Development of supraglacial drainage systems on the Devon Ice Cap and its connection to the formation of near-surface ice layers within the shallow firn

by

Luísa da Cunda Fernandes

A thesis submitted in partial fulfillment of the requirements for the degree of

Doctor of Philosophy

Department of Earth and Atmospheric Sciences
University of Alberta

Abstract

Increased mass loss from the Canadian Arctic ice caps is associated with regional increases in the summer mean glacier surface temperature and the annual number of melt days. As a result of these changes , snow and ice melt are likely to occur at higher elevations and become more widespread, especially in the percolation zone, where surface meltwater percolates into the subsurface and refreezes. Such a process adds uncertainties to predictions of rates of both glacier mass loss and ensuing sea-level rise because of the unknown distribution of locations at which meltwater percolates and refreezes. The absence of a known infiltration pattern makes it challenging to obtain accurate information about all the processes associated with firn densification and its impact on the development of supraglacial drainage networks.

This study used remote sensing techniques to identify permeable and impermeable substrates within the accumulation zone of the Devon Ice Cap by mapping temporal changes in the extent and distribution of glacier facies zones and inter-annual variability in the spatial extent, timing and characteristics of supraglacial meltwater runoff. Comparisons between observations obtained from satellite remote sensing data and ground-truth data obtained using Ground Penetrating Radar and shallow firn cores are used to ascertain whether the methods used facilitate the study of changes in firn structure over large geographical areas. Our results suggest that analysis of the distribution and inter-annual variability of supraglacial drainage networks in firn-covered regions is a promising approach to study regional scale changes in firn structure at a relatively low cost, and to characterize spatial heterogeneity in firn runoff processes that contribute to glacier mass loss and, ultimately, sea-level rise.

Preface

A version of Chapter 2 has been published in the Proceedings of the 12th European Conference on Synthetic Aperture Radar (EUSAR 2018) (available at https://www.vde-verlag.de/proceedings-en/454636127.html). I was responsible for the data analysis and manuscript composition. All authors (M. Sharp, A. Schmitt; A. Wendleder, A. Roth) contributed to manuscript edits.

All other chapters are unpublished work. I completed the study design, field work, data analyses and manuscript composition. A. Dubnick and M. Sharp assisted with field work and A. Rutishauser assisted with Ground Penetrating Radar processing. C. Mortimer contributed to manuscript edits on Chapter 3. M. Sharp contributed to manuscript edits in all chapters.

.

Table of Contents

List of Tables

List of Figures

Chapter 1 - INTRODUCTION

1.1 Motivation

Mass losses from the Canadian Arctic ice caps, currently the major regional contributor to the non-steric component of global sea-level rise after the Antarctic and Greenland ice sheets (Gardner et al., 2011), have increased dramatically in recent decades. The ice masses in the Canadian Arctic Archipelago (CAA) are estimated to contain between 22,336 and 37,555 Gt of ice, distributed over an area of ~150,000 km^2 (Huss and Farinotti, 2012; Marzeion, Jarosch and Hofer, 2012; Grinsted, 2013; Radić et al., 2014), and this represents ~ 45% of the world's ice mass outside the two ice sheets in Antarctica and Greenland. Satellite data from GRACE (Gravity Recovery and Climate Experiment) suggest that approximately 800±8 Gt of ice was lost from ice caps and glaciers in the CAA from 2003-2015 (Blunden, Arndt and Hartfield, 2018). A more recent study using GRACE data from April 2002 to August 2016 found that the North portion of the Canadian Arctic (as defined by the RGI – Randolph Glacier Inventory (RGI Consortium, 2017)) lost mass at an average rate of 35.8±3.5 Gt yr^{-1}, while the South portion lost mass at a rate of 32.5±7.8 Gt yr^{-1} (Wouters, Gardner and Moholdt, 2019). The occurrence of these rates of mass loss coincides with a ~1ºC increase in the regional mean summer glacier surface temperature in the CAA from 2000-2015 (mainly between 2005 and 2012), which accounts for recent surface temperatures being 1º C to 1.2º C higher than the mean of values recorded between 1948 and 2015 (Mortimer, Sharp and Wouters, 2016).

The Devon Ice Cap (DIC), the second largest ice cap in the CAA, covers an area of approximately 14,000 km^2, has a maximum ice thickness of ~800 m (Dowdeswell *et al.*, 2004), and an estimated volume of 3962 ± 140 km^3 (Boon *et al.*, 2010). It ranges in

elevation from sea level to 1920 m a.s.l. The total mass loss from DIC from 1963 to 2003, including that by iceberg calving, was estimated to be ~78 km^3 water equivalent (Burgess and Sharp, 2008). Mass loss by supraglacial melt and meltwater runoff accounts for 60-90% of this total (Hock, 2005; Mair, Burgess and Sharp, 2005).

The annual number of melt days on the DIC during the period 2000-2004, derived using images from the SeaWinds scatterometer (on board the QuikSCAT satellite), was 42.1 ± 6.3 days (Wang *et al.*, 2005). Using a sixteen-year (2000-2015) record of satellite-derived ice surface temperatures for different elevation zones on the ice cap, Mortimer et al. (2016) demonstrated that surface melt has likely increased substantially in recent years at higher elevations on the ice caps of the Canadian High Arctic. Arctic surface and lower troposphere air temperature records for the past three decades show regional warming that exceeds any seen in proxy temperature records for the past 2000 years (Kaufman *et al.*, 2009; *IPCC*, 2013). This has resulted in pronounced summer melting on the ice caps.

Where surface melting occurs in the ice cap's accumulation area (the region where annual snowfall exceeds annual melt/runoff), meltwater percolates downwards into permeable snow/firn, where it may fill the pore volume. If the temperature of the surrounding snow/firn is below 0 ºC, the meltwater will refreeze and may form extensive ice layers within the firn (Bøggild, Forsberg and Reeh, 2005). The occurrence of such ice layers on the DIC, and their growth over time, have been documented by ice coring and ground penetrating radar studies, as well as by dramatic warming of the firn that is associated with latent heat release as percolating meltwater freezes within the firn (Bezeau *et al.*, 2013; Gascon *et al.*, 2013, 2014). Because firn has a high capacity to absorb and retain meltwater (Pfeffer and Meier, 1991; Fountain and Walder, 1998; Jansson, Hock and

Schneider, 2003; Bøggild, Forsberg and Reeh, 2005; de Woul *et al.*, 2006) early studies of this process (Harper *et al.*, 2012) argued that the pore volume of the firn column would have to be totally filled with infiltration ice before runoff from firn-covered regions of ice caps could occur and contribute to sea-level rise. However, recent studies suggest that, even when empty pore volume is available, surface runoff begins to dominate over meltwater storage well before the firn column becomes completely filled with meltwater (Machguth *et al.*, 2016a; MacFerrin *et al.*, 2019). The presence of ice layers near the surface of the firn creates a feedback whereby the fraction of meltwater generated in the accumulation area that runs off directly to the ocean is increasing while, at the same time, the generation of surface meltwater runoff is both increasing and becoming more widespread. In flat areas or surface depressions from which the meltwater does not run off, the firn may become water-saturated during the spring melt period, forming an unstable slush "swamp", from which slush flows may eventually develop, resulting in an additional mass transfer to lower elevations, where the slush may be fully converted to liquid water.

1.2 Objectives

Recent warming in the Arctic has resulted in pronounced summer melt and the continued meltwater production throughout the years is speeding up the development of widespread and thick ice layers. The observed changes in the firn area of the Devon Ice Cap raise the following questions:

1) Could we use satellite remote sensing techniques to map the growth of ice layers near the surface of the Devon Ice Cap and their evolution over time in order to identify permeable and impermeable substrates?

2) What information can be retrieved with the continued mapping of inter-annual variability in the extent and character of supraglacial meltwater development using optical remote sensing imagery?

3) Is it possible to make use of the penetration capability of satellite radar imagery to detect ice formation in the shallow subsurface of the accumulation area through changes in spatial and temporal radar backscattering?

Predictions of future sea level change suggest that small ice caps and mountain glaciers will be the dominant sources of eustatic sea-level rise over the next century (Radić and Hock, 2011; Radić *et al.*, 2014; Harig and Simons, 2016). Likewise, the quantity of meltwater produced in the percolation zone of ice caps and glaciers in the CAA (where snowmelt occurs at the surface but the resulting water percolates into the subsurface and refreezes) is predicted to increase, and the area affected by the infiltration of surface meltwater into the firn, which redistributes water both vertically and horizontally, is expanding. Although the major changes in the structure of the firn layer on the Devon Ice Cap that have occurred in the last decade have been well documented, the evidence comes from ice core stratigraphy and ground-based and airborne ice-penetrating radar measurements collected along a relatively small number of linear transects (Bezeau *et al.*, 2013; Gascon *et al.*, 2013; Rutishauser *et al.*, 2016). This makes it difficult to quantify the rate and overall pattern of ice layer growth within the firn layer as a whole, and to evaluate its likely impact on meltwater runoff from the entire accumulation area.

To address this problem, we map the distribution and growth of ice layers near the surface of the firn on the DIC and their evolution over time in order to identify permeable

and impermeable substrates. Three different methods are used to achieve this objective: (a) spatial and temporal changes in radar backscatter from the firn-covered areas of the ice cap are mapped using the Kennaugh Elements (KE) approach (Schmitt, Wendleder and Hinz, 2015) applied to X-band SAR data; (b) inter-annual variability in the extent and character of supraglacial meltwater runoff is mapped using multi-temporal remote sensing data from optical imagery (Landsat 7/8); (c) the surface drainage pattern that would be expected if firn were impermeable to meltwater is simulated using a hydrological flow routing algorithm applied to a representation of the surface topography of the ice cap derived from a digital elevation model (Arctic DEM). Additional data from GPR (Ground Penetrating Radar) surveys and shallow firn cores are used to test the assumption that changes in radar backscatter can be used to identify areas where massive ice layers form in the shallow subsurface layer of the firn.

This will be the first attempt to apply this new methodology to satellite radar data in order to study changes in the structure of the firn layer of ice caps at a large spatial scale with the goal of documenting spatio-temporal patterns in ice layer growth (or decay) and their impact on surface runoff patterns. This method could result in a new approach to the study of firn-layer change that would be applicable to other glacierized regions, particularly in Greenland, where rapid changes in firn structure due to refreezing of percolating meltwater have also been observed (Pfeffer and Meier, 1991; Bøggild, Forsberg and Reeh, 2005; Harper *et al.*, 2012; Forster *et al.*, 2013; Machguth *et al.*, 2016a).

1.3 Scientific Background

The *Kennaugh matrix*, also known as the *Stokes scattering matrix*, is a mathematical approach to evaluate the power returned to a radar receiver, given the

polarization characteristics of the receiving antenna (Guissard, 1994). The resulting *Kennaugh elements* are easily derived using a decomposition technique to separate the total intensity backscattering strength from the polarimetric information. The KE method was chosen for use in this study because it is highly sensitive to polarimetric backscattering. Moreover, it can be applied to multi-scale, multi-polarized, multi-temporal and multi-frequency SAR images, and is therefore suitable for the detection of both temporal and spectral change (Schmitt, Wendleder and Hinz, 2015). The Kennaugh decomposition for the co-polarized (HH-VV) image delivers 4 elements as follows:

$$K_0 = \frac{1}{2}\{|S_{HH}|^2 + |S_{VV}|^2\} \quad (1)$$

$$K_3 = -Re\{S_{HH}S_{VV}^*\} \quad (2)$$

$$K_4 = \frac{1}{2}\{|S_{HH}|^2 - |S_{VV}|^2\} \quad (3)$$

$$K_7 = Im\{S_{HH}S_{VV}^*\} \quad (4)$$

The elements K_0 and K_4 are purely intensity-based and correspond to the total intensity of scattering and the difference in scattering between horizontally and vertically oriented dipoles, respectively. The element K_3 represents the real part (Re) of the inter-channel phase shift and contains the difference between even (also known as double) and odd (also known as single) bounce scattering, while the K_7 element represents the imaginary part (Im) of the inter-channel phase shift and the phase difference between even and odd bounce scattering. The S stands for the summarized intensity of the measured image channels.

To evaluate the seasonal progression of surface melting, detect ice layers that form within the firn, and identify the changes in scattering associated with the formation of ice layers, KE signatures for each pixel are retrieved by capturing the spatiotemporal evolution of backscattering, especially right after the end of the melt season when water in the firn is expected to freeze, resulting in a greater radar penetration depth. This procedure will enable us to analyze the backscatter signature at two different time-scales: (a) Intra-annual and (b) Inter-annual (for the summer season). Mapping of the formation and distribution of ice layers in firn was first attempted using the biweekly averaged backscattering for date-defined periods, using 12.5-km spatial resolution data, immediately prior to and after the melt season on the Greenland ice sheet using QuikSCAT data (Nghiem *et al.*, 2005). A similar method based on the same data was evaluated over the Canadian Arctic, this time using a floating-date period, to map changes in the distribution of ice layers within the firn over time (Wang *et al.*, 2005).

The advantage of the KE approach, besides its high spatial resolution, is that the K_3 element contains information that indicates whether the returned backscatter signal results from interaction with the surface (odd bounce) or from irregularities within the medium (even bounce). The KE method was used successfully to monitor and classify ice growth and lake freeze-up in the Mackenzie Delta, in the Beaufort Sea region of the Arctic Ocean, using the same antenna configuration and polarization as is proposed for this research. In this region, the backscattering was characterized by a temporal switch from odd bounce to even bounce during freeze-up (Wendleder, Roth and Schmitt, 2014). A similar change is expected to occur on Arctic ice caps in mid-August or September when the air temperature

drops below 0°C, melt comes to an end, and water remaining in firn areas, ponds, lakes, or supraglacial channels refreezes.

The distribution of surface water on glaciers is highly variable in space and time, but it can be extensive, especially during the summer months. Once formed on a glacier, water may either be stored in depressions on the glacier surface, run off over the glacier surface, percolate into underlying snow and/or firn (where it may freeze or be stored as pore water), or penetrate (via crevasses and/or moulins) to the glacier bed, where it runs off in a down-glacier direction. On Arctic ice caps, all of these situations can occur during a single melt season.

When melting begins on snow surfaces in spring, water percolates into the pore volume of the snow-pack. Early in the melt season, when the snowpack is still cold after the preceding winter, it is likely that such water will refreeze, releasing latent heat that warms the snowpack and firn until either the water is completely frozen or the snowpack temperature reaches the melting point. Due to the low surface slope of ice cap interior regions, snow and firn in these regions can become water-saturated, especially where ice layers formed by refreezing within the firn impede vertical meltwater drainage (Muller, 1961; Pfeffer and Meier, 1991). This can result in surface ponding in depressions or locally flat areas and/or in the occurrence of slush flows on steeper slopes. Slush flows may initiate or re-open pre-existing supraglacial drainage channels by removing mass from the snowpack by mass failure and downslope transport of water-saturated snow/firn (Mortimer, Sharp and Wouters, 2016). This is especially the case at lower elevations, where supraglacial meltwater channels are carved into the surface of glacier ice lying beneath the snowpack (Ferguson, 1973; Marston, 1983; Knighton, 1985; Greuell and Knap, 2000;

Boon *et al.*, 2010; Irvine-Fynn *et al.*, 2011). In the accumulation area, slush flows may also cut channels into the surface of massive ice layers that formed by refreezing within the firn. Slush flows were reported in the Arctic and High Subarctic regions by Washburn (1980) and Clark (1988) and their impacts were described following a single massive rainfall-related event on the Brewster Glacier, New Zealand, (Smart *et al.*, 2000). Once channels are initiated by slush flows, they become a focus for meltwater drainage from the surrounding slopes.

To investigate how supraglacial meltwater channel systems change over time, the distribution, structure, and continuity of supraglacial drainage channels were digitized manually from a combination of Landsat 7 and 8 images, providing an evolving-time series from 2000 to 2017. Using this assemblage of data improves the temporal resolution of channel mapping. The distribution, extent, continuity, and structure of supraglacial channel systems, and their evolution over the melt season are mapped using a combination of visible imagery. Due to the narrow width of many supraglacial channels, visual interpretation of optical data is a logical approach for mapping hydrological networks on glaciers. This approach was previously applied successfully to DIC using Landsat-7 imagery (Wyatt and Sharp, 2015).

Drainage network structures can provide evidence about the location of ice layers within the firn as channels evolve quickly from incipient to well-developed each year as surface melting progresses and eventually wanes (Karlstrom, Gajjar and Manga, 2013). The presence of impermeable ice layers that formed either during a previous melt season and are buried within the firn, or early in a melt season within the end of winter snow cover, will locally limit the ability of water to percolate into the snow and firn, hindering its access

to pore space available below the ice layers (Machguth *et al.*, 2016a). This will promote water-saturation of the overlying snow early in the following melt season. Meltwater will pond and create areas of slush that may develop into lakes as the melt season progresses. Where local slope angles are large enough, supraglacial channels may form or re-open, forcing the meltwater to run off via a near-surface drainage system (Smith *et al.*, 2015). By contrast, water will percolate downwards into snow and/or firn that contain no or few ice layers. The distributions of water-saturated and under-saturated areas of the firn will be obvious because the presence of liquid water is easily detected by radar, as it results in high absorption of Radio Frequency energy, causing low backscatter (Malnes *et al.*, 2006). At the end of a melt season, new ice layers will form by freezing where water was stored in ponds, lakes, and slush "swamps" during the summer.

Repeat supraglacial drainage maps are used to identify major temporal changes in the drainage network, such as the appearance of new supraglacial channels at higher elevations in especially warm summers. As warm summers likely produce thicker and more extensive ice layers than cold summers (Sylvestre *et al.*, 2013), it is crucial to map and monitor the highest elevations at which supraglacial channels can be detected during each melt season by superimposing the yearly maximum drainage extent maps on the DEM. Such an analysis will be used to describe and explain drainage system and channel development during the summer periods of successive years, and to identify networks of temporary channels that may not develop in all years.

DEMs, computed simplifications of land-surface topography that are used to model and/or characterize the real terrain, are widely used for detecting temporal changes in glacier topography driven by surface melt, snow accumulation and/or ice dynamics

(Flowers and Clarke, 2002; Bolch *et al.*, 2008; Naz *et al.*, 2014; Li *et al.*, 2015). Ice and water flow patterns have been determined for DIC (Dowdeswell, 2004; Burgess *et al.*, 2005; Wyatt and Sharp, 2015). However, in order to understand the mechanisms that control water flow and accumulation patterns, topographic information, such as relief and hydrography are extracted from the Arctic DEM and used to reconstruct the likely spatial patterns of meltwater drainage, ponding, and drainage catchment structure on the surface of the DIC.

Most large-scale surface topography of the ice cap is controlled by the interaction between ice flow and the subglacial bedrock topography, especially in fast-flowing outlet glaciers, and by variations in the ice thickness. Ice may override the bed topography if the topographic amplitudes of the bedrock are less than the ice thickness, while the ice may fold, generating a subdued version of the bedrock topography in the surface topography if the topographic wavelengths are larger than the ice thickness (Hindmarsh *et al.*, 2006). The thickness of the DIC increases rapidly inwards from the margin and more slowly towards the central dome (where there is a maximum ice thickness of ~800 m), and the bed topography and surface topography are closely connected (Dowdeswell, 2004). For this reason, the Arctic DEM provides a good basis for reconstructing the surface meltwater drainage system. Nonetheless, in this case, the difference in time between the acquisition of the images used to construct the Arctic DEM and map the present surface drainage system structure could be as much as 17 years, thus some changes in surface topography would be expected and this may result in some differences between mapped and modelled drainage network structures.

To investigate patterns in the near-surface permeability of the ice cap, a synthetic drainage pattern is derived using the Arctic DEM. The synthetic drainage channel mapping is performed using the D8 (Directional Eight) flow direction model (Jenson and Domingue, 1988), which determines the flow direction according to the line of steepest descent on a grid box of 3x3 pixels. The steps involved include identifying sink areas in the Arctic DEM that are caused by noise in the dataset, and infilling the associated depressions prior to using the D8 model to extract information about flow direction and flow accumulation. The recurrent appearance of lakes on the ice cap surface indicates where depressions in the DEM surface are likely to be real. However, this approach assumes that runoff occurs over an impermeable surface, which may not be the case for snow and firn-covered areas of the ice cap, or for areas where glacier ice is crevassed. Thus, comparison of the modeled drainage map with the drainage maps extracted from Landsat-7/8 imagery (that truly represent the drainage system) will allow identification of areas where drainage patterns are affected by crevasses and/or ice layers in the firn, and where water becomes ponded in depressions in the ice cap surface.

1.4 Thesis outline

The chapters of this thesis follow a progression from an analysis of spatio-temporal changes in the distribution of firn-covered areas on the ice cap to the local identification of ice layers forming in the shallow subsurface layer of the firn.

In Chapter 2 “Detecting Supraglacial Meltwater Drainage On The Ice Cap Using Kennaugh Decomposition Of Terrasar-X Imagery”, parts of which have been published in the Proceedings of the 12th European Conference on Synthetic Aperture Radar (EUSAR 2018) (available at https://www.vde-verlag.de/proceedings-en/454636127.html), the focus

is on the interpretation of spatial and temporal changes in radar backscattering from the DIC using the Kennaugh Decomposition applied to TerraSAR-X imagery. Using a series of TerraSAR-X images, we focus on the interpretation of the resulting Kennaugh Elements and on the identification of the melt onset and freeze-up periods. This allows us to characterize areas where refreezing occurs and, as a consequence, to identify locations where ice layers are more prone to form based exclusively on the interpretation of the KE derived from TerraSAR-X imagery.

In Chapter 3 “Supraglacial Drainage Network Expansion On The Devon Ice Cap In Response To Changes In The Shallow Subsurface Hydrology Of The Firn Covered Areas””, we examine temporal variability in the extent of supraglacial meltwater channels on the Devon Ice Cap using Landsat 7 and 8 images from 2000 to 2017. Our observations, focused only on firn-covered areas, suggest that a surface drainage network is only likely to form and persist over multiple years in areas where the firn layer is impermeable to meltwater. A synthetic drainage network extracted from the ArcticDEM (based purely on the assumption that the surface of the ice cap is completely impermeable) provides additional information when compared to the Landsat-derived drainage network. The product derived from comparison between mapped and modeled drainage networks shows areas in which an impermeable ice layer has formed based on the ice cap’s natural slope and/or the multi-temporal mapping of subsurface ice layers in the firn.

Although the first two chapters of the thesis explore different methods to locate areas where ice layers and ice slabs >1 m thick (MacFerrin *et al.*, 2019) are forming within the firn layer on the Devon Ice Cap, the question of whether these methods are efficient and accurate is discussed in Chapter 4. In Chapter 4 “Detecting Ice Layers In The

Percolation Zone Of The Ice Cap Using Terrasar-X Images" we examine Ground Penetrating Radar (GPR) profiles from areas that were identified as possibly containing ice layers in Chapters 2 and 3. A gridded GPR dataset was collected over a potential ice layer (or ice slab) that was identified in Chapter 2, and along the Cryosat line on the southern flank of the ice cap. These GPR profiles support the findings reported in Chapters 2 and 3. In the fourth chapter, we present evidence of the widespread formation of shallow ice layers within the firn layer on the Devon Ice Cap during a summer melt season.

Chapter 5 summarizes our findings, proposes answers to the questions that we set out to address, and suggests some directions for further work on this topic.

Chapter 2 - DETECTING SUPRAGLACIAL MELTWATER DRAINAGE ON THE DEVON ICE CAP USING KENNAUGH DECOMPOSITION OF TERRASAR-X IMAGERY

2.1 Introduction

Recent increases in mean summer air temperature over the Arctic have resulted in longer melt seasons and in increased surface runoff from ice caps and glaciers (Gardner and others, 2011, 2013; Sharp and others, 2011; Fisher and others, 2012; Bezeau and others, 2013; Gascon and others, 2013). The total mass loss from the Devon Ice Cap (DIC), the second largest ice cap in the Canadian Arctic Archipelago, was estimated to be ~ -78 km^3 w.e. (water equivalent) from 1960 to 1999 (Burgess and Sharp, 2008) with the greatest source of mass loss being supraglacial melting and meltwater runoff (Hock, 2005). At higher elevations on the ice cap where there is a perennial snow cover, surface meltwater initially percolates into the pore volume of the snowpack and/or underlying firn and refreezes. If sustained over a period of years at a given location, this process may result in the formation of extensive ice layers within the firn (Bezeau *et al.*, 2013; Gascon *et al.*, 2013). Once formed, these ice layers impede the vertical percolation of meltwater into the snow and firn, cause lateral and/or downslope diversion of water flow, and increase the fraction of melt generated in the accumulation area that runs off to the ocean.

Due to the low surface slopes in the interior regions of ice caps, snow and firn overlying relatively impermeable ice layers can become water-saturated during the melt season. This may result in ponding of meltwater and slush formation in flat areas of the ice surface and can promote extensive slush flows in areas where slopes are locally steeper. Slush flows remove mass from the snowpack and transport it downslope via eroded

channels that become a focus for meltwater drainage from the surrounding snow and firn. Some of the water that drains through these channels may reach the glacier bed via channelized drainage into moulins or open crevasses. Early in the melt season, slush flows may also drain directly into crevasses and/or moulins. Surface melt ponds may drain directly to the bed if hydro-fracture-driven growth of crevasses on their floors creates a surface-bed connection (Zwally *et al.*, 2002; Boon and Sharp, 2003; Palmer *et al.*, 2011). Spatially and temporally variable delivery of surface water to the glacier bed may influence glacier flow dynamics (Phillips *et al.*, 2013; Tedesco *et al.*, 2013). Until recently, when supraglacial lakes were discovered buried in snow on the Greenland Ice Sheet (Koenig *et al.*, 2015), the hydrology of snow and firn-covered glacier surfaces was little studied. This is partly because the widespread occurrence of water-saturated snow and firn within the accumulation areas of glaciers during the melt season, and the hazard posed by slush flows, make it difficult to undertake season-long ground-based studies of surface drainage-development.

Multi-temporal remote sensing technologies such as Synthetic Aperture Radar (SAR), which can acquire high-resolution images at any time of day and are relatively unaffected by clouds, have the potential to provide regular time series of observations of conditions on the snow- and firn-covered areas of ice caps. Thus, they complement the sparse datasets provided by optical sensors. The timings of melt onset and freeze-up are easily observed using microwave sensors due to the high absorptivity of liquid water, which causes a strong attenuation of the microwave radiation, resulting in weak backscattering (Malnes *et al.*, 2006). Here we use data from the German Earth Observation satellite TerraSAR-X (TSX), which was launched in 2007 by DLR (German Space Center).

TSX provides dual-polarized data (HH-VV) with a revisit time of 11 days and a spatial resolution of up to 3m in the StripMap acquisition mode. Our goal is to demonstrate the great potential of X-band (12.5-8 GHz) dual-polarization SAR imagery for detecting the seasonal onset of surface melting on Arctic ice caps, the evolution of water storage in snow and firn, and the development of surface meltwater drainage systems on the DIC, Nunavut, Canada. To achieve these objectives, we used automatic pre-processing and computed the Kennaugh Elements for time series of TSX data using the Schmitt-Algorithm (Schmitt, Wendleder and Hinz, 2015) in order to separate two important and distinct parameters: the total intensity backscattering strength of the radar return (K_0) and the polarimetric information (K_3). We focus only on these elements as they reveal the most significant changes that occurred over the time period analyzed. Complete information about the four Kennaugh Elements derived from Dual Co-polarized TSX images is found in Chapter 1 (section 1.3 above).

Processes related to firn densification due to retention and percolation of meltwater in the accumulation area of glaciers is associated with availability of meltwater. By using radar images, specifically Decomposed Elements from TerraSAR-X images, it is possible to distinguish areas where the firn/snow surface gets saturated my melt from that where meltwater is not so abundant or/and the firn has capacity for retaining meltwater into pore volume in the subsurface. Discriminating between the two means an advance in the study of firn densification processes at the same time it provides a large observation area compared to the prevailed and limited coverage offer by the Ground Penetrating Radar method. The potential of the K_0 element is its ability to detect surface melt because the high absorptivity of liquid water attenuates the radiation and limits the transmissivity,

ultimately resulting in a weak backscattering. The advantage of the K_3 element in differentiating between the even bounce (high subsurface contribution) and the odd bounce (high surface contribution) scattering is suitable in the detection of ice layer formation within the firn.In addition, due to the penetration capacity of the x-band and as such of the Kennaugh Elements retrieved from the TerraSAR-X images, it is anticipated that ice layer formation within the shallow subsurface of the firn is likely detectable.

2.2 Test site

The test site is located on the southern flank of the ~14,000 km^2 Devon Ice Cap between 75°30'N / 82°35'W in the northwest and 74°40'N / 82°55'W in the southeast (Figure 2.1). This area was chosen for investigation because it has been the subject of previous InSAR measurements of glacier flow, ground-based radar studies, and ice core and borehole-based analyses of the structure and temperature of the firn layer. There are also two automatic weather stations (AWS) in the area (Burgess *et al.*, 2005; Bezeau *et al.*, 2013; Gascon *et al.*, 2013; Wyatt and Sharp, 2015; Rutishauser *et al.*, 2016). A previous study of the surface hydrology of the region using optical data from Landsat-7 acquired in 1999 suggested that the highest elevation at which supraglacial meltwater channels could be detected was 1420 m a.s.l. (above sea level) (Wyatt and Sharp, 2015). The same study also found no indication of meltwater at higher elevations. However, an earlier study covering the period 1999-2005 using data from the SeaWinds scatterometer found that surface melting extended all the way to the summit of the DIC in some years (Wolken, Sharp and Wang, 2009).

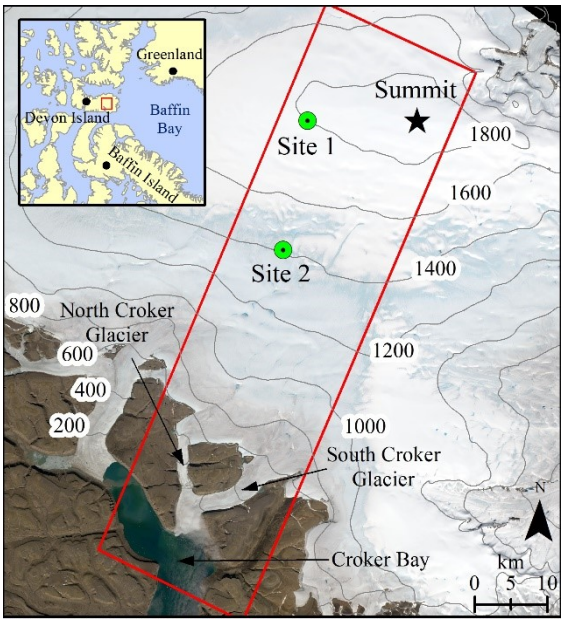

Figure 2.1 - Locations of the automatic weather stations (AWS) at Site-1 (~1800 m a.s.l) and Site-2 (~1400 m a.s.l.). The red rectangle outlines the area with TSX coverage. The background image is a Landsat-8 true-color composite image acquired on July 26, 2015. The inset shows the location of the Devon Ice Cap.

2.3 Background

Over the course of a year, glaciers may gain mass by accumulation of snow (mainly from fall to spring) and lose mass by surface melting and meltwater runoff (mainly in summer). In the accumulation zone of an ice cap, supraglacial meltwater channels may extend above the equilibrium line altitude (ELA) during the melt season. Their annual formation may involve re-opening of pre-existing channels by slush avalanches that result from failure of a water-saturated snowpack (Fountain, 1996). Below the ELA, in the ablation zone, supraglacial channels are formed by localized thermal erosion of the glacier ice surface by summer meltwater runoff, and they may persist over multiple years (Ferguson, 1973). Supraglacial channels in the ablation zone are usually significantly longer than channels formed in the accumulation zone, where the pore volume of the firn can retain meltwater and delay runoff.

Microwave radar data are well suited for discriminating between the accumulation and ablation zones of a glacier, and for differentiating "facies zones" on the glacier surface, even though facies boundaries may shift over time as weather and climate change. Glacier facies zones are defined on the basis of the physical and thermal properties of the materials exposed at, and immediately below, the glacier surface. Typically, some combination of the following facies is recognized (a) a dry snow zone, where snow is not subject to melting; (b) a percolation zone, where snowmelt occurs at the surface but the resulting water percolates into the subsurface and refreezes; (c) a wet snow zone, similar to (b), but where the amount of latent heat released during refreezing is sufficient to raise the temperature of the snow and firn to the pressure melting temperature; (d) a superimposed ice zone, where melt water percolates down to the base of the snow/firn and refreezes directly onto the underlying glacier ice - and where the resulting ice is exposed at the surface before the end of the melt season, and (e) a bare ice zone where glacier ice is exposed at the surface during much of the melt season. All these facies zones are found on the Antarctic and Greenland ice sheets, but a more restricted set of facies zones may be found on smaller ice caps and glaciers. For instance, the dry-snow zone is often missing from smaller ice caps and valley glaciers, where summer melt occurs over the full vertical extent of the ice mass. The extent and spatial distribution of the different facies zones on a given ice mass may change over time due to changes in summer climate (Sylvestre *et al.*, 2013).

The distribution of persistent supraglacial meltwater channels on the DIC is largely determined by the distribution of summer melting and by the slope of the ice cap surface. The density of channels is highest at lower elevations where the glacier surface is exposed

to warmer air temperatures and glacier ice is exposed at the surface in summer. At higher elevations, in the percolation zone, the local absence of supraglacial channels may be explained by vertical percolation of meltwater into the snow and firn that results in refreezing within the available pore volume or, at the highest elevations, by the lack of sufficient meltwater production to saturate the pore volume of the snow and firn and generate surface runoff (Nienow and Hubbard, 2005). The density of surface meltwater channels over wet snow and firn increases where meltwater is abundant. Where surface slopes are low, however, meltwater may fill the pore volume, allowing the formation of "slush swamps" and/or lakes and ponds, on the glacier surface (Chu, 2014). In the superimposed ice and bare ice zones, the low permeability of the glacier surface results in more abundant surface meltwater which may accumulate in supraglacial lakes or run off via well-developed meltwater channels (Irvine-Fynn *et al.*, 2011). Supraglacial streams may be captured by crevasses and/or moulins and diverted into the body of the glacier.

2.4 Data and Methods

2.4.1 TSX data Processing

To detect the evolution of supraglacial meltwater drainage on DIC during the 2015-2018 melt seasons, twenty-four dual co-polarized (HH and VV) TSX images were acquired between June and August of each year. The selection of acquisition dates was based on the timing of the summer melt season (as defined by records of surface air temperature from the two automatic weather stations on the ice cap within the study area (Figure 2.1)). All images were obtained from the same relative orbit, and have the same acquisition geometry and incidence angle, which facilitates comparison of images acquired on different dates. The images have a 5 m pixel spacing after pre-processing.

Processing of the co-polarized TSX images involves 3 steps: Kennaugh decomposition, orthorectification, and radiometric enhancement. These processing steps were accomplished using the Schmitt-Algorithm (Schmitt, Wendleder and Hinz, 2015).

2.4.2 Kennaugh Decomposition

The Kennaugh Decomposition approach was chosen due to its high sensitivity to polarimetric backscattering, and suitability for detecting temporal and polarimetric change. For dual co-polarized images, the Kennaugh method for the co-polarized (HH-VV) images returns four independent elements. K_0 represents the total backscattering intensity, K_3 contains the scattering difference between the even bounce and the odd bounce, K_4 reflects the scattering difference between horizontally and vertically oriented dipoles, and K_7 represents the phase difference between the even and odd bounces. As the K_0 and K_3 elements revealed more significant changes in backscattering over the study period than the K_4 and K_7 elements, only the K_0 and K_3 elements are discussed further here.

2.4.2.1 *Orthorectification*

Surface elevation is a key variable for the proposed study due to its strong influence on the incidence, distribution, and intensity of surface melt, and on the development of the surface meltwater drainage system. Due to the intrinsic acquisition geometry of SAR sensors, there is significant terrain distortion due to foreshortening, layover, and shadowing effects, especially in areas with steep slopes. The TanDEM-X digital elevation model was used to orthorectify the images to minimize these effects and to calibrate for terrain-induced variations in backscatter intensity.

2.4.2.2 Radiometric Enhancement

Due to the coherence of the radar signal, SAR data exhibit high additive and multiplicative speckle – a form of noise that degrades the visual quality of images. A new approach called *multi-scale multi-looking* (Schmitt, Wendleder and Hinz, 2015) has been developed to adapt the local number of looks to the image content, resulting in a very smooth SAR image which retains radiometric information.

2.4.3 Melt Onset and Freeze-up

Information about the annual melt onset and freeze-up dates was available from the two AWS for the period 2004-2016 (Table 2.1). The absence of temperature data for later years is due to the decommissioning of the weather stations. The start and end dates of the melt season in each year were defined as the first and last dates on which the daily mean air temperature exceeded 0°C. In 2015, the Site-2 station record shows that melting began on June 29th and ended on August 4th (June 9th and August 29th in 2016), yielding totals of 37 days of melting in 2015 and 82 days in 2016). The record from Site-1, located ~400 meters higher than Site-2, showed that in 2015 melting began one day later and ended one day earlier than at Site-2, giving a melt period of 35 days. In 2016, 78 days of melting were recorded at Site-1 where melt onset occurred on June 11th and freeze up was on 27th August. The 12-year air temperature records from these sites indicate that the melt season is usually longer at Site-2 and slightly shorter at Site-1 than it was in 2015.

Table 2.1- 2015 and 2016 and 12 year averages (2004-2016) of melt onset day, melt freeze-up day and melt duration.

		2015	2016	Average (2004-2016)
SITE 1	Melt onset (DOY)	181	163	186
	Freeze-up (DOY)	215	240	219
	Melt duration (days)	35	78	35
	Single days T > 0°C	19	16	14
	PDD sum (°C)	30	16	21
SITE 2	Melt onset (DOY)	180	161	177
	Freeze-up (DOY)	216	242	224
	Melt duration (days)	37	82	48
	Single days T > 0°C	33	38	34
	PDD sum (°C)	44	54	42

2.5 Results and Discussion

In order to detect the timings of melt onset in spring and freeze-up in fall, and the progressive evolution of surface meltwater drainage within the study area, the Kennaugh Elements were calculated for all twenty-four TSX images (2015-2018). The K_0 element represents the total backscattering intensity, which may be influenced by the dielectric constant, the roughness of the surface, and the surface geometry. The K_3 element indicates whether backscattering results from the surface (odd bounce) or from within the snowpack (even bounce). The Kennaugh Elements are multi-temporal, which means that their radiometric stability does not change over time if there is no variation in backscatter intensity or polarimetry. As such, all variations in the computed elements are, in this specific case, associated with changes in the snow/firn package. These are due mainly to melting and/or snow precipitation. Although the timings of melt onset and freeze-up, and the duration of summer melt differ between years, the interpretation of the observed

changes in the K_0 and K_3 elements is the same, and it takes into consideration the length of the melt season in that specific year. For this reason, we present the derived elements for 2015-2018 but we discuss in detail only the results from 2015 (Appendix A - Chapter 2).

On June 20, 2015 (Figure 2.2 frames A and B), none of the weather stations recorded temperatures > 0°C, suggesting that there was no surface melt on that date. The percolation zone shows strong backscattering in K_0, which K_3 suggests is dominated by the even bounce, which is due to the presence of ice pipes and ice lenses within the snowpack. The wet-snow zone shows a mix of even and odd bounce from the interface between the ice and the overlying snow. The superimposed ice and bare ice zones show a dominance of surface scattering as the snow cover at lower elevations is thin and some rough ice may already be exposed. The sea ice surface in Croker Bay also shows surface scattering as this ice has a rough surface caused by irregular edges, ridges, and floes. The Landsat-8 image from July-3 (Figure 2.1) exhibits the optical properties (true-color composition) of the glacier prior to extensive melt and shows no distinction between the glacier facies zones. For the purposes of clarity and consistency throughout the analysis of the TSX images, the glacier facies boundaries delineated in Figure 2.2 (frames A and B) are taken to demarcate initial facies boundaries that are expected to change location over the time period represented by the image series.

The TSX image of July-1 2015 (Figure 2.2 frames C and D) was acquired 2 days after melt onset at Site-2 and 1 day after melt onset at Site-1. The wetness of the snow results in low backscattering in K_0 and dominance of even bounce in K_3 as bare ice is exposed as the thin snow cover melts. Frames C and D show the spread of the superimposed ice and bare ice zones to higher elevations and consequently, the shrinkage of the wet snow

zone. Although the air temperature records suggest that melting has probably already begun in the percolation zone, neither K_0 nor K_3 show any indication of this, likely due to the downward percolation of the first fractions of meltwater into the snow and firn.

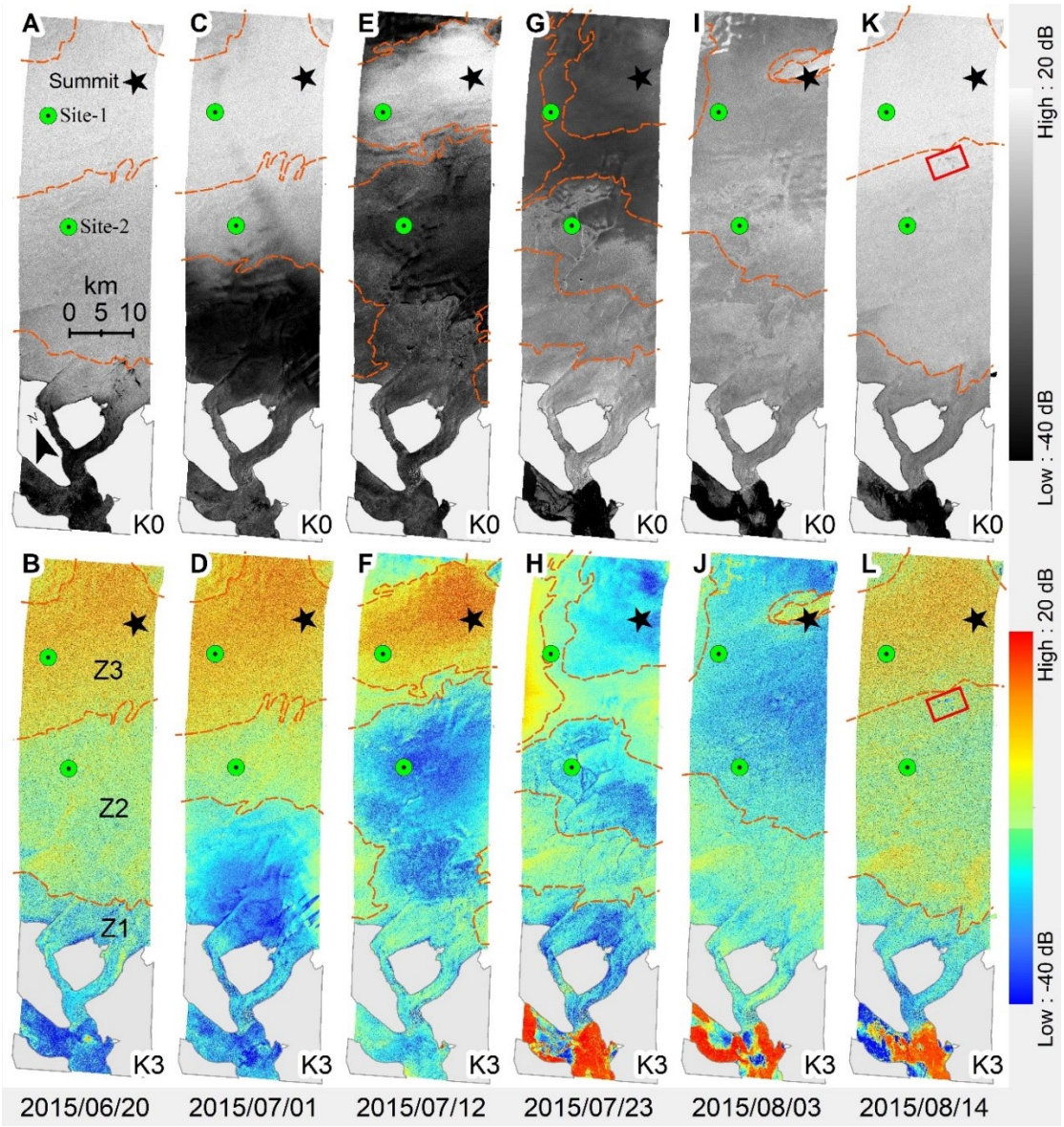

Figure 2.2 - TerraSAR-X images from June 20th of 2015 to 14th of August 2015 with a temporal resolution of 11 days. Z-1 corresponds to the Superimposed Ice and Bare Ice zones; Z-2 corresponds to the Wet-Snow zone; Z-3 corresponds to the Percolation zone. The red rectangle is the extent frame for the anomaly found on the image.

On July-12 2015 (Figure 2.2 frames E and F) almost all of the wet-snow zone has undergone melt and this zone exhibits low backscattering due to the high absorption caused by the presence of meltwater that inhibits reflection and limits transmissivity to just a few centimeters (Long and Drinkwater, 1994). This accounts for the dominance of surface scattering in K_3.

Obvious supraglacial meltwater channels are present in the images of July-23 2015 (Figure 2.2 frames G and H) although they are most obvious in the K_3 image. The percolation area, in which the summit is located, has undergone melt and exhibits less backscattering in K_0 than it did in the previous images, even though the snowpack is not completely water saturated as indicated by the moderate backscattering values. Deeply incised supraglacial channels can have widths ranging from 5 to 20 meters (Yang and Smith, 2016), and the edges of such channels may affect the strength of the backscattering signal as channels can cause corner reflector backscattering, thus producing high values of K_0 and surface scattering in K_3 (Figure 2.2 frames C and D). In addition, rough water surfaces, such as those likely to be found in channels on steep slopes, can lead to backscattering signals of varying strengths. Supraglacial channels are also visible in the images of July-9 2016 and August-9 2017 (Appendix A - Chapter 2

The image from August-3 2015 suggests there is considerably less meltwater on the ice cap surface on that date than in the image from July-23 2015, as indicated by moderate values of K_0 (Figure 2.2 frame I). The region surrounding the summit shows a high contribution from even bounce, which likely indicates that the snow has refrozen, while the percolation and wet-snow zones show a greater contribution from surface scattering, which suggests that meltwater is still available at the surface. The air

temperatures recorded by the AWS confirm that air temperatures dropped below 0°C on August 3rd at AWS Site-1, and on the following day at AWS Site-2. The images from July 23rd and August 03rd 2015 (Figure 2.2 - G-J) show a phenomenon common on radar images of Croker Bay where the water surface is so smooth that the transmitted signal is reflected away from the sensor, yielding very low backscattering in K_0 and a higher even bounce in the K_3 image (Wendleder, 2014).

In the last image of the 2015 series (Figure 2.2 frames K and L) the surface conditions of the ice cap, as defined by the locations of the facies boundaries, have essentially returned to their initial state, which coincides (with slight displacement compared to Figure 2.2 (A and B)) with the expansion of the wet-snow zone at the expense of the percolation zone in the upper parts of the ice cap, and of the superimposed and bare ice zones in the lower regions of the ice cap. Images from August 14 show an anomaly consisting of 5 areas that show the Kennaugh Elements K_0 and K_3 with backscattering signatures that are usually attributed to the Superimposed and Bare Ice zones although located at the upper boundary of the wet snow zone (the location of this anomaly is framed in red in Figure 2.2 frames K and L). This anomaly shows relatively low backscattering in K_0, suggesting that it may be a remnant of wet snow. The K_3 element shows a strong odd bounce consistent with surface scattering, which suggests that the transmission depth of the radar signal is limited to a few centimeters. This anomaly is compatible with the exposed ice found in the Superimposed and Bare Ice zones that are exposed at lower elevations on the ice cap after the removal of snow by summer melt. To investigate the nature of this anomalous radar backscattering, all images from 2015 to 2018 were analyzed.

2.5.1 Ice build-up anomaly

To better understand the anomaly we looked into the backscattering signature of the K_0 and K_3 elements in the images from the melt seasons of 2015 to 2018 with dates ranging from the begining of June to the end of August. Six AOI (areas of interest) of 9x9 pixels were collected in the region (red rectangle), three of which were placed over the anomaly area (Samples S1-S3) and the other 3 of which were placed in the immediate surrounding area (Samples S4-S6). The AOIs were moved slightly from year to year in order to accommodate any displacement caused by either the processing of the images or by the displacement caused by the nature of the anomaly and normal glacier flow. The dates and locations of the AOIs (Samples) are displayed in Figure 2.3 - Spectral signature of the Kennaugh Elements K_0 and K_3 for the year of 2015.. The anomaly was present from 2015 to 2017 but absent in 2018. For this reason, the placement of the 2018 samples is the same as was used in 2017. Only in 2015 and 2016 did the anomaly have a clear boundary. The absence of the anomaly in 2018 is likely due to the lack of substantial melting during that summer, coupled with the effects of summer snowfall that buried the region.

The backscattering signatures of the AOIs (Figure 2.3 - Spectral signature of the Kennaugh Elements K_0 and K_3 for the year of 2015.) show that the presence of the anomaly is linked to low backscattering in the K_0 element that is associated with melting, and to low backscattering in K_3 that is associated with odd bounce. Such behaviour is likely explained by the accumulation of meltwater in surface depressions underlain by a thick ice layer in the shallow subsurface that causes an odd bounce in K_3. In 2015 and 2016, years in which the anomaly had well-defined boundaries, it is possible to observe that, in the days following freeze-up (August 14, 2015 and August 11, 2016), both K_0 and K_3 discriminate

clearly between the samples located over the anomaly (S1-3) and those placed over the surrounding areas (S4-6) although the backscatter values differ by <5 dB. In 2017, the separability is also apparent in the image from August 20, although the backscattering difference is lower (<2 dB). In 2018, the anomaly is only visible in K_0, even though the boundaries are not well marked. This indicates a change in backscattering that is likely caused by the wetness of the surface even though the polarimetry remains the same, which could indicate water percolating down into the firn and freezing at depth.

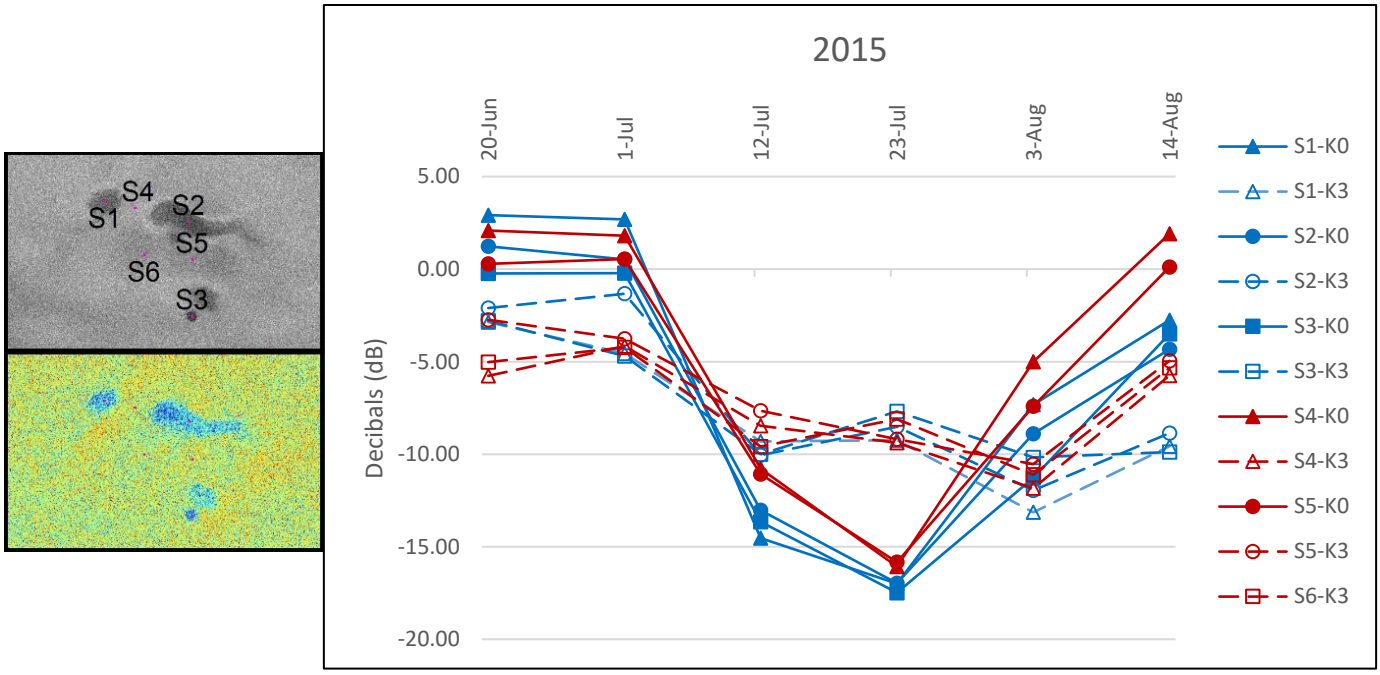

Figure 2.3 - Spectral signature of the Kennaugh Elements K_0 and K_3 for the year of 2015.

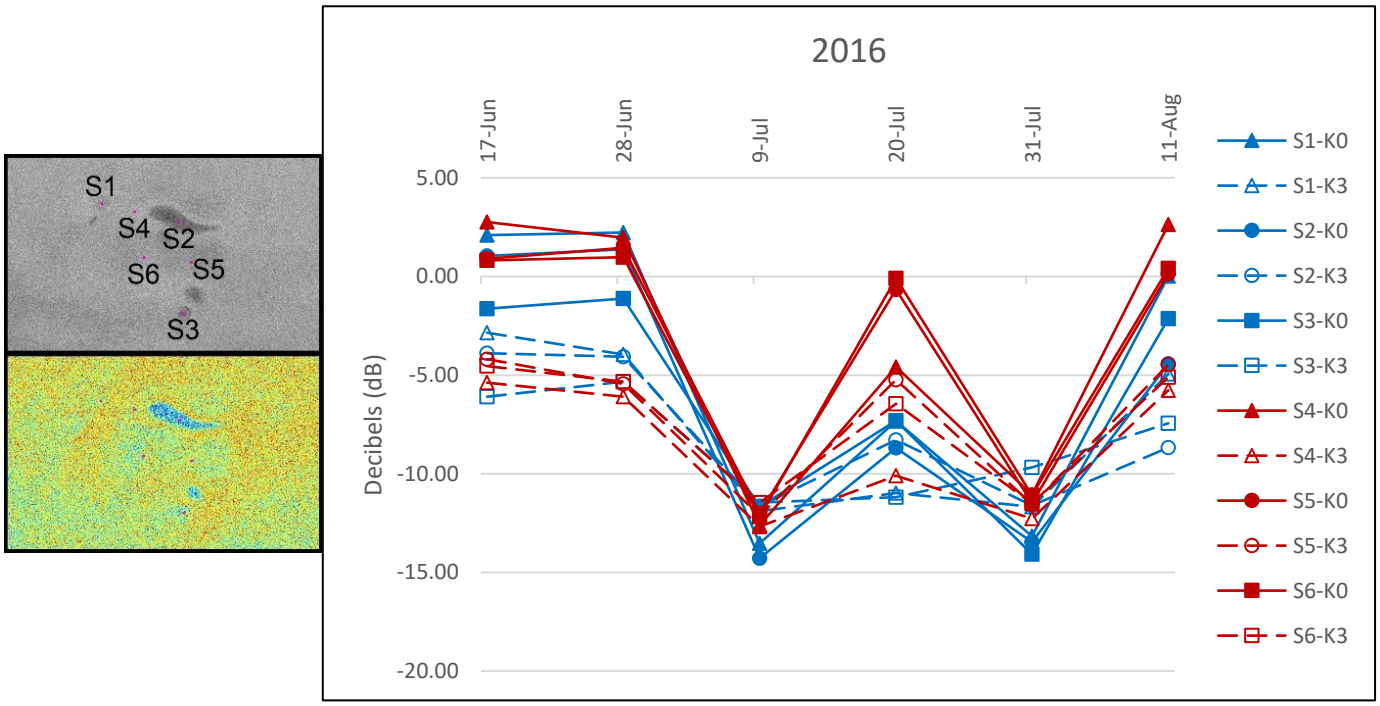

Figure 2.4 - Spectral signature of the Kennaugh Elements K_0 and K_3 for the year of 2016.

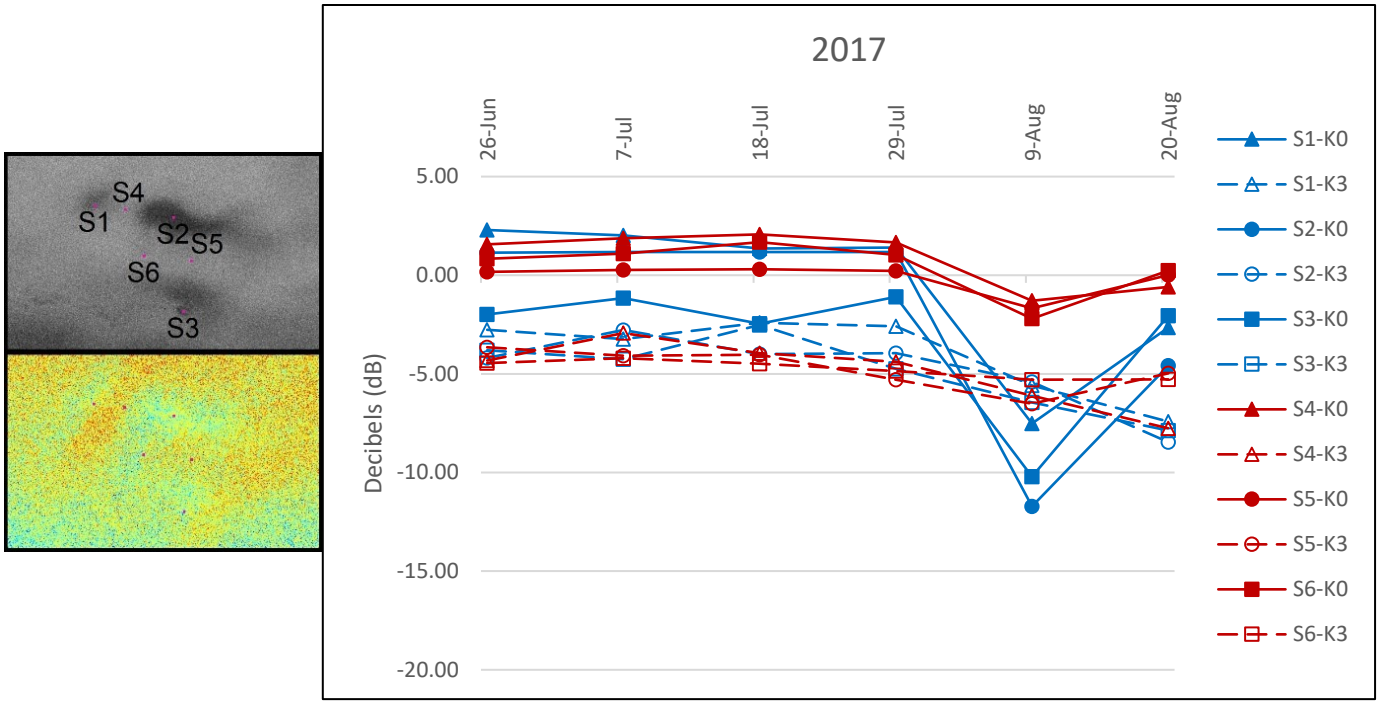

Figure 2.5 - Spectral signature of the Kennaugh Elements K_0 and K_3 for the year of 2017.

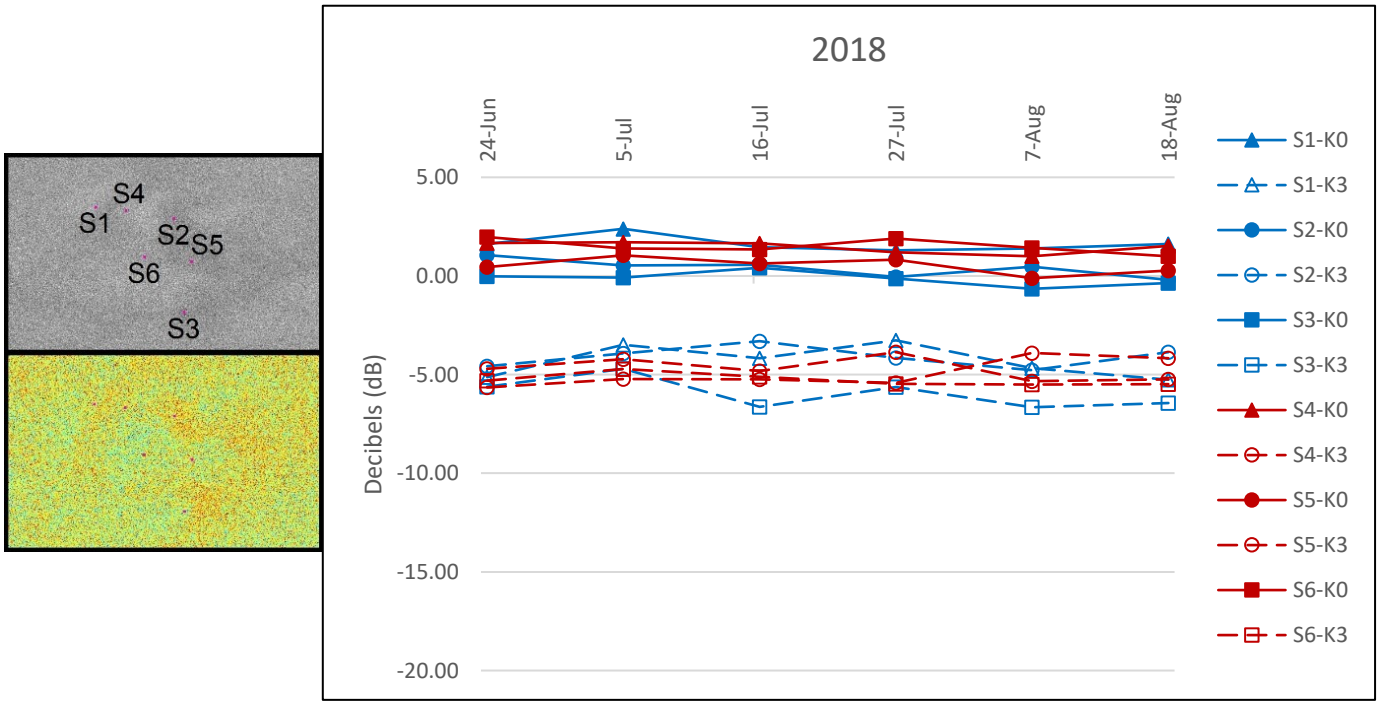

Figure 2.6 - Spectral signature of the Kennaugh Elements K_0 and K_3 for the year of 2018.

2.6 Conclusion

This chapter provides an application of the Kennaugh Decomposition technique to TSX dual-co-polarized imagery to study the seasonal evolution of surface melt and runoff patterns on the DIC, and the seasonal development of the supraglacial meltwater drainage network. The Kennaugh Elements K_0 and K_3, derived for 24 TSX images spanning the melt season, provide meaningful information about how the radar interacts with the snowpack and how this changes over the summer melt period. Using a combination of the total intensity of backscattering (K_0) and the polarimetric information (K_3) it is possible to detect the seasonal onset and end of surface melt on the ice cap. In situ records of surface air temperature are consistent with the dates of first appearance of surface meltwater on the ice cap and of end-of-summer freeze-up inferred from the TSX images, even though a small uncertainty in those dates (2 days) is inevitable because of the TSX revisit interval.

The decomposition technique proved to be extremely valuable for detecting the formation and distribution of supraglacial meltwater channels because the presence of liquid water in the percolation and wet-snow zones directly affects the intensity element (K_0). For these regions, the polarimetric information provided by the K_3 element makes it possible both to map the distribution of supraglacial meltwater channels and to differentiate the percolation and wet-snow facies. The sensitivity of the derived elements shows some potential for the detection of ice build-up across snow covered regions. Even so, in-situ measurements are critical to determine whether the proposed interpretation of the data is accurate, and whether the derived elements can be used in large-scale studies. Nonetheless, our results show that the Kennaugh technique has high potential for studying the seasonal

formation and evolution of supraglacial drainage systems in Polar Regions due to its adaptive multi-temporal characteristic.

Chapter 3 - SUPRAGLACIAL DRAINAGE NETWORK EXPANSION ON THE DEVON ICE CAP IN RESPONSE TO CHANGES IN THE SHALLOW SUBSURFACE HYDROLOGY OF THE FIRN COVERED AREAS

3.1 Introduction

Higher mean summer air temperatures over the Canadian Arctic since the mid-1990s have resulted in pronounced increases in glacier surface melt rates across the region (Gardner and others, 2011, 2013; Sharp and others, 2011; Fisher and others, 2012; Bezeau and others, 2013; Gascon and others, 2013). A 16-year record (2000–15) of mean summer land surface temperatures derived from satellite measurements (MODIS LST) over the Queen Elizabeth Islands shows glacier surface warming of ~1°C over the period (Mortimer, Sharp and Wouters, 2016). Associated increases in meltwater production, particularly at higher elevations, have altered the structure of the firn layer on the ice cap and accelerated the rate of firn densification (Bezeau and others, 2013; Gascon and others, 2013a). This has implications for the generation of supraglacial runoff at higher elevations on the ice cap and has changed the routing of meltwater from the ice cap through the development of an expanded supraglacial meltwater drainage network.

Surface melting and consequent supraglacial meltwater runoff are the largest sources of surface mass loss from glaciers and ice caps (Hock, 2005) and together accounted for 60–90% of the total mass loss from the Devon Ice Cap (DIC) during the period 1963–2000 (Mair, Burgess and Sharp, 2005). In areas where glacier ice is exposed at the surface in summer, meltwater is routed across the ice surface but, in firn-dominated areas at higher elevations, it will initially percolate downward into the pore volume of the firn layer (Pfeffer and Meier, 1991). Where the temperature of the firn is below the melting

point, the meltwater will refreeze, forming ice pipes, ice lenses, and discontinuous ice layers within the firn (Pfeffer and Meier, 1991; Pfeffer and Humphrey, 1996, 1998; Bøggild, Forsberg and Reeh, 2005; Humphrey, Harper and Pfeffer, 2012). With continued meltwater production, percolation, and refreezing, widespread and thick ice layers can develop within the firn to the point where they have the potential to impede downward percolation of meltwater. In recent years, such ice layers have been observed on both the DIC (Bezeau and others, 2013; Gascon and others, 2013a; Rutishauser and others, 2016) and the Greenland Ice Sheet (Machguth *et al.*, 2016a; Mikkelsen *et al.*, 2016). The release of latent heat during the refreezing of meltwater raises the temperature of the firn (e.g. Zdanowicz *et al.*, 2012; Gascon *et al.*, 2013), and, over time, reduces the firn's cold content, as exemplified by a 5.5ºC warming at a depth of 10 m on the summit of the DIC between 2004 and 2011 (Bezeau *et al.*, 2013). Once the temperature of the firn reaches the pressure melting point, meltwater draining vertically into the firn will fill the pore volume above the ice layers - unless it can drain through or around them (Harper *et al.*, 2012; Humphrey, Harper and Pfeffer, 2012). Once the firn becomes water-saturated, surface runoff will occur and meltwater produced on the surface can be routed down the surface slope via supraglacial meltwater channels or pool in surface depressions forming supraglacial lakes (Chu, 2014; Chen, Howat and De La Peña, 2017).

Ice layers within firn have been shown to affect the local hydrology. For instance, in the percolation zone on the western margin of the Greenland Ice Sheet in 2011, ice layers in the firn prevented deep percolation of surface melt which then led to the development of two supraglacial lakes (Chen and others, 2017). It has been hypothesized that the presence of these impermeable ice layers might affect the regional hydrology by promoting

surface runoff from firn-covered areas without the total pore volume having to be filled (Mikkelsen *et al.*, 2016). However, research has yet to directly evaluate the impact of such ice layers on the regional hydrology and, specifically, on the development of supraglacial drainage networks. This study addresses this knowledge gap by investigating the degree to which ice layers in the upper part of the firn may affect the development and persistence of supraglacial drainage networks in a firn-covered area of the DIC.

To evaluate how surface slope and ice layer distribution influence supraglacial channel development on the southern flank of the DIC, we begin by characterizing the supraglacial drainage network that existed in a firn-covered area between 2000 and 2017 using Landsat-7/8 imagery. Observed inter-annual variations in the DIC's supraglacial drainage network are compared with the distribution of glacier facies zones and in-situ air temperature records. To identify supraglacial channels with locations that are exclusively topographically-controlled we used a digital elevation model (DEM) to predict the supraglacial drainage network that would be expected to develop if the glacier surface was impermeable to water. The distribution of impermeable ice layers within the firn is then inferred from a comparison of the expected distribution of topographically controlled channels (derived from the DEM) and the actual channel distribution (derived from Landsat imagery) which is likely to also be influenced by the presence or absence of impermeable ice layers in the firn (subsurface).

3.2 Background

3.2.1 Glacier Facies Zones

Müller (1961) and Benson (1962) recognized five distinct facies zones on glaciers. From highest to lowest elevation, these are the Dry-Snow zone, the Percolation zone, the Wet-Snow zone, the Superimposed Ice zone, and the Bare Ice zone. Only the latter four of these occur on DIC (Gray *et al.*, 2015). The dry-snow zone, which is characterized by the complete absence of melt even in the peak of summer, is absent on the DIC and a "quasi-dry snow zone" – in which melting historically occurred in some, but not all, summers – has not been observed since ~ 2004–06 (Sylvestre and others, 2013; de Jong and others, 2018).

The percolation zone, where surface meltwater percolates into the snowpack and refreezes to form ice pipes, lenses and discontinuous ice layers (Benson, 1962), is widespread at higher elevations on the DIC. The amount of ice formed by refreezing of meltwater in snow and underlying firn in this zone during a given melt season generally increases with decreasing elevation. The boundary between the percolation and wet-snow zones is defined by the Wet-Snow Line (WSL), where, by the end of a summer, the temperature of the snow accumulated since the end of the previous summer has been raised to the pressure melting point and the snow has become water saturated (Cogley *et al.*, 2011). The lower elevation limit of the wet-snow zone, referred to as the Snow Line (SL), demarcates the boundary between the accumulation area and the ablation area (Cogley *et al.*, 2011).

Below the SL is the Superimposed Ice zone, a region in which meltwater refreezes to the upper surfaces of either glacier ice or superimposed ice that formed in previous years

(Singh, Singh and Haritashya, 2011). This zone usually occupies a small fraction of the glacier surface and the boundary between it and the Bare Ice zone coincides with the Equilibrium Line, which separates the accumulation and ablation areas of the glacier. Bare ice is exposed in the ablation area during the summer by the melting of the snow that accumulated during the previous winter and its runoff as glacial meltwater (Benson, 1962).

3.2.2 Supraglacial Drainage Network

Supraglacial meltwater drainage networks play an important role in evacuating meltwater from glacier surfaces by routing water across the glacier to its margins, or to moulins and crevasses by which it may penetrate to the glacier bed (Iken *et al.*, 1983; Palmer *et al.*, 2011; Phillips *et al.*, 2013; Yang and Smith, 2013). Water reaching the glacier bed can lubricate the base of the glacier and affect the rate of glacier flow (Iken, 1972). Although the development of supraglacial drainage networks in the ablation zone is long established, supraglacial channels and lakes can also develop in the accumulation zone, for example above the ice layer at the interface between the wet-snow zone and superimposed ice and/or bare ice zones (Ferguson, 1973). Local flat areas or depressions in the accumulation zone can become collecting points for meltwater that can either saturate the surface snowpack and form slush areas (Fountain, 1996), or, if the meltwater supply is sufficient, collect on the surface and form supraglacial lakes (Chu, 2014; Chen, Howat and De La Peña, 2017).

A recent study of the Greenland Ice Sheet's surface hydrology found that supraglacial channels can form from channels created by water-saturated slush flows in the lower wet-snow zone (Chu, 2014), especially in areas with steep surface slopes, where failure of the water-saturated snowpack promotes slush avalanches or slush flows that

carve channels into the snow and firn (Marston, 1983). Even though supraglacial channels extending into the wet-snow zone are not widely documented, they have been observed (July 1999) at the heads of major outlet glaciers in the percolation zone of the northeastern DIC (Wyatt, 2013) and were widespread on steeply sloping sections of John Evans Glacier, Ellesmere Island in late May and June in the mid 1990s (Boon and Sharp, 2003). The presence of these channels is important because they can become the focus of lateral inflow of meltwater from the surrounding area (Gleason *et al.*, 2016). If surface meltwater flow persists throughout the melt season, these incipient meltwater channels can evolve into large supraglacial meltwater channels (Karlstrom, Gajjar and Manga, 2013). Supraglacial drainage channels typically form in the same location from year to year because they are routed in the direction of steepest surface slope (Cuffey and Paterson, 2010). Their networks are usually dendritic, except where crevasses, moulins, or topographic features (such as the longitudinal ridges created by differential melting of clear and bubbly ice layers within foliated glacier ice) disrupt the surface flow and produce 'trellis-like' drainage patterns (Sugden and John, 1976; Nienow and Hubbard, 2005).

3.3 Study Site

The influences of surface slope and buried ice layers on the development of supraglacial channel networks in firn-dominated areas were investigated for a 1757 km^2 area of the Croker ice divide region on the Southern flank of the DIC (GLIMS; NSIDC;, 2005, updated 2017). The lower boundary of this region is defined by the 800 meter elevation contour, which approximately defines the elevation of the equilibrium line in this part of the DIC (Casey and Kelly, 2010; Gray *et al.*, 2015). The maximum elevation along the ice divide which defines the upper limit of the study area is 1827 m a.s.l. The study

area is comprised of five distinct supraglacial drainage basins (Figure 3.1). Basin 1 (~317 km²), in the westernmost part of the study area is characterized by stagnant ice (Van Wychen *et al.*, 2012), while Basins 2–5, in the central and eastern parts of the study area, drain the North and South Croker Glaciers. Although the supraglacial hydrology of the DIC was previously characterized and reported on by Wyatt (2013) for a single year (1999), the inter-annual variability in this region's supraglacial drainage network has not yet been documented. In 1999, the distribution of supraglacial channels in the Croker ice divide region was limited to the area below the percolation zone, up to a maximum elevation of 1420 m a.s.l. A small number (low density) of lakes was also found in surface depressions in this region (Wyatt and others, 2013). These lakes either froze in situ at the end of the melt season or drained to downstream sink points (<600 m a.s.l.) via supraglacial channels.

Near-surface (2m) air temperatures for the period 2004–16 are available from two sites (Site-1: ~1800 m a.s.l., Site-2: ~1400 m a.s.l.) located in the upper part of the study area (Figure 3.1**,** Table 3.1**;** see Gascon and others (2013b) for instrumentation specifications). Melt onset, defined as the first day on which the mean daily 2-m air temperature reached 0°C, occurred between DOY 163 (2016) and 217 (2013) at the higher elevation Site-1, and between DOY 161 (2016) and 203 (2004) at the lower elevation Site-2. Freeze-up, defined as the first day on which the mean daily 2 m air temperature dropped below 0°C at the end of the summer melt season, occurred between DOY 190 (2005 and 2006) and 240 (2016) at Site-1, and between DOY 203 (2004) and 242 (2016) at Site-2. Mean daily air temperature during the melt season ranged from -2.97°C (2016) to 0.27°C (2013) at Site-1 and -2.51°C (2013) to 1.06°C (2015) at Site-2. The number of individual days within each melt season with a mean daily air temperature >0°C ranged from 5 (2013)

to 19 (2015) at Site-1 and 18 (2013) to 44 (2010) at Site-2, while the positive degree day sum ranged from <1°C (2005) to 69°C (2008) at Site-1 and from <1°C (2004) to 68°C (2010) at Site-2.

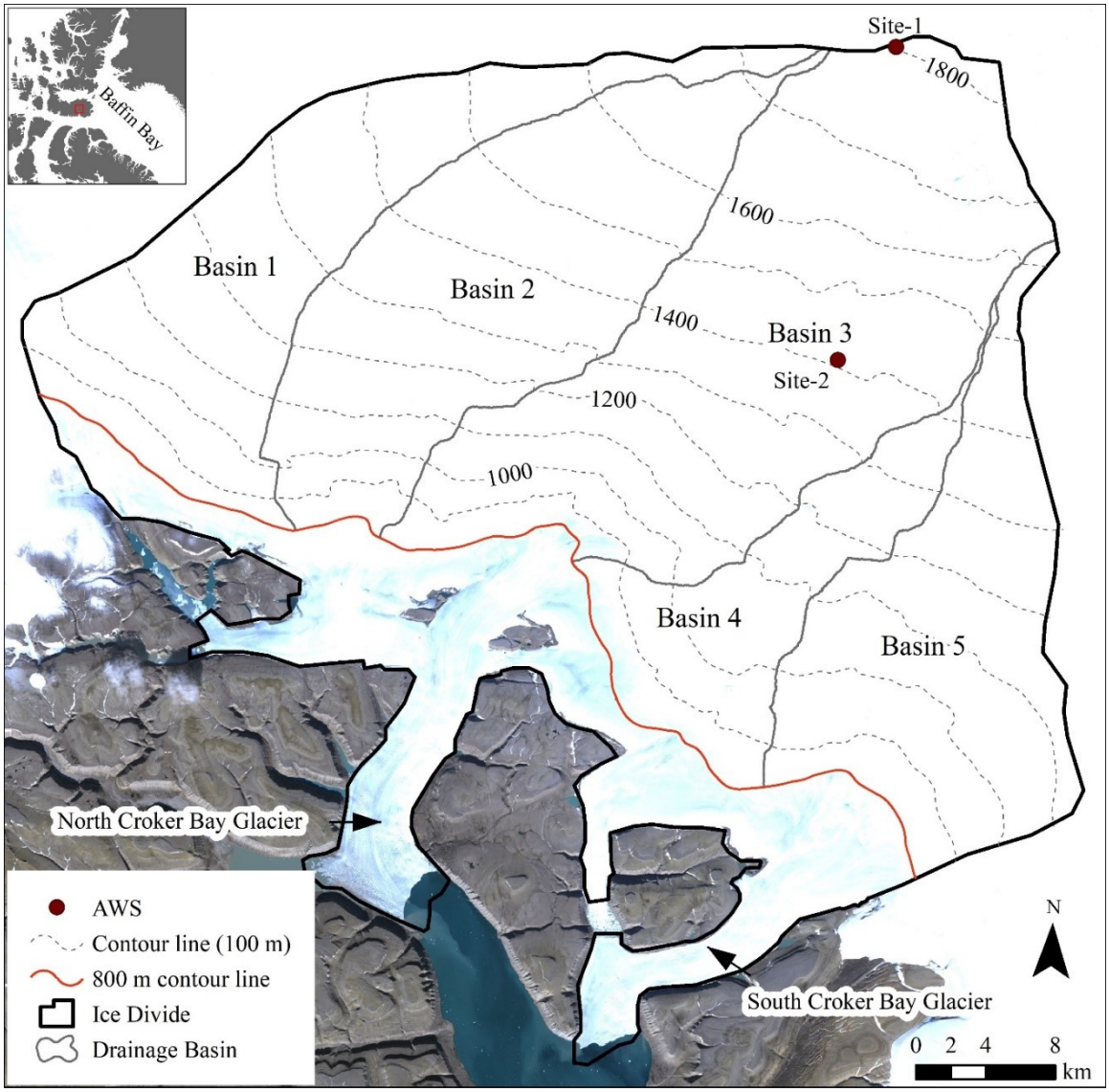

Figure 3.1 - Map of the Croker ice divide region, DIC. The 800 m contour line demarcates the lower boundary of the study area. Site-1 AWS is located in the percolation zone ~1800 m a.s.l., Site-2 AWS is located in the wet-snow zone ~1400 m a.s.l. Background image: Landsat 8, 29 August 2016.

Table 3.1 - Dates of melt onset and freeze-up, melt duration, and positive degree day sum at Sites 1 and 2 for summers from 2004-2016 (Updated from Gascon, 2013b). Hyphen indicates no data.

		2004	2005	2006	2007	2008	2009	2010	2011	2012	2013	2014	2015	2016
SITE 1	Melt onset (DOY)	-	190	190	181	179	-	183	182	179	217	196	181	163
	Freeze-up (DOY)	-	190	228	200	225	-	234	222	219	223	214	215	240
	Melt duration (days)	-	1	39	20	47	-	52	41	41	7	19	35	78
	PDD sum (°C)	-	0.1	38	11	69	-	20	15	19	5	12	30	16
SITE 2	Melt onset (DOY)	203	189	191	177	174	193	165	167	171	158	178	180	161
	Freeze-up (DOY)	203	210	230	223	223	238	239	232	219	224	214	216	242
	Melt duration (days)	1	22	40	47	50	46	75	66	49	67	37	37	82
	PDD sum (°C)	0.6	8	34	51	52	51	68	60	67	29	27	44	54

3.4 Data and Methods

3.4.1 Landsat

Optical satellite imagery acquired by the Landsat-7 Enhanced Thematic Mapper Plus (ETM+) (1999–present) and Landsat-8 Operational Land Imager (OLI) (2013–present) instruments over the period 2000 to 2017 (Appendix B - Chapter 3 - Table 1) was used to delineate the supraglacial drainage network (supraglacial channels and lakes) and to map the distribution of glacier facies zones in every year for which imagery was available. These sensors provide coverage of the surface of the study area along the same path/row every 16 days under cloud-free conditions at spatial resolutions of 15 m (panchromatic band) and 30 m (visible and near-shortwave infrared). Due to the high latitude of the study area and the near-polar orbits of the satellites, near daily coverage of the study area can be obtained using different path/row combinations.

Failure of the Landsat-7 ETM+ sensor's scan line corrector introduced striping towards the edges of the scenes beginning in 2004. To address this issue, all Landsat-7

images from 2004 onward were gap-filled using the code proposed by Scaramuzza and others, (2004) and obtained from the Center of Earth Observation, Yale University (https://landsat.usgs.gov/sites/default/files/documents/SLC_Gap_Fill_Methodology.pdf).

In situ air temperature records (Table 3.1) collected during the study period (2000–17) indicate that melt onset occurred as early as 10 June. Inspection of June Landsat imagery (2000, 2008, 2010, 2011 and 2012) shows incipient formation of short supraglacial channels (longest observed segment < ~1.5 km) and slush areas in late June (earliest observation 25 June 2010) in lower elevation parts of the study area. As a result, the supraglacial drainage network was only digitized for the months of July and August when melt was generally more widespread and intense.

3.4.1.1 *Supraglacial Drainage Network Mapping*

Remotely sensed imagery has been used widely to manually delineate supraglacial meltwater channels (e.g. Lampkin and Vanderberg, 2014; Wyatt and Sharp, 2015; King and others, 2016; Yang and Smith, 2016). Although recent studies have demonstrated the ability to map supraglacial drainage networks automatically from high-resolution optical data and digital elevation models (e.g. Yang and Smith, 2013; Smith and others, 2015; Yang and others, 2015a; 2015b; King and others, 2016), for this work, supraglacial channels and lakes were digitized manually due to constraints on the data available arising from time-variable cloud cover and irregular temporal coverage, along with the high spatial and temporal variability in the extent and distribution of supraglacial drainage channels and lakes.

The supraglacial drainage network was digitized manually from panchromatic images, and cross-validated with true-color composites. To ensure consistency during manual digitization, locked scales of 1:5000 and 1:10000 were used for lakes and supraglacial channels, respectively. As this study focuses on supraglacial channels in firn areas, channels in the bare ice zone (below ~800 m a.s.l.) were not digitized. Because of the transient nature of supraglacial channels, and to permit investigation of the variability in the location of supraglacial channels over the course of each melt season, supraglacial channels were digitized from multiple images acquired during July and August. The combined length of the digitized channels in a given year was then used for inter-annual comparisons.

For each year during the period 2000–17 for which imagery was available, a map displaying the aggregate extent of the observed supraglacial drainage network was produced. As there was insufficient imagery to map channels in 2003 and 2004, supraglacial channels were mapped for only 16 of the possible 18 years. The digitized channel networks for each year were converted from vector to raster (30 m pixels) format and summed to produce a single map showing the total number of years in which a particular channel, or channel segment was observed. This final map allowed examination of the persistence of supraglacial channels over the study period. Finally, to investigate the seasonal evolution of the supraglacial drainage network over the course of each melt season (intra-annual variability), the acquisition dates of all images used to delineate supraglacial channels and lakes were recorded.

Supraglacial lakes, the presence of which can indicate highly impermeable ice in the substrate (Fountain and Walder, 1998), were also mapped. For each year, the aggregate

extent of lakes was mapped from all available July and August cloud-free imagery (Appendix B - Chapter 3 - Table 1). A map showing the aggregate extent of supraglacial lakes was produced for each year for which imagery was available. Lake polygons were summed across all years to produce a single map showing the number of years in which a particular lake, or pond, was observed. In addition to being used to characterize the supraglacial drainage network, the locations of lakes were used to validate the representation of surface topography in the ArcticDEM (section 3.4.2).

Difficulties in mapping the aggregate extent and seasonal evolution of the drainage network arose firstly from the loss of information when clouds were present, and secondly from differences in timing between the occurrences of surface melt and/or drainage events and image acquisitions. To limit data gaps when clouds were present, all available July-August images were used. The combination of the highly variable and transient nature of supraglacial channels and the discrete nature of satellite observations means that, even under cloud-free conditions, information about changes in the occurrence and distribution of surface melting and the development of the supraglacial drainage system was not captured when these changes occurred during the time gaps between available images. Finally, differences in image availability between years may suggest inter-annual variability in the mapped supraglacial channel networks that is not physically real. However, investigation of the relationship between image availability and the extent and distribution of mapped channels found no clear relationship between the total number of images available in a given year and the total length of supraglacial channels that was mapped (Figure 3.2).

In most years, six to seven images were available to map the supraglacial channel network. Exceptions to this were 2002, 2006, 2009 and 2011, when only two or three images were available in each year.

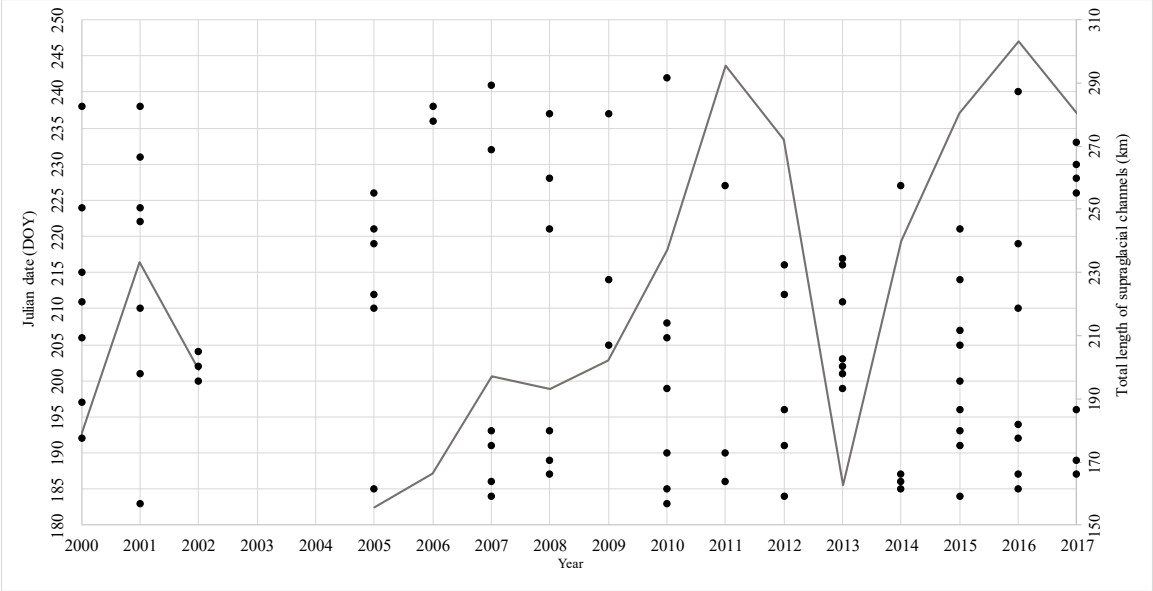

Figure 3.2 - Temporal distribution of images used in the analysis (dots) as a function of DOY, left-hand axis, and the total length (km, right-hand axis) of supraglacial channels in each year of the study period for which suitable imagery was available (solid line).

The mapped supraglacial channels were classified as either *'Regular'* or *'Irregular'*. *'Regular'* channels are defined as those that were continuous along their length during the same year (as observed from either a single image or multiple images) and that appeared in the same location in multiple years. If the full length of a particular channel was not always visible every year, the channel was classified as an *'Irregular'* channel. *'Irregular'* channels are spatially discontinuous channels in which the upper and/or lower reaches are visible, but the middle section is not. This occurs either because the channel is routed englacially in some places, or because there are differences in timing between periods of image availability and meltwater production. We did not differentiate between

'Irregular' channels and channel segments (whose discontinuous nature was likely the result of limited image availability) and channels for which there was a clear physical explanation for observed discontinuities.

3.4.1.2 *Glacier Facies Zone Mapping*

To investigate the relationship between the development of the supraglacial drainage network and changes in the extent and/or distribution of glacier facies zones in the years 2000, 2001, 2005–12, 2015 and 2016, the distributions of the different glacier facies zones and the respective locations of the SL and WSL were mapped from Landsat-7/8 imagery. Insufficient imagery was available to permit the classification of glacier facies zones in the years 2002–04, 2013–14, and 2017. Pixels were assigned to one of three classes corresponding to the combined bare-ice and superimposed ice zones, the wet-snow zone, and the percolation zone, using a maximum likelihood classification applied to the visible bands. The classified images were then used to delineate the annual mean positions of the SL and WSL. For each year, the spatial mean, minimum, and maximum elevations (and their standard deviations) of the SL and WSL were delineated for the July–August period

3.4.1.3 *Uncertainty Assessment: Landsat-derived supraglacial channels*

The four principal sources of uncertainty associated with the positioning of the mapped meltwater channels arose from: (a) the georeferencing accuracy inherent to the Landsat data, (b) image co-registration uncertainty, (c) pixel size and (d) human error introduced during the digitization process. All but one of the images used in the analysis were Tier 1 images (Landsat inventory structure based on data quality and level of

processing) which have an inter-calibrated accuracy (RMSE) of 50 m in Arctic Regions (https://landsat.usgs.gov/geometry). Positional uncertainty attributable to different path/row combinations was estimated by co-registering all path/row combinations used in the analysis. The highest RMSE (0.98 m) was included in the estimation of the total uncertainty. Uncertainty (*d*) in positioning related to pixel size (15 m) was taken as the square root of the sum of squares in both the x and y dimensions (eq. 1),

$$d = \sqrt{x^2 + y^2} \quad (1)$$

where x and y are the pixel dimensions; yielding an uncertainty of 21.21 m. To quantify the uncertainty attributable to manual digitization and image interpretation, a representative ~42 km long channel segment was repeat-digitized five times and differences in channel length and location were estimated. To be conservative, the largest (lateral) positional difference (90 m) was included in the total uncertainty estimate. The uncertainty in the location of the mapped supraglacial channels, taken as the straight sum of all four sources of uncertainty, is 162.19 m.

3.4.2 ArcticDEM

3.4.2.1 *Supraglacial Drainage Network Modeling*

To assess the degree to which the morphology and extent of the observed supraglacial drainage network are controlled by the near-surface topography, a modeled surface drainage network was generated from the ArcticDEM 7th release and compared with the drainage network mapped from Landsat-7/8 imagery. The ArcticDEM 7th release, 2m spatial resolution, was obtained from the University of Minnesota's Polar Geospatial Center (https://www.pgc.umn.edu/ - downloaded 29 Oct 2018). This time-varying DEM

is produced primarily from WorldView 1–3 stereo imagery. However, its horizontal and vertical accuracies have yet to be verified ('ArcticDEM Documentation and User Guidance', 2017).

An eight-directional hydrological flow routing model, implemented in ArcGIS (Jenson and Domingue, 1988), was used to model the expected surface meltwater drainage network from the topography in the ArcticDEM. Before modeling the surface drainage network, closed depressions (sinks) were filled. To assess the impact of the sink-filling process, which was necessary to produce continuously flowing channels (Li and Wong, 2010; Yang and others, 2015b), the DEM was inspected to check whether sinks in the DEM were physically real (associated with surface lakes) or whether they were data artefacts (products of noise in the data). Comparison of sink locations with digitized lakes (see section 3.4.1.1) showed that <4.5% (~0.1 km^2) of the sink locations overlapped with the digitized water bodies. Thus, filling the sinks did not compromise the modeled supraglacial channel network as the majority of sinks represent either very small surface depressions or DEM noise.

Supraglacial channel modeling was conducted on the post-processed (sink-filled) DEM. For each pixel, flow direction was determined using a 3x3 window (surrounding the central pixel) and the flow accumulation was determined from a summation of the number of pixels contributing flow to the central pixel. A flow accumulation threshold, whereby pixels with higher accumulated flows are selected to generate a channel network, was determined iteratively (Li and Wong, 2010). Larger flow accumulation thresholds consistently resulted in a smaller number of channels while smaller thresholds resulted in many spurious channels. For this study, the threshold that generated the channels that best

aligned with the observed channels was selected. Specifically, the flow accumulation threshold was increased by increments of ten up to a point at which the modeled channel extent overestimated the extent of any of the mapped (Landsat-derived) supraglacial channels and then reduced by one iteration to generate the final modeled network.

3.4.2.2 DEM Uncertainty Assessment

The uncertainty associated with the ArcticDEM arises from the co-registration uncertainty (RMSE) of all images used to generate the DEM, and from the DEM pixel size. The co-registration uncertainty of all image pairs used to generate the DEM over our study area (Appendix B - Chapter 3 - Table 2) was obtained from the ArcticDEM Explorer website (https://livingatlas2.arcgis.com/arcticdemexplorer/). The average RMSE in both the x and y dimensions (±1.9 m and ±0.4 m, respectively) was used to estimate the total co-registration uncertainty (2.02 m) from the sum of squares (eq.1).The uncertainty related to pixel size (2 m) was 2.82 m (eq. 1), yielding a total positional uncertainty of 4.84 m for the DEM.

3.5 Comparison between the mapped and modeled drainage networks

The modeled supraglacial drainage network is derived based on the assumption of an impermeable surface. Thus, the surface topography is the only control on the location and flow direction of modeled supraglacial channels. The modeled network provides a benchmark against which the observed supraglacial drainage network (which is the result of the combined effects of surface topography, variations in surface and near-surface permeability, and the distribution of other drainage features such as the presence of moulins

and crevasses – absent from the study area as during the study period only moulins and crevasses that occur below 800 m a.s.l. can be mapped.

To compare the mapped and modeled channel patterns, a buffer equal to the combined DEM (section 3.4.2.2) and Landsat (section 3.4.1.3) uncertainties (167 m rounded up to 170 m to be conservative) was applied to the modeled channels. The mapped supraglacial channels for each year were then intersected with the buffered modeled channels (DEM-derived, section 3.4.2.1), (Figure 3.3). When superimposing the mapped and modeled supraglacial channels, three scenarios can occur: (a) presence of both mapped and modeled channels, (b) presence of mapped channels and absence of modeled channels, and (c) absence of mapped channels and presence of modeled channels. The presence of mapped and modeled networks (scenario a) is expected to occur where the surface topography is the main control on the location of supraglacial channels and the subsurface is sufficiently impermeable to support supraglacial runoff. A supraglacial channel in a location not predicted by the modeled drainage (scenario b), indicates that surface topography is not the main control on the location of that channel and may indicate the presence of an extensive impermeable ice layer in the near-surface part of the firn that inhibits vertical percolation of surface meltwater. Scenario c is expected where the firn layer is sufficiently deep and permeable for vertical percolation of meltwater to occur, making it impossible for an observable supraglacial channel to develop.

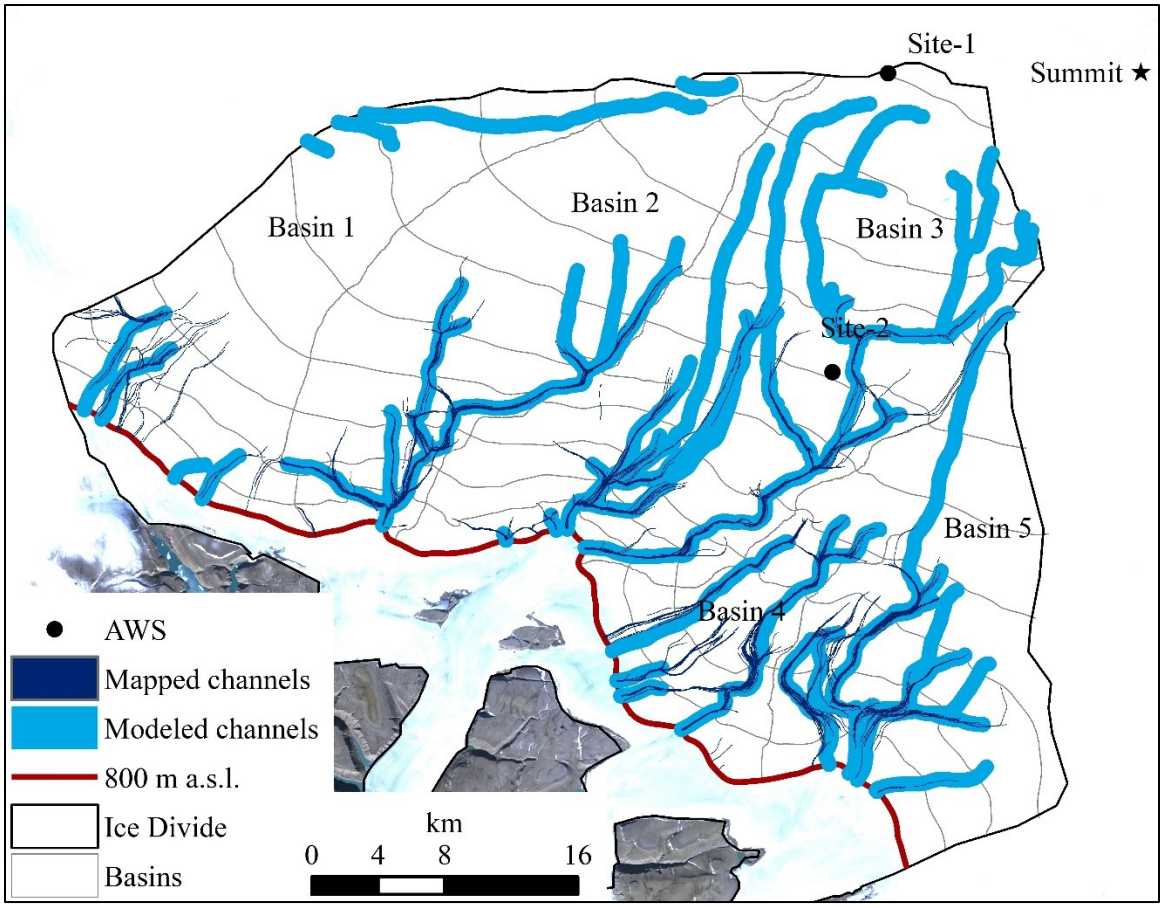

Figure 3.3 – Distribution of modeled (DEM derived) channels and all mapped channels during the period 2000-2017.

3.6 Results

To investigate the influences of surface slope and the presence of ice layers buried in the firn on the distribution and geometry of supraglacial drainage networks in firn-dominated areas, the principal glacier facies zones, supraglacial lakes, and supraglacial channels were mapped for the period 2000–17 using all the available data. These records were then evaluated in the context of available near-surface air temperature measurements to determine the influences of melt and, potentially, the presence of ice layers in the firn, on the observed surface drainage patterns. Then, the influence of surface slope on the locations of observed supraglacial channels is investigated through a comparison with the modeled supraglacial drainage network.

3.6.1 Classification and distribution of glacier facies zones

The mean elevations of the SL and WSL during the study period were 924 m a.s.l. and 1365 m a.s.l., respectively (Figure 3.4**)**. These values are in general agreement with estimates based on analyses of QuikScat scatterometer data for the period 1999–2005 (Wolken, Sharp and Wang, 2009), and with estimates derived from mass-balance approaches using satellite laser altimetry (ICESat) and gravimetry (GRACE) for the period 2004–09 (Gardner and others, 2011; 2013). Between 2000 and 2016, the (spatially-averaged) mean elevation of the SL ranged from 870 m a.s.l. (2006) to 978 m a.s.l. (2016), while that of the WSL ranged from 1221 m a.s.l (2011) to 1553 m a.s.l. (2012). Within a given July–August period, the elevation of the SL varied less than that of the WSL. The standard deviation of the spatially-averaged mean SL elevation ranged from 41 m (2007) to 57 m (2008) while that of the WSL varied between 30 m (2016) and 228 m (2006) (Figure 3.5).

The elevation of the WSL, which demarcates the percolation zone from the wet snow zone, ranged from 1221 to 1418 m a.s.l. during the period 2000–11. In 2012 there was a marked shift of the WSL to higher elevations (1553 m a.s.l.) and there was a commensurate reduction in the area of the percolation zone from 954 km² in 2011 to 295 km^2 in 2012. In 2015 and 2016 the elevations of the WSL (2015: 1492 m a.s.l., 2016:1495 m a.s.l.) and the areas of the percolation zone (2015: 388 km², 2016: 383 km^2) appear to have (temporarily) stabilized. Like that of the WSL, the elevation of the SL was fairly stable between 2000 and 2011 (ranging from 870 to 941 m a.s.l.). However, while the elevation of the WSL increased markedly in 2012, that of the SL experienced a much smaller change in its mean elevation in 2012 (961 m a.s.l.). The SL was higher again in 2015 (969 m a.s.l)

and 2016 (978 m a.s.l.) and there was a commensurate reduction in the area of the wet-snow zone from 1217 km^2 in 2012 to 1097 km^2 in 2016.

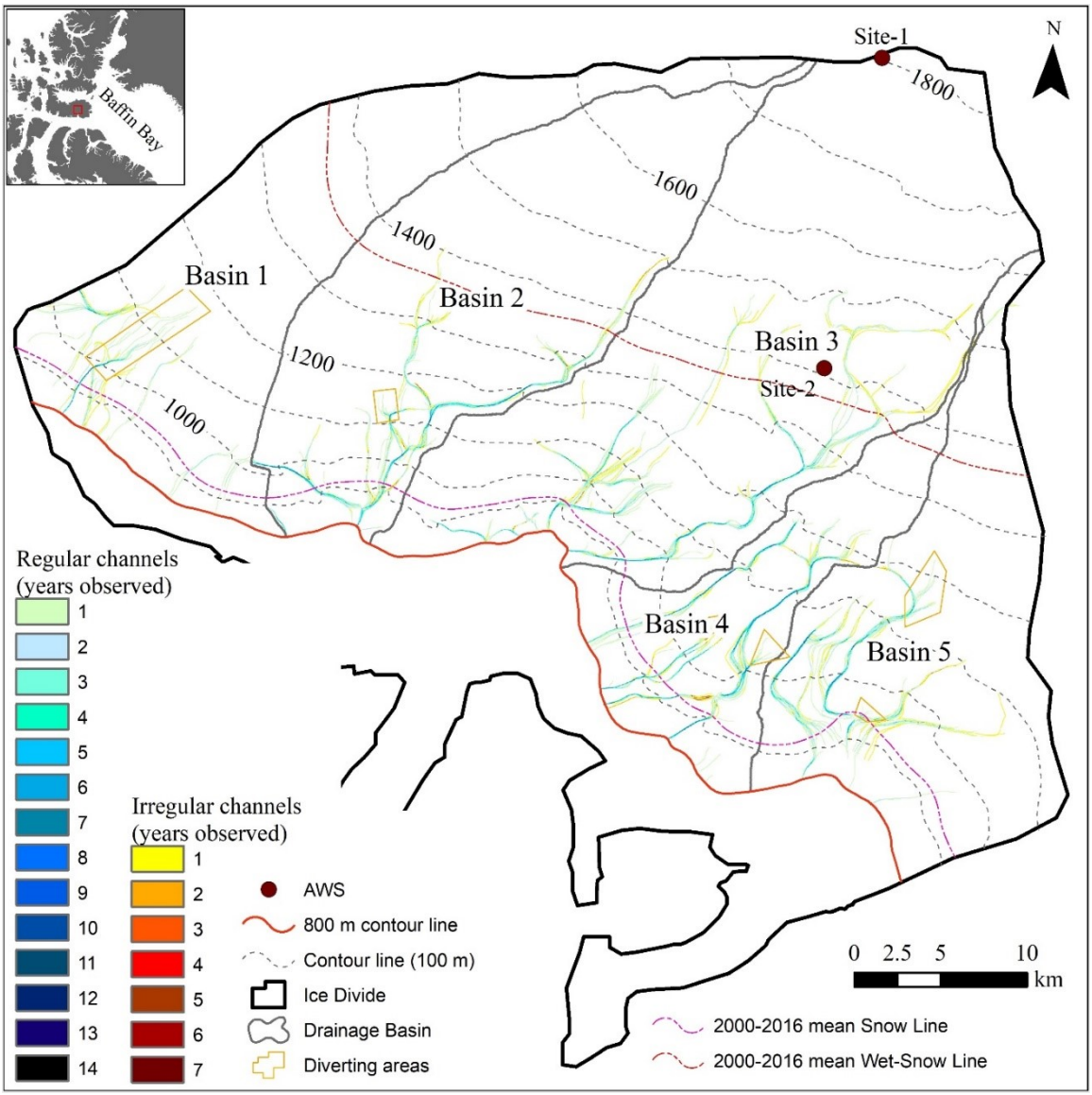

Figure 3.4 - The number of years in which 'Regular' or 'Irregular' channels or channel segments were observed between 2000 and 2017. See Section 4.1.1 for comprehensive definition of Regular and Irregular channels. The 800 m contour line demarcates the lower boundary of the study area.

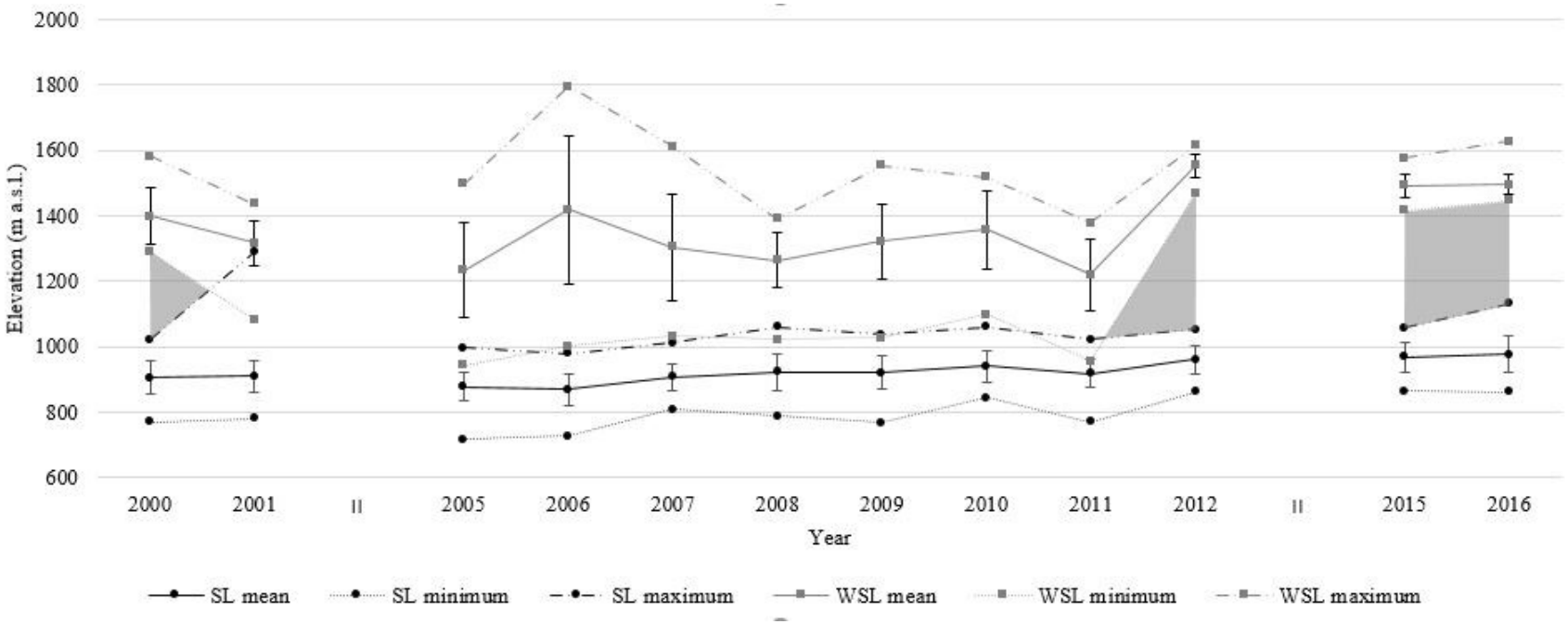

Figure 3.5 - Spatially-averaged minimum (dotted line), mean (solid line), and maximum (dashed line) Snow line (grey) and Wet Snow Line (black) elevations with standard deviation (vertical bars) over the period 2000–16. The shaded (grey) area highlights the time period when there was clear separation between all three glacier zones, with no overlap between the maximum SL elevation and the minimum WSL elevation.

3.6.2 Supraglacial lakes

Supraglacial lakes were mapped at 16 different locations in the study area during the study period (Table 3.2; Figure 3.6). These lakes ranged in size from 0.01 km² to 0.39 km². In nine locations, lakes were observed in at least six of a possible 16 years. This suggests that the locations of these lakes are controlled by the underlying bedrock topography as opposed to glacier flow (Echelmeyer *et al.*, 1992; Lampkin and Vanderberg, 2011; Selmes, Murray and James, 2011). In five locations (Lakes 10, 11, 12, 15 and 16), lakes were observed in only one year (Lake 10 in 2009, Lake 11 in 2011, Lake 12 in 2015 and Lakes 15 and 16 in 2016). The two most frequently occurring lakes (Lakes 1 (15 years) and 2 (16 years)) are located between 918 and 943 m a.s.l.. Up until 2015, four to eight lakes were typically mapped in each year and they were confined to elevations below 1198 m a.s.l.. In 2015, eleven lakes were observed and the aggregate lake area (1.36 km²) was nearly double the 2000–17 average (0.79 km^2). In 2015, two lakes (Lakes 13 and 14, total area: 0.06 km^2) were located in the percolation zone, at elevations of 1614 and 1590 m a.s.l., respectively. These lakes reappeared in the same locations the following year, albeit with a smaller total area (0.04 km^2).

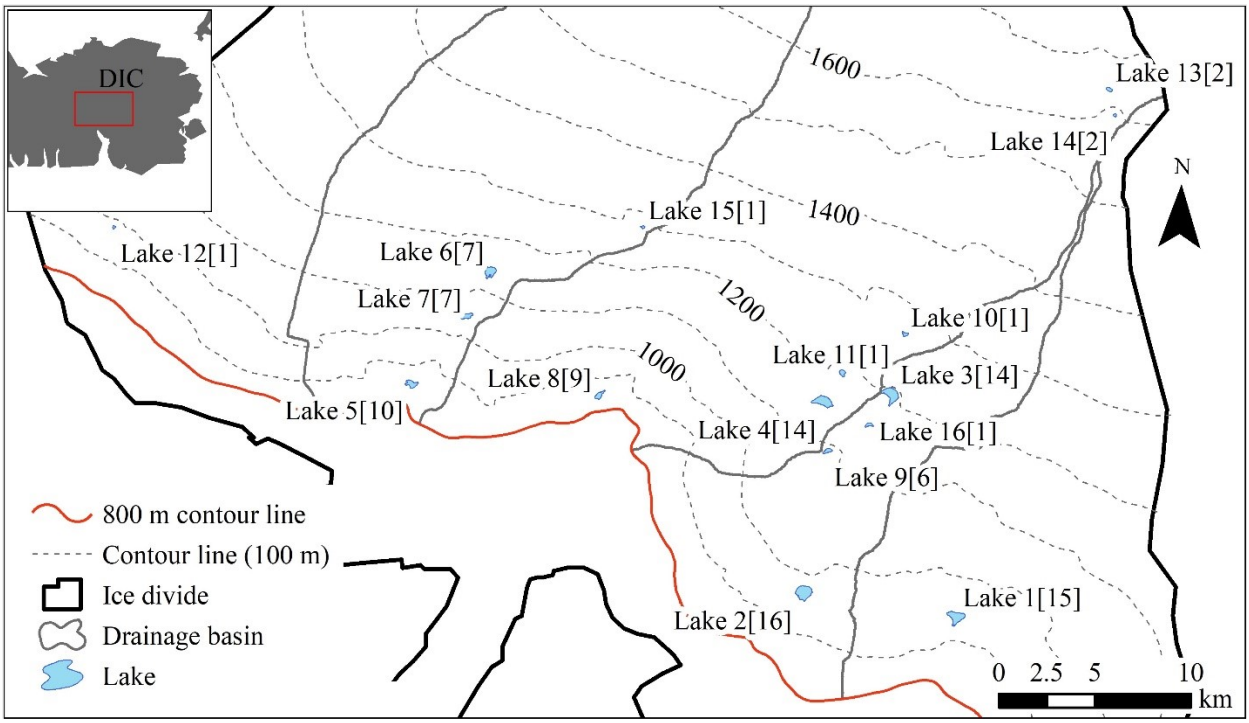

Figure 3.6. Distribution of supraglacial lakes and the number of years each lake was observed (value in brackets) during the period 2000–16

Table 3.2**.** Aggregate length (km) of supraglacial channels (SC) by glacier zone for each year when sufficient imagery was available. Note that for each year, the aggregate length of supraglacial channels by glacier zone was calculated according to the area of the glacier zones in that year (when information was available). Differences of <1m in the total length are due to rounding.

	2000	2001	2002	2005	2006	2007	2008	2009	2010	2011	2012	2013	2014	2015	2016	2017
SC length - BI & SI zone	23	33		14	14	33	40	36	39	30	51			52	94	
SC length -Wet snow zone	155	201		142	152	163	141	161	183	199	221			222	203	
SC length - Percolation zone						0	12	5	15	67				6	5	
SC total length - all mapped glacier zones	179	233	199	156	166	197	193	202	237	296	272	163	240	280	303	281

3.6.3 Supraglacial channels

The aggregate extents of the supraglacial drainage network in each year of the study period (for which sufficient imagery was available to allow drainage network mapping, see section **3.4.1**) are shown in Figure 3.7. The density of supraglacial channels is higher at lower elevations in the wet-snow zone. On average, there were 224.8 km of mapped supraglacial channels in each year. The largest aggregate length of supraglacial channels (303.3 km) was recorded in 2016, when the maximum elevation reached by a channel was ~1540 m a.s.l.. The shortest aggregate channel length (155.7 km) occurred in 2005, when channels were confined to areas below ~1210 m a.s.l. The highest elevation (1505 m a.s.l.) of a singular '*Regular'* supraglacial channel was observed in 2014, and the lowest (1197 m a.s.l.) in 2005 and 2011. Above the WSL, channels were mostly '*Irregular'*. '*Irregular'* channels (see section 3.4.1.1) were typically observed in the upper reaches of '*Regular'* channels although, at times, 'Irregular' channels also formed parallel to the continuous channels.

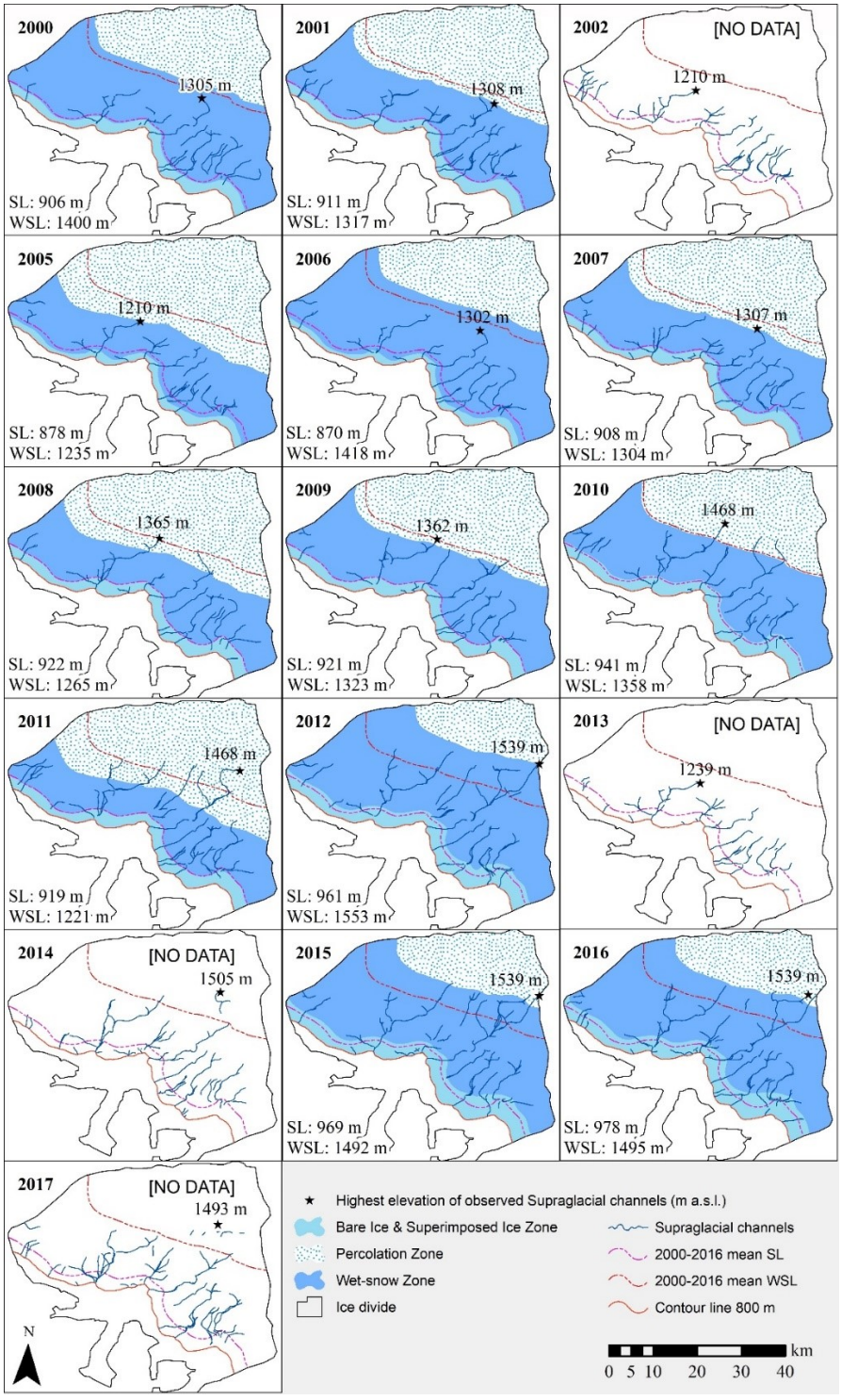

Figure 3.7**.** Distribution of glacier facies zones and the aggregate extent of the supraglacial drainage network in each year of the period 2000–16 for which sufficient imagery was available. The dashed pink and red lines show the position of the 17-yr average Snow Line (SL) and Wet Snow Line (WSL), respectively. For each year, the highest elevation at which channels were observed (black star) and the spatially-averaged elevations of the SL and WSL are included in each inset box. The 800 m contour line demarcates the lower boundary of the study area.

The total length of supraglacial channels mapped in Basin 1 (296 km) was less than half that in each of the other four drainage basins (average of Basins 2–5: 825 km). Supraglacial channels in Basin 1, which is characterized by stagnant ice (see section 3.3), are long (average length of 2.3 km per channel segment) with a large amount of spatial variability in the location of channels that are found below ~1200 m a.s.l.. In contrast, Basins 2–5, which drain into the North and South Croker Glaciers, have well-defined dendritic networks of supraglacial channels (below ~1200 m a.s.l. in Basins 4 and 5, and below ~1400 and ~1500 m a.s.l. in Basins 2 and 3 respectively). Channels in these basins occur in the same locations in multiple years, albeit with a small amount of spatial variability.

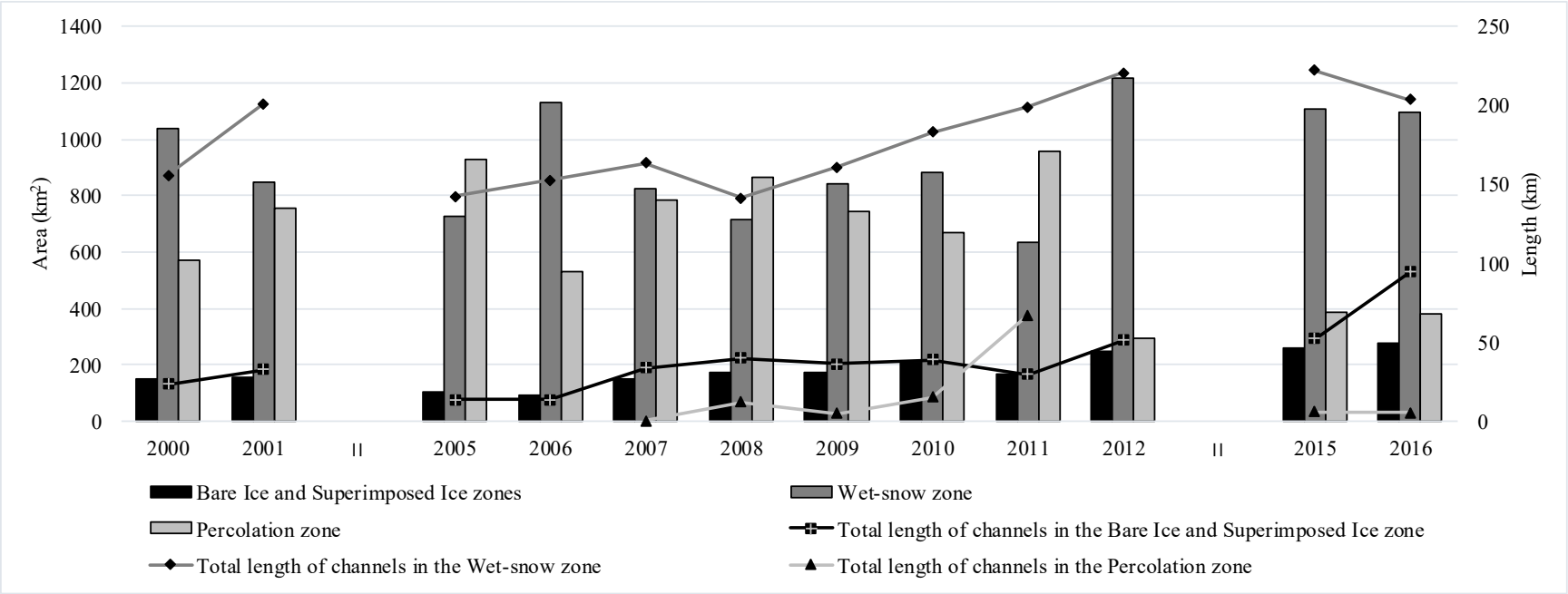

Figure 3.8. Area of mapped glacier facies zones (km^2) and aggregate length ('total length') of supraglacial channels (km) during the period 2000–16 for years when sufficient imagery was available.

3.6.3.1 Seasonal evolution of supraglacial channels

The number and lengths of individual supraglacial meltwater channels both increase over the course of July (section **3.4.1**, Appendix B - Chapter 3 - Table 3). The channel network typically attains its annual maximum extent at the end of July. In August, the number and total length of supraglacial channels progressively decrease before the channels eventually disappear. This is due to either a lack of surface meltwater production (the melt season ended before 13 August at Site-1, except in 2010 and 2016, Table 3.1) or to the infill and burial of the channels by new snowfall.

During a given melt season, the supraglacial drainage network in the wet snow zone is often diffuse, with small discontinuous tributary channels linking to the main trunk channels (Figure 3.4, orange polygons). These small channels are likely either to have been abandoned at the end of the summer due to a lack of meltwater production, or to have formed at the end of the melt season as a result of downglacier drainage of meltwater previously stored in lakes or firn at higher elevations (Rippin, Pomfret and King, 2015; Yang *et al.*, 2016).

3.6.3.2 Year to year variability in, and persistence of, supraglacial channels

The number of years in which a particular channel (‘*Regular’*) or channel segment (‘*Irregular’*) was observed in the available imagery is presented in Figure 3.4. Many ‘*Regular’* channels occurred in the same location in multiple years (Figure 3.4), suggesting that these channels are predisposed to reappear in the same location year after year. Supraglacial channels that formed in the same location in at least five years are usually found in the wet snow zone between ~850 and 1280 m a.s.l (section 3.6.1)**.**

Similar to the supraglacial lakes, the main streams of most '*Regular'* channels appeared in the same location in at least six of a possible 16 years, with some channels being observed in almost all years for which imagery was available. For example, a ~10 km long channel located on the eastern edge of Basin 4 between ~945 m a.s.l. and ~1155 m a.s.l. was observed in all years, albeit with some (~900 m) lateral variation in position. Finally, examination of the type, location, and persistence of channels (Figure 3.4) indicates that new channels begin as '*Irregular'* channels and evolve into '*Regular'* channels over time. This observation is important as the upper parts of most channels were classified as '*Irregular'* but, with continued warming and increased surface melting (Arctic air temperatures are expected to increase at twice the rate of global mean air temperatures, warming by 3.1ºC by 2100 (AMAP-SWIPA, 2017)), it is likely that these channels will evolve into '*Regular'* channels.

3.6.4 Comparison of supraglacial channel distribution, glacier facies zones and summer air temperature

Changes in the extent and distribution of glacier facies zones and supraglacial drainage networks are strongly tied to changes in summer air temperature (Lampkin and Vanderberg, 2014; Leeson *et al.*, 2015; de Jong, Copland and Burgess, 2018). Our results suggest a complex relationship between air temperatures, the distribution of glacier facies zones, and the development of supraglacial drainage networks, especially prior to 2012. It was not until 2015 and 2016 (no glacier facies zone data are available for 2013–14) that there was a coincident reduction in the area of the percolation zone and an increase in the total length of supraglacial channels that coincided with summers with relatively large

PDD sums. The 2015–16 average PDD sum at Site-2 was 49°C compared to 28°C in 2013–14.

Comparison of the lengths of supraglacial channels with available in situ air temperature data shows that the aggregate length of supraglacial channels in a given year varies with the annual sum of positive degree days (PDD), which serves as a proxy for the total available melt energy (Huybrechts and Oerlemans, 1990; Braithwaite, 1995). The PDD sum at Site-2 increased from 0.6°C in 2004 to 52°C in 2009 (the 2004–09 average PDD sum was 32.7°C), and this was followed by three consecutive years (2010–12) with PDD sums >60°C. In 2012 there were abrupt increases in channel length in all facies zones. Specifically, the total lengths of supraglacial channels in the bare ice/superimposed ice zone and the wet-snow zone increased by 64 % and 28 %, respectively, compared to the 2000–12 mean. In the percolation zone, the aggregate length of supraglacial channels in 2011 (67 km) was more than eight times the 2007–11 average (8 km; with no channels observed prior to 2007).

Comparison of the areas of each glacier facies zone with the PDD sums at Site-2 shows some agreement between the occurrence of larger summer PDD totals and the expansion of the bare ice/superimposed ice zones, albeit with some delay. Prior to 2012, there was often a delay of ~1–2 years between changes in PDD totals and changes in the extents of these facies zones. For example, at Site-2 in 2010, there were abrupt increases in melt season duration (75 days in 2010; average 2004–10: 40 days), and PDD sum (68°C in 2010; average 2004–10: 38°C). Yet, the areas of the bare ice and superimposed ice zones remained relatively stable (average 2000–11: 153 km^2) and it was not until 2012 that they increased to 245 km^2. No such relationship between PDD sums and facies zone areas was

observed for either the wet-snow or percolation zones prior to 2012. Instead, from 2000–11, the areas of these zones exhibited a large amount of inter-annual variability.

Prior to 2012 there was considerable inter-annual variability in the area of the wet snow zone, as indicated by the overlap between the maximum elevation of the snowline and the minimum elevation of the wet snowline. After 2012, however, there is clear separation between all three glacier zones (Figure 3.7, grey area) and the area changes of all mapped glacier zones align more closely with the changing PDD sums than they did from 2000–11. Importantly, beginning in 2012, there was a distinct change in the nature of the relationship between the areas of glacier zones, the lengths of supraglacial channels, and the PDD totals. Maximum PDD sums at Site-2 occurred in 2012, and there was an abrupt increase in the area of the wet-snow zone (1217 km² in 2012; 2000–11 average: 850 km²) at the expense of the percolation zone (295 km^2 in 2012; 2000–11 average: 755 km^2). Furthermore, from 2012 onward, there is clear separation between all three facies zones (Figure 3.7, grey area) and the areas of all mapped glacier zones co-vary more closely with the PDD sums than they did from 2000–11.

In 2015 and 2016 (no glacier facies zone area data are available for 2013 or 2014) a decrease in the area of the percolation zone and an increase in supraglacial channel lengths coincided with an increase in PDD sums at Site-2 (2013–14 average PDD sum: 28°C; 2015–16 average PDD sum: 49°C). Such a clear and direct correspondence between changes in air temperature, supraglacial channel extent, and the areas of the different glacier facies zones was not observed during the period from 2000 to 2011/12. Importantly, in 2015 and 2016, lower PDD sums at Site-2 (44°C and 54°C, respectively) generated supraglacial channel networks that were comparable to those observed from 2010–12 when

the PDD sums were markedly higher (between 60°C and 68°C at Site-2). This may indicate a change in near-surface stratigraphy that would be consistent with the presence of more extensive and impermeable ice layers in the near surface part of the firn. Although an abrupt increase in the area of the wet-snow zone (at the expense of the percolation zone) compared to the previous year was also observed in 2006, it was not accompanied by noticeable changes in the observed supraglacial drainage network. Instead, our results suggest that the three consecutive warm years 2010-2012, may have driven the observed change in the nature of the relationship between near-surface air temperatures, the distribution of glacier facies zones, and the development of supraglacial drainage channels.

Our results suggest that a sustained period (e.g. 2010–12) of anomalously high summer air temperatures (Mortimer, Sharp, and Wouters, 2016) and associated high melt rates (Gardner and others, 2011; 2013; Sharp and others, 2011) altered the hydrology of the Croker Ice Divide region on the Devon Ice Cap. Initially, surface meltwater was able to percolate downward into the firn, where it refroze as infiltration ice and released latent heat (Cogley *et al.*, 2011). Increased melt and refreezing within the firn during the study period resulted in the development of impermeable layers in the sub-surface (Bezeau and others, 2013; Gascon and others, 2013a). This modification to the firn structure, which reduced the firn's infiltration and water storage capacities, was not immediately expressed at the surface (e.g. by the development of extensive supraglacial channels). Over time, however, successive high melt years resulted in the formation of thick and spatially-extensive ice layers within the firn that impeded the vertical percolation of meltwater into the firn below these ice layers. Thereafter, meltwater was retained in the surface and near-surface layers of the firn (Bezeau *et al.*, 2013). In the percolation zone, this ponded

meltwater forms slush areas (Fountain, 1996) and supraglacial lakes (e.g. Chu, 2014), or can be routed downslope as slush flows or via supraglacial channels. Importantly, these surface features are often the first visible indications of the changes that have occurred in the subsurface.

3.6.5 Modeled supraglacial drainage network

To examine how the observed supraglacial drainage network is influenced by variations in surface slope and by the distribution of impermeable ice layers within the firn, a modeled supraglacial drainage network was generated (section **3.4.2.1**). This consisted of 943.3 km of modeled supraglacial channels that extended up to ~1790 m a.s.l.. This is much longer than the mapped supraglacial channel network (which contained an average of 224.8 km of mapped channels per year, and extended to a maximum elevation of 1539 m a.s.l. in 2012 and 2015). This is to be expected because the modeled channel network assumes an impermeable underlying surface, whereas the mapped drainage network reflects the combined influences of surface topography, spatial variations in surface and near-surface permeability, and the distribution of moulins and crevasses. Basin 3 had the greatest total length of modeled channels (336.9 km), followed by Basins 2 and 5 (203.9 and 197.7 km respectively), while Basin 4 had the smallest total length of modeled channels (61.2 km).

3.6.5.1 *Comparison of the mapped and modeled supraglacial drainage networks*

The aggregate length of supraglacial channels observed from 2000–17 that overlaps with the modeled supraglacial channels is 2777.2 km, which represents 77% of the mapped channels. The highest elevation at which the distributions of mapped and modeled channels

overlapped was 1538 m a.s.l. (in Basin 3 in 2016). In this basin, 91% (872.1 km) of the mapped channels overlapped with the buffered modeled channels during the period 2000–17, compared with 88% (659.6 km) in Basin 2 and 79% in Basin 5 (567.3 km). For the study area as a whole, the largest percent overlap occurred in 2015 when 81% of the 280.4 km of mapped channels overlapped with the buffered modeled channels. This is notable as it is the same year in which lakes first appeared in the percolation zone. It also post-dates the 2012 shift in the relationship between near-surface air temperatures and the distributions of glacier facies zones and supraglacial channels. In contrast, 2013 had the least overlap between modeled and mapped supraglacial channels (71%; 116 km of the 162.6 km of mapped channels). The total length of channels mapped in that year was also small. 2013 was an anomalously cold year on the DIC relative to 2000–15 (Mortimer, Sharp and Wouters, 2016) and GRACE-derived glacier mass change estimates for that year in the QEI were only mildly negative (Blunden, Arndt and Hartfield, 2018). Thus, a small number of supraglacial channels is expected.

3.7 Discussion

Two elements are required for a supraglacial drainage network to develop: surface meltwater and an impermeable surface and/or near-subsurface to sustain continuous horizontal (as opposed to vertical) meltwater flow at the ice cap surface. The observed expansion of the supraglacial drainage network in the Croker Ice Divide region is a result of the combined effects of increases in surface melt rate, meltwater percolation into snow and firn, and growth of ice layers within the firn (Wolken and others, 2009; Gardner and others, 2011; 2013; Sharp and others, 2011; Fisher and others, 2012; Wyatt, 2013; Bezeau and others, 2013; Gascon and others, 2013a; 2013b). Ice layers and other ice slabs in the

near-subsurface of the firn can impact the local and regional hydrology (Chen and others, 2017) by promoting surface (or shallow sub-surface) runoff from firn-covered areas (Mikkelsen *et al.*, 2016). Continued refreezing of meltwater above an initial ice lens (which forms infiltration ice) can result in progressively thicker and more widespread ice layers within the firn.

According to the long-established model of glacier facies zonation (section 3.2.1), melt can occur in all the glacier facies zones that are present on the DIC, with small scale refreezing occurring first in the percolation zone (accumulation area), and runoff occurring initially only in the ablation area. Our results show that supraglacial drainage networks can develop in firn-covered areas, including the percolation zone. Because there is usually insufficient melt in this zone to fully saturate the firn layer (Benson, 1962; Cogley *et al.*, 2011), the development of supraglacial channels in the percolation zone points to the presence of impermeable ice layers in the firn that, at least locally, prevent the downward percolation of meltwater (Bezeau and others, 2013; Gascon and others, 2013a; Chen and others, 2017) and promote surface runoff.

Supraglacial channels were first observed in the percolation zone of Devon Ice Cap in 2007, when the total length of channels was only 300 m, and lakes were first observed there in 2015. By summer 2011, the total length of channels in the percolation zone was 67 km (values respect the year-to-year changes in the locations of the boundaries between glacier facies zones). After 2012, however, the total length of supraglacial channels in the percolation zone was much lower, in part because the lower limit of this zone had shifted to higher elevations because of expansion of the wet snow zone.

The expansion of the supraglacial drainage network to higher elevations occurred after three anomalously warm summers (2010–12; Table 3.1) (Mortimer, Sharp and Wouters, 2016). The formation of lakes and the increase in supraglacial channel length in the percolation zone coincide with the upward expansion of a >1 m thick ice layer in the firn (from ~1300 m a.s.l. in 2004 to ~1550 m a.s.l. in 2012 (Bezeau *et al.*, 2013), and is consistent with the presence of undulating ice layers in the top six meters of the subsurface of the DIC between 1150 and 1895 m a.s.l.in 2015 (Rutishauser *et al.*, 2016). The presence of such ice layers in the firn, particularly near the surface, may help to explain the occurrence of supraglacial channels in this region in 2015 and 2016 even though the PDD sums in those years were small (compared to earlier in the study period).

3.7.1 Attributes of the mapped and modeled supraglacial drainage networks

Surface topography and the presence of impermeable ice layers in the firn are the key elements that control the development of supraglacial drainage networks in the accumulation zone. Investigation of the influence of surface topography on the observed supraglacial drainage network was undertaken via a comparison of the distribution of modeled and mapped supraglacial channels (section **3.5**). This suggests that, in general, the locations of most observed channels were controlled by the surface topography, particularly at higher elevations in the percolation zone where ice layers are widespread within the firn. Coincidence between the locations of the buffered-modeled channels and the mapped channels ranged from 71% (2013) to 81% (2015), with an average (2000-2017) agreement of 77%. Agreement was better at higher elevations, suggesting that the locations of supraglacial drainage channels at these higher elevations are influenced primarily by the surface topography. At higher elevations, supraglacial channels tend to form in the same

locations in multiple years. These locations are determined by the surface topography and by the presence of a continuous ice layer within the firn that is thick enough to impede vertical percolation of meltwater. At lower elevations, as meltwater flow increases, erosion due to heat production takes place, causing a lateral migration of channels (Karlstrom, Gajjar and Manga, 2013). Thus, the relatively low overlap between modeled and mapped supraglacial channels found at lower elevations on Devon Ice Cap in most years is expected, as is a poorer coincidence between the locations of mapped and modeled channels.

Examination of how the level of agreement between the mapped and modeled supraglacial channels varies as a function of elevation (100 m elevation bands) shows better agreement at higher elevations. In each year, the best agreement (91–100%) occurred in either the highest or second-highest elevation band in which channels were mapped, while the poorest agreement (60% overlap) was found below 1100 m a.s.l. in all years except 2014, when it was in the highest elevation band (26% overlap at 1400–1500 m a.s.l.). The near complete agreement (>90%) between mapped and modeled channels at high elevations suggests that surface topography is a major control on the location of channels in the percolation and wet snow zones.

3.8 Conclusions

In this study, Landsat7/8 imagery was used to characterize and digitize the supraglacial drainage network in the Croker ice divide region of the Devon Ice Cap during the period 2000-2017, and to compare it with a hypothetical surface drainage network that was derived from a digital elevation model of the glacier surface. Records of air temperature (at 2 m) were used to analyze spatial and temporal variations in the distribution

of glacier facies zones and in the extent and degree of development of supraglacial drainage networks.

The area of the percolation zone decreased substantially over the study period, while that of the wet snow zone increased, as did near-surface air temperatures. Supraglacial channels first appeared in the percolation zone in 2007. Over time, these channels extended upwards to higher elevations. The total PDD sum required to generate equivalent supraglacial drainage networks was substantially less in the latter part of the study period (2015 and 2016), which may indicate a reduction in the infiltration capacity of the firn due to ice layer buildup within it. This is consistent with the findings of previous studies that indicate that, on Arctic Ice Caps, the capacity of the firn layer to retain meltwater is likely decreasing due to increases in the rate and spatial extent of surface melting that are driving more widespread formation of thick ice layers in the shallow subsurface of the firn (Van Angelen and others, 2013; Bezeau and others, 2013; Gascon and others, 2013a; Machguth and others, 2016; Mikkelsen and others, 2016). Monitoring the expansion of supraglacial drainage networks to higher elevations using remotely-sensed imagery permits the identification of areas where high rates of firn densification, and especially the formation of extensive and impermeable ice layers in the firn, may be promoting the development of new supraglacial channels and lakes in areas of ice caps and glaciers that have not traditionally supported extensive supraglacial drainage networks. The development of such drainage networks in the percolation zone may provide an early indication of an impending change in glacier facies zonation (e.g. a change from a percolation zone to a wet-snow zone). As a result, remote sensing studies of supraglacial drainage system change (such as this) can help with site selection for field-based studies of

meltwater drainage processes in areas in which thick ice layers are likely to have developed.

Chapter 4 - DETECTING ICE LAYERS IN THE PERCOLATION ZONE OF THE DEVON ICE CAP USING TERRASAR-X IMAGES

4.1 Introduction

Glaciers and ice caps in the Canadian Arctic Archipelago are projected to be the largest contributors to future sea level rise after the Antarctic and Greenland Ice Sheets (Radić and Hock, 2011; Radić *et al.*, 2013). Increased mass losses from the Canadian Arctic are associated with recent warm summers that have resulted in higher rates of surface melting (Gardner *et al.*, 2011; Lenaerts *et al.*, 2013). The accumulation areas of ice sheets and ice caps, underlain by porous snow and firn, can absorb and store meltwater formed on the surface during the melting season in the pore space available within the subsurface. This limits the amount and rate at which meltwater runs off from the glacier (Harper *et al.*, 2012). The stored meltwater may freeze in the pore volume of the firn, forming ice lenses and ice layers that limit further percolation of surface meltwater (Bezeau *et al.*, 2013; Gascon *et al.*, 2013, 2014; Machguth *et al.*, 2016). This can lead to lateral and downslope diversion of subsurface water flow or to further accretion of ice formed by freezing of meltwater ponded on top of the infiltration ice, which leads to the formation of thick ice layers, the extent and thickness of which depend on the surface elevation and topography.

The near surface firn stratigraphy of the Devon Ice Cap (DIC) has changed a lot in recent years and this has resulted in major changes in surface meltwater drainage patterns. The most dramatic changes are associated with the development of thick and widespread ice layers in the shallow subsurface layers of the firn (Bezeau *et al.*, 2013; Gascon *et al.*, 2013; Rutishauser *et al.*, 2016). Once a continuous ice layer is formed, any further vertical percolation of meltwater is hindered and lateral flow will occur in downward sloping areas,

along with ponding in surface depressions. However, the influence of meltwater refreezing in the accumulation area and its role in enhancing runoff from firn-covered regions remains unquantified. A recent study performed on the Greenland Ice Sheet has suggested that the enhancement of runoff that results from the presence of ice slabs (thick and discontinuous ice layers) buried in firn can add up to 74 millimeters to the predictions of future sea level rise related to melting on that ice sheet (MacFerrin et al., 2019). Accretion of infiltration ice on top of an existing ice layer can intensify the amount and rate at which meltwater runs off from the system. When ice accretion by refreezing of meltwater is continuous, the ice layer can spread into its immediate surroundings, forming further, or more extensive, impermeable ice layers.

Documenting the presence, distribution, and thickness of continuous and discontinuous ice layers on DIC was the motivation of past field campaigns that documented recent changes in firn stratigraphy (Bezeau *et al.*, 2013; Gascon *et al.*, 2013; Rutishauser *et al.*, 2016). Although these studies have looked into changes in firn densification using data from Ground Penetrating Radar (GPR) surveys and firn cores, these data are temporally discontinuous and at most provide an accurate assessment of the changes that occurred between specific time periods. To fully understand the changes that are occurring in the sub-surface (i.e. within the firn layer) of the accumulation zone, it is critical to keep collecting data over the same region in order to document the extent and nature of ongoing changes, as well as to understand the timing, causes, consequences, and spatial pattern of the build-up of ice layers within the firn.

The use of satellite remote sensing data is the most inexpensive and effective method of observing changes over large areas of the planet. However, until recently, large scale observations of the subsurface stratigraphy of ice caps have required expensive airborne radar surveys. Here we use an experimental approach that compares interpretations of GPR data

collected in situ, with interpretations derived from Kennaugh-decomposed radar imagery from the TerraSAR-X (TSX) satellite (Chapter 2). The combined analysis of the two datasets provides information about the benefits and limitations of the TSX satellite data in regards to radar penetration depth and the potential value of the resulting data for interpretation of the properties of the shallow sub-surface layers of the firn layer of the ice cap. Data from ground-based PulseEKKO Noggin radar collected in the spring of 2017 along the CryoSat line (Figure 4.1, Box A) are used to document the stratigraphic changes in the firn layer of the DIC that have taken place since the 2012 GPR survey (Gascon *et al.*, 2013). With this dataset, we are able to track the development of ice layers within the firn layer and document their spread to higher elevations on the ice cap. Additionally, a gridded GPR dataset was collected over a small area of the percolation zone to investigate the development of 2 ponds that formed in 2015 and 2016 and that were identified as an abnormal formation detectable in TerraSAR-X data (Chapter 2 – Item 2.5.1.). Three firn cores were collected to check the accuracy of the GPR interpretations and to aid in the interpretation of the stratigraphic anomaly detected by TSX. This unique combination of datasets allows us to understand the complex dynamics of the formation and expansion of ice layers within the firn, as well as their impact on the expansion of the supraglacial meltwater drainage network (See Chapter 3 – Section 3.6.3.).

4.2 Study Site

The Devon Ice Cap is located on Devon Island, Nunavut, Canada. The region has been studied extensively for more than 60 years (Boon *et al.*, 2010). Current research includes airborne radio-echo sounding and ground data acquisitions to characterize an inferred system of hypersaline subglacial lakes beneath the ice cap (Rutishauser *et al.*, 2018). The ice cap is characterized by a dome shape with a maximum elevation of 1920 m a.s.l. Two main ice

divides extending from this point separate the ice cap into four regions. The southern flank of the ice cap, the focus of this research, includes the North and South Croker Glaciers that flow into Croker Bay.

In order to examine changes in the firn stratigraphy and document the spread of ice layers across the study region, GPR data were collected along a 38 km extension of the CryoSat line starting from a point located in between the North and South Croker Glaciers (970 m a.s.l) and ending at the Automatic Weather Station Site-1 (near the summit of the ice cap at ~1800 m.a.s.l.) (Figure 4.1 Box A). GPR transects were also collected over a small area of approximately 9.87 km^2 (Figure 4.1 – Boxes B and C) as part of an effort to investigate the potential of X-band SAR and, more specifically, of the Kennaugh Elements Decomposition technique, for early detection of the formation of extensive ice layers in the shallow subsurface of the ice cap. The study area includes 2 small lakes detected using Landsat-8 images (Chapter 3 – Item 3.6.2) that are co-located with anomalies in the TSX data from 2015-2017 (Chapter 2 – Item 2.5.1).

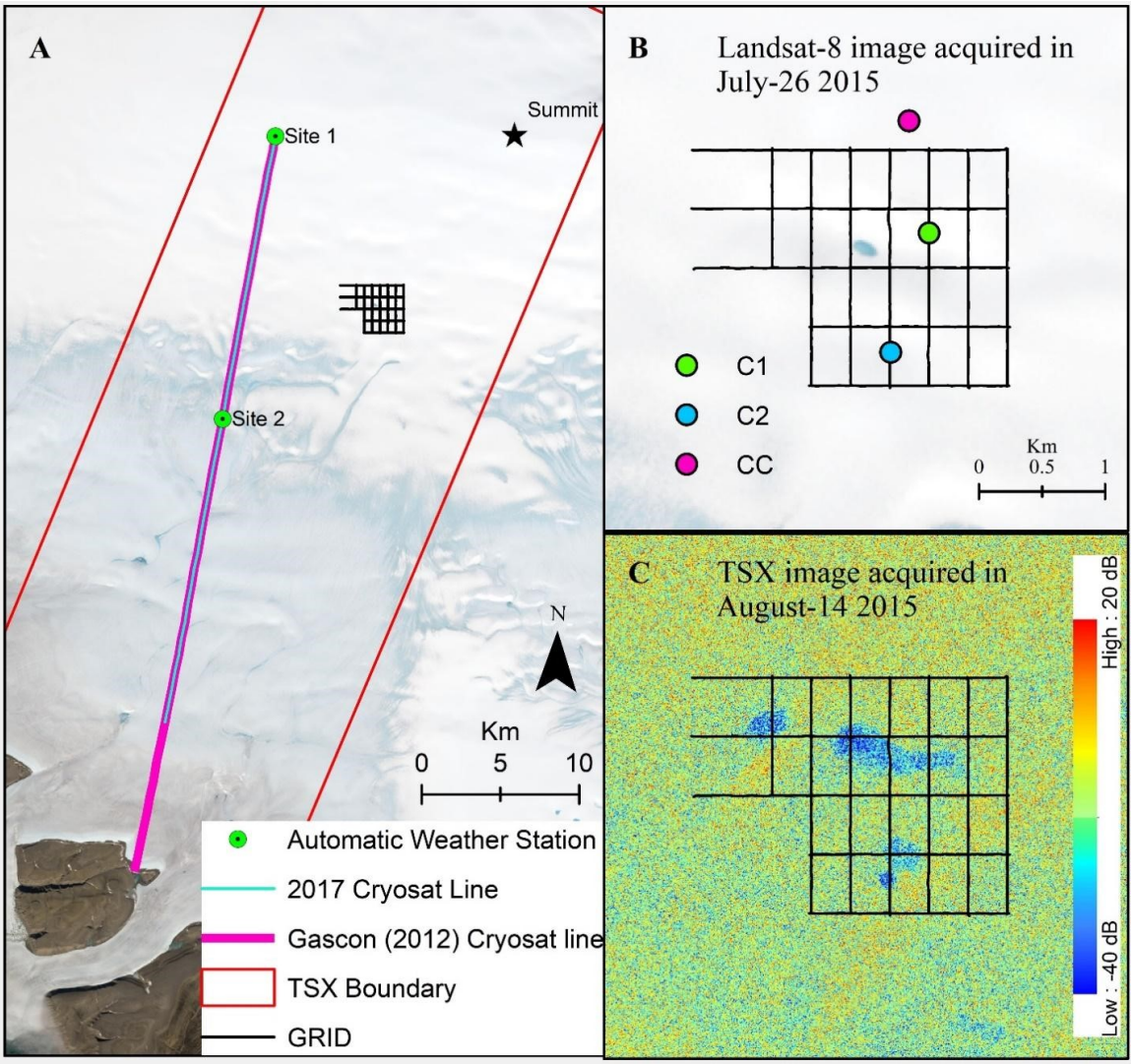

Figure 4.1 - Box A shows (in pink) the location of the CryoSat line acquired by Gascon et. al. (2012) and (in cyan) the section surveyed in in 2017, along with location of the grid within the TSX image limits. Box B presents a Landsat-8 image acquired on July-26 2015, showing the distribution of melt on the surface and the location of the 3 firn cores. Box C shows the K3 Element from the TSX image acquired on August-14 2015. High values indicate a double bounce contribution and lower values indicate the surface contribution.

4.3 Data and Methods

4.3.1 GPR data and processing

GPR data were collected on the southern flank of the ice cap, along a 33.5 km grid and a 38 km long section of the CryoSat Line in spring 2017 using a 500 MHz PulseEKKO Noggin radar (Sensors & Software Inc.) with a center frequency of 60 MHz. Traces were recorded

every second, which allows collection of information on the structure of the firn to a depth of at least 10 m below the snow surface.

GPR positioning was obtained with a Leica Geosystems GPS system using concurrent differential kinematic GPS measurements, providing up to 25 cm RMS accuracy. The GPS antennae were mounted on a Komatiq sled towed by a snowmobile and the GPR antennae were mounted on a smaller wooden structure attached to the back of the Komatiq. Two hand-held GPS units were coupled to the Komatiq and to the snowmobile to provide backup GPS information in case of disconnection of the cables to the GPS antennae and the GPR equipment that would have resulted in total loss of geolocation information (a common issue due to the effect of low air temperatures on the stiffness of the wires and connection cables).

GPR data were processed using the Ekko-Project software from Sensors and Software. Snow and firn have different dielectric properties and, as such, the transmitted radar signal reflects from different Internal Reflecting Horizons (IRHs). The differences in density of ice (830-917 kg/m^3), firn (400-830 kg/m^3), and fresh snow (50-200 kg/m^3) (Cuffey and Paterson, 2010)), where ice has a higher density than firn, produce well defined boundaries in GPR depth profiles that make it possible to distinguish complex patterns of melting and refreezing within the firn.

The pre-processing follows the steps used by Gascon et al. (2013) and uses a similar color scheme to display the data, thus facilitating the comparison between profiles without compromising the interpretation of the data. A few steps are required to ensure that the dataset is up to the highest standards. First, all transects were checked for the time-zero point. The time-zero point is associated with the scale and depth penetration of the GPR recordings and must occur at the first large deflection in the signal to ensure the accuracy of all transects

(EKKO Manual). GPS data recorded simultaneously with the GPR instrument and also independently by hand-held GPS were used for correction of the surface topography. All static measurements recorded when the equipment was not moving were removed from all transects. Due to failure in the GPS equipment coupled to the GPR, some transects had to be manually adjusted for the initial location of the transect. Such editing was conducted using the GPS information collected as backup by a handheld GPS coupled to the komatik sled along all GPR transects and adjusted to 1.2 m, which was the approximate distance between the GPR and GPS (in the komatik) equipment in the field.

The GPR processing was designed to ensure that the firn stratigraphy and, in particular, the boundary between glacier ice and the firn layer is noticeable. Although the same equipment was used for this research and that performed by Gascon et al. (2013), the processing steps were adapted in order to obtain a better result in response to the different velocities at which the GPR was hauled in the two surveys. Background subtraction using a rectangular filter with 1 meter width was applied to the dataset in order to enhance dipping events and suppress horizontal responses recorded by the receiver (EKKO Manual). To correct all low frequency content in the recorded data, the Dewow filter was applied using a window width of 1.5 pulses (half of the pulse width recorded). The last step in the processing flow included the velocity adjustment. This step is crucial to the interpretation of the data as it is used to estimate the target depth (EKKO Manual). The speed at which the GPR signal travels was adjusted to 0.206 m/ns using the theoretical relationship provided by (Kovacs, Gow and Morey, 1995), which accounts for the average velocity calculated from measured densities of firn and ice.

4.3.1.1 CryoSat Line

The CryoSat Line extends from 970 m a.s.l. to 1800 m.a.s.l. intersecting all the glacier facies zones on the ice cap: glacier ice, superimposed ice, wet snow, and the percolation zone (information about the zonation on the DIC is presented in Chapter 3 – Items 3.2.1 and 3.6.1). Since 2004, several GPR campaigns have been conducted along the CryoSat line in order to calibrate and validate the radar altimeter on board the Cyosat-2 satellite. From 2007 to 2012, the CryoSat line was revisited at least once a year mostly to validate the accuracy of elevation changes (Colgan, 2008). The 38 km long GPR transect that partially covers the CryoSat line was collected over 2 different days (12 and 17 May 2017). The Cryosat line is overlaid on, and compared to, the location of GPR data previously collected and documented by Gascon et al. (2013) (48 km in extent). The result of this analysis will provide more information about the progression of ice layer formation to higher elevations on the ice cap that is suggested in Chapter 3.

4.3.1.2 Grid Lines

The location and spacing of the grid lines to be surveyed were chosen especially to allow the characterization and interpretation of the ice build-up anomaly detected via TSX decomposition in 2015-2017 (Chapter 2 – Item 2.5.1) and to accommodate the drilling of firn cores in such way that they coincided with the grid transects. In total, the grid contained 12 radar transects (Figure 4.1 box A-C) that were collected in either a North-South direction (Vertical transect) or a West-East direction (horizontal transects). The GPR transects included 7 vertical and 5 horizontal profiles, and revealed the stratigraphy of the uppermost 8 meters of the firn. In order to organize data and make transect reading easy, the lines were named using the letter V (for N-S transects) or H (for W-E transects) followed by a sequential number

according to their position on the map. The westernmost vertical transect was named V1 and the easternmost was named V7. The horizontal transects were named from the northernmost to southernmost and range from H1 to H5. The grid is located on a descending slope of the DIC and ranges in elevation from ~1680 m a.s.l to ~1590 m a.s.l. It encompasses an area of ~8 km^2. Located in the wet-snow zone where the snowpack temperature reaches the melting point during the melt season, it was expected to show heterogeneous features such as refreezing within the firn and discontinuous ice layers (thickness: 0.5-1.15 m (Gascon *et al.*, 2013)). GPS data collected during measurement of the GPR transects are used to model the surface topography. Grid lines contain detailed information about the local characteristics of the firn stratigraphy and are interpreted jointly with the ice build-up anomaly.

4.3.2 Shallow firn cores

The accuracy of the firn stratigraphy and the identification of ice layers in the GPR data can only be confirmed via *in situ* validation of the processed results. Thus, the firn stratigraphy was derived from 3 firn cores (C1: 5.8 m; C2: 6.07 m; CC: 5.70 m - Figure 4.2) collected in the grid area. Two of these (C1 and C2) that are located along vertical profiles V5 and V4 respectively were used for validation and interpretation of the GPR data. The specific locations of the boreholes were chosen based on the location of the ice-build up anomaly detected in the KE data (Chapter 2 – Item 2.5.1). One additional firn core was drilled at a location north of, and slightly outside, the grid area (firn core CC). This core was used exclusively for validation against the KE. Originally, the goal was to collect 5 cores along the grid lines, but only 3 were actually collected due to the impact of adverse weather conditions on the field schedule.

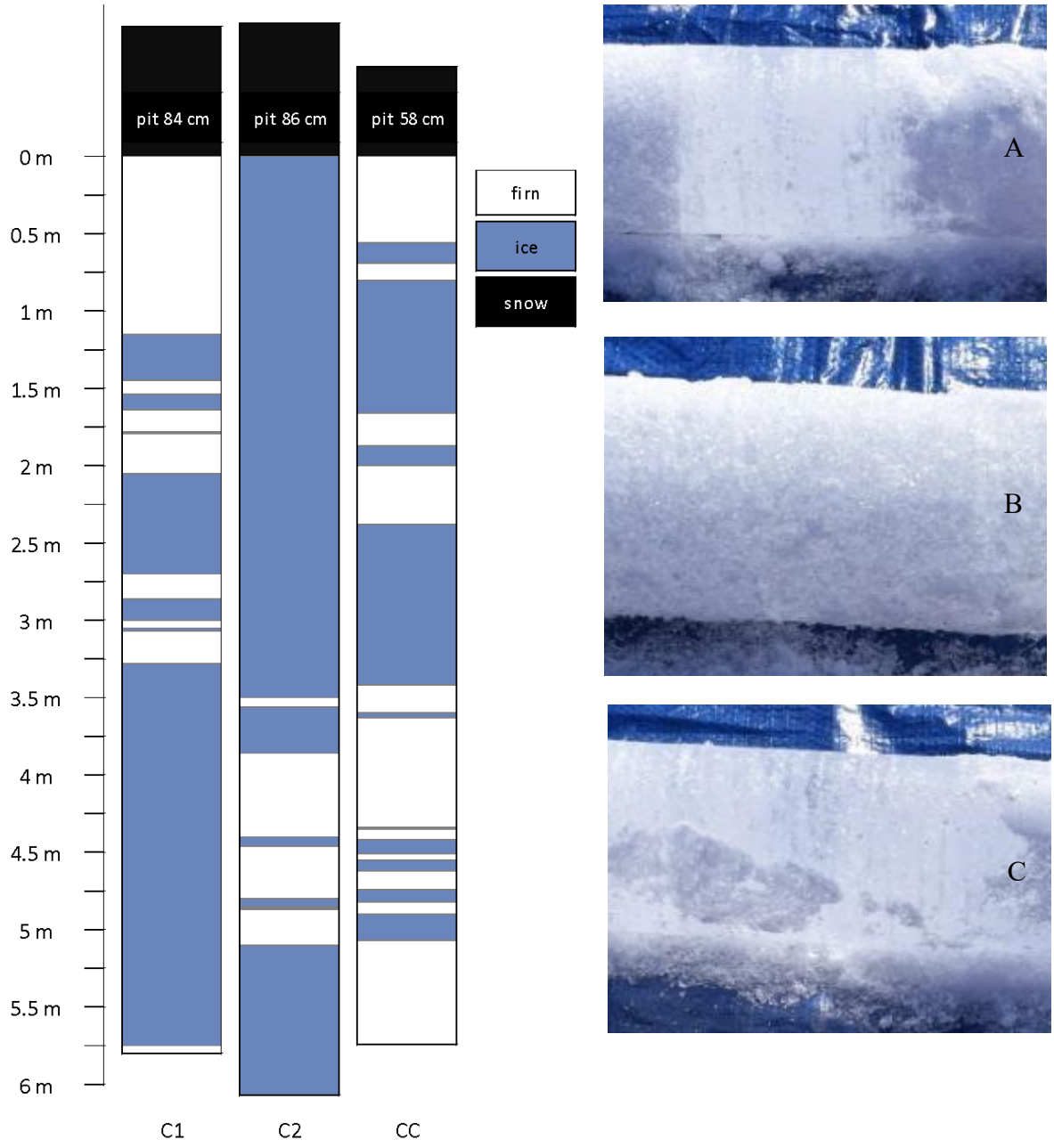

Figure 4.2 - On the left side the detailed stratigraphy of the firn cores. On the right side, box A shows a picture of a section of a firn core with the transition between firn and ice. Box B shows a section of the firn core composed of firn only. Box C shows a section of a firn core composed of ice.

Firn Core-1 (C1) was collected at 1.07 km from point 0 on the V5 profile in a downhill sloping location. The upper 1.15 m of the core profile is composed of firn followed by 3 layers of ice that decrease in thickness from 30 cm to 9 cm comprising the first 2 meters of the core. Firn Core-2 (C2) was collected at 2.57 km from the point on the V4 profile located in the lower

concavity of that profile. The first 3.5 m of the core was composed of ice with a total of only 4 sections (varying in thickness from 6 cm to 54 cm) composed of residual firn forming 5.1 m of the core. Both firn core stratigraphy profiles correspond with the GPR stratigraphy for their locations. The upper 0.5 m of firn core-C (CC) consists of firn followed by a thin (13 cm) layer of ice, 11 cm of firn, and 86 cm of ice forming the first 1.6 m of the firn core. (Appendix C – Chapter 4 - Figure 1).

4.3.3 Kennaugh Elements

The Kennaugh Elements (KE) are a product of a matrix decomposition technique that allows the partitioning of dual co-polarized TerraSAR-X (HH-VV) images into four distinct elements (Chapter 2 – Item 2.4.2). The element K_0 represents the total intensity of backscattering; K_3 contains the scattering difference between the even bounce and the odd bounce, which indicates whether the backscattering has a higher contribution from internal interaction with the target or from the surface of the target; K_4 reflects the difference between horizontally and vertically oriented dipoles, and K_7 represents the phase difference between the even and odd bounces.

The two Elements that yield the most important information are K_0, which summarizes the total intensity of backscattering, and K_3, which represents the real part of the inter-channel phase shift and contains the difference between even (also known as double) and odd (also known as single/surface) bounce scattering. Kennaugh decomposition of dual co-polarized radar satellite imagery acquired by the TerraSAR-X instrument during the period 2015-2017 is used to observe and investigate the depth to, and accuracy with, which X-band SAR data can be used to infer the shallow-subsurface stratigraphy. The grid lines are intersected with the KE images of 14-August 2015 when an anomaly was detected in the Percolation zone at its

maximum extent. This analysis will contribute to a better understanding of the potential of X-band radar data for retrieving stratigraphic information from firn.

4.4 Results and discussion

Snow and firn show different structures in the GPR profile. These are tied to the different processes that lead to their formation. Using a combination of pre-processing and processing flows, the GPR dataset yielded well-defined boundaries between ice layers and firn layers. Low amplitude reflections were dismissed and moderate/high amplitude reflections were amplified. The color scheme used shows ice layers in white color and firn in lilac shades. The interpretation of the transects can provide detailed information about the local characteristics of the firn stratigraphy and how it was formed. All definitions of the different stratigraphic profiles follow (Gascon *et al.*, 2013) and (Cogley *et al.*, 2011).

In the percolation zone, the ice core stratigraphy is expected to be highly heterogeneous with the local presence of ice pipes, ice lenses, and discontinuous ice layers. Such features create several internal radar reflectors that are recorded by the GPR. Thus, due to the small-scale variability of ice pipes and ice lenses within this region, the profiles show very small variability in the IRH. The wet-snow zone, where melting occurs during the summer, is characterized by the presence of heterogeneous ice layers that form within the firn as the meltwater refreezes. In this zone it is common to find residual firn within ice layers as a result of snow precipitation during the winter. Ice layers in this zone can be as thick as 1.5 m. and show up on the radar profile as having low radar reflectivity while the residual firn has high radar reflectivity. The superimposed ice zone has a low reflectivity due to the presence of a thick ice layer that is usually embedded with layers of residual firn. The bare ice zone, from which all the previous year's winter snow pack has melted by the end of the summer, is

characterized by continuous low radar reflectivity due to the homogeneity of the glacier ice, although some faint internal layers can be found.

4.4.1 CryoSat Line analysis and comparison with KE

To investigate the differences between the GPR profiles acquired in 2017 and that acquired in 2012 by Gascon et al. (2013) we take the distance from point zero which is the northernmost location for both transects and coincides with the location of the AWS Site-1. Data collected over the same region and 5 years apart (2012 and 2017) are used to track the migration of glacier facies zone boundaries since 2012 (Figure 4.1). In 2012 the percolation zone extended from Site-1 to 9.6 km down the CryoSat line and was characterized by a gradual compaction of the snow with the first indication of a thick ice layers occurring at 4 m depth. In 2017 a continuous thick ice layer was observed only 1.7 km downslope from Site-1 at ± 2.5 m depth and its thickness continued to increase down-glacier from there (Figure 4.3). The presence of a single and thick ice layer in this region indicates that an extensive melt event occurred over almost the entire ice cap between 2012 and 2017 except at locations above 1784 m a.s.l. Such findings indicate that the area of the percolation zone decreased substantially from 2012 to 2017. The first field campaign in 2012 detected only small variability in the IRH, which is tied to the absence of substantial melt and, as a consequence, gradual compaction of the snow package. In the following years a considerable amount of surface melt occurred over the ice cap leading to the development of thick and continuous ice layers within 3 m of the ice cap surface. Such a development requires an expansion of the wet-snow zone into higher elevation regions of the ice cap, consuming 7.9 km of the CryoSat line that were previously characterized as being located in the percolation zone.

The most significant changes in the locations of firn facies boundaries involved the wet-snow zone. In this zone melt occurs every year and percolation of meltwater into the underlying firn is followed by refreezing that creates discontinuous and thin ice layers at higher elevations and thick and continuous ice layers at lower elevations. Ice layers are generally identified by low radar reflectivity. In 2012, the wet-snow zone was spread across a total of 6.4 km of the CryoSat line, between kilometers 9.6 and 16 and contained ice layers with an undulating pattern. In 2017, the wet-snow zone reached higher elevations and its upper limit reached kilometer 1.7, while its lower limit was around kilometer 11.8, so the wet snow zone was around 10.1 km wide. The undulating layer pattern observed in the wet-snow zone has remained almost intact in the lower regions of the ice layer but has almost disappeared from its upper regions, likely due to the filling of pore volume with ice formed by the refreezing of meltwater percolating down from the ice cap surface coupled with a higher rate of snow compaction. Accretion of meltwater on top of the ice layer from 2012 to 2017 has significantly changed the area between the ice cap surface and the upper surface of the ice layer that, in 5 years, changed from very undulating between kilometers 9 and 16 to a smoother undulation in 2017 along with the presence of a thinner layer of firn on top of the ice layer as a result of freezing of meltwater on top of the ice layer that is thick enough to hinder access to the patches of firn buried beneath the ice. This finding is supported by the evidence that the thickness and form of the underside of the thick ice layer between kilometers 9 and 16 have remained almost unchanged although the upper surface has become more smoothly undulating as additional ice has accreted on top of the ice layer detected in 2012.

Significant changes occurred in the overall extent of the superimposed ice zone which has expanded its upper and lower limits at the expense of the wet snow and glacier ice zones

respectively. In 2017 this zone was 20.2 km wide. However, the depth and form of the ice layers within it have remained very similar to those observed in 2012. The boundary between the percolation and glacier ice zones was chosen by tracking the limit of a firn layer embedded within the ice that has undergone a small downslope displacement (<2 km) from kilometer 30 in 2012 to kilometer 32 in 2017. The major difference in the stratigraphy of the superimposed ice and glacier ice zones occurs at the surface. However, the GPR equipment used in this research is not very effective at capturing features right at the surface because it was chosen specifically for its capacity to distinguish ice layers at depth.

The color-coded CryoSat Line (Figure 4.4) is compared with the KE data derived from the TSX data acquired between June and August 2017. The GPR data were acquired on 12 and 17-May and the TSX data with the closest date to a KE image were acquired on May-13. Data from the CryoSat line superimposed on the TSX data (the interpretation of the TSX data is found in Chapter 2 – Item 2.5) shows a good fit only with the transition from the Wet-Snow Zone to the Superimposed Ice Zone (images from May and June - Figure 4.4) and no fit with any of the other glacier facies zone boundaries in the color-coded GPR transect. For instance, the transition between the wet-snow zone and superimposed ice zone is seen on the first 3 images (13- and 24-May and 26-June) when no surface melt had occurred at that elevation (1573 m a.s.l.). Previous studies report that the penetration depth of x-band SAR can reach up to 10.4 m (Rott, Sturm and Miller, 1993) and that seasonal snow cover can also be penetrated if dry (Müller, 2011). The GPR profile shows a higher ice content within 1m depth at km 11.8 than was found in the same location in the 2012 and 2017 GPR profile. Thus, considering the penetration potential of the x-band associated with the higher ice content in the upper meter of the CryoSat transect, the matching of the color-coded transect with the KE data is considered

proper. Yet, no ice buried below ~1 m depth was captured by the KE as would have been expected from the penetration depth potential of the radar. This is likely due to the fact that the ideal conditions for deep penetration of x-band occur in the dry-snow zone, which has disappeared from the DIC since ~ 2004–06 (Sylvestre and others, 2013; de Jong and others, 2018). Thus, the limited penetration depth in the percolation zone may be caused solely by the grain size of the snow and firn in the shallow subsurface.

As the melt season progresses (TSX data June-26 to August-20) there is no consistency between the GPR color-coded readings and the KE decomposed from TSX data. However, on 26-June and from 07 to 18-July the GPR transition between the Superimposed Ice and Glacier Ice zones coincides with an equivalent transition in the K_0 element (no correspondence with K_3 on 23-June and 07-July). The timing of acquisition of the TSX images relative to the seasonal progression of surface melting is likely the cause of this outcome as the presence of water at the surface changes the response of the x-band radar. Hence, the fit is an artifact created by the progression of surface melt and does not contribute to the detection of glacier facies zones.

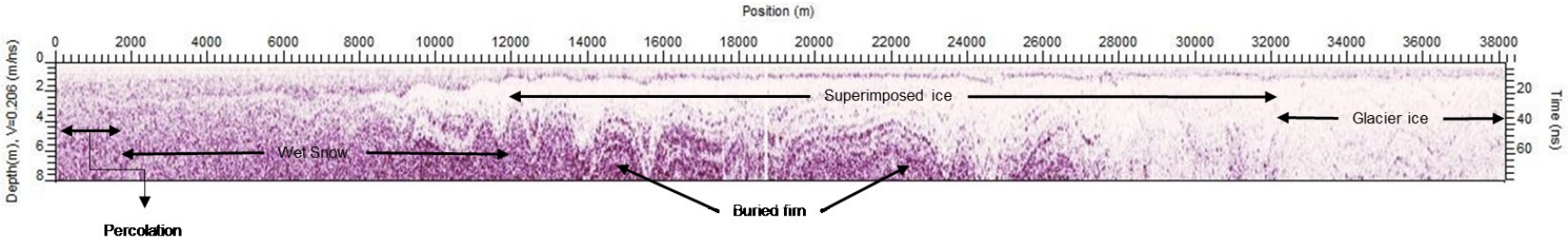

Figure 4.3 - GPR profile of the Cryosat line from Site-1 (0-km) to km-38. Lilac color represents firn and white layers represent ice.

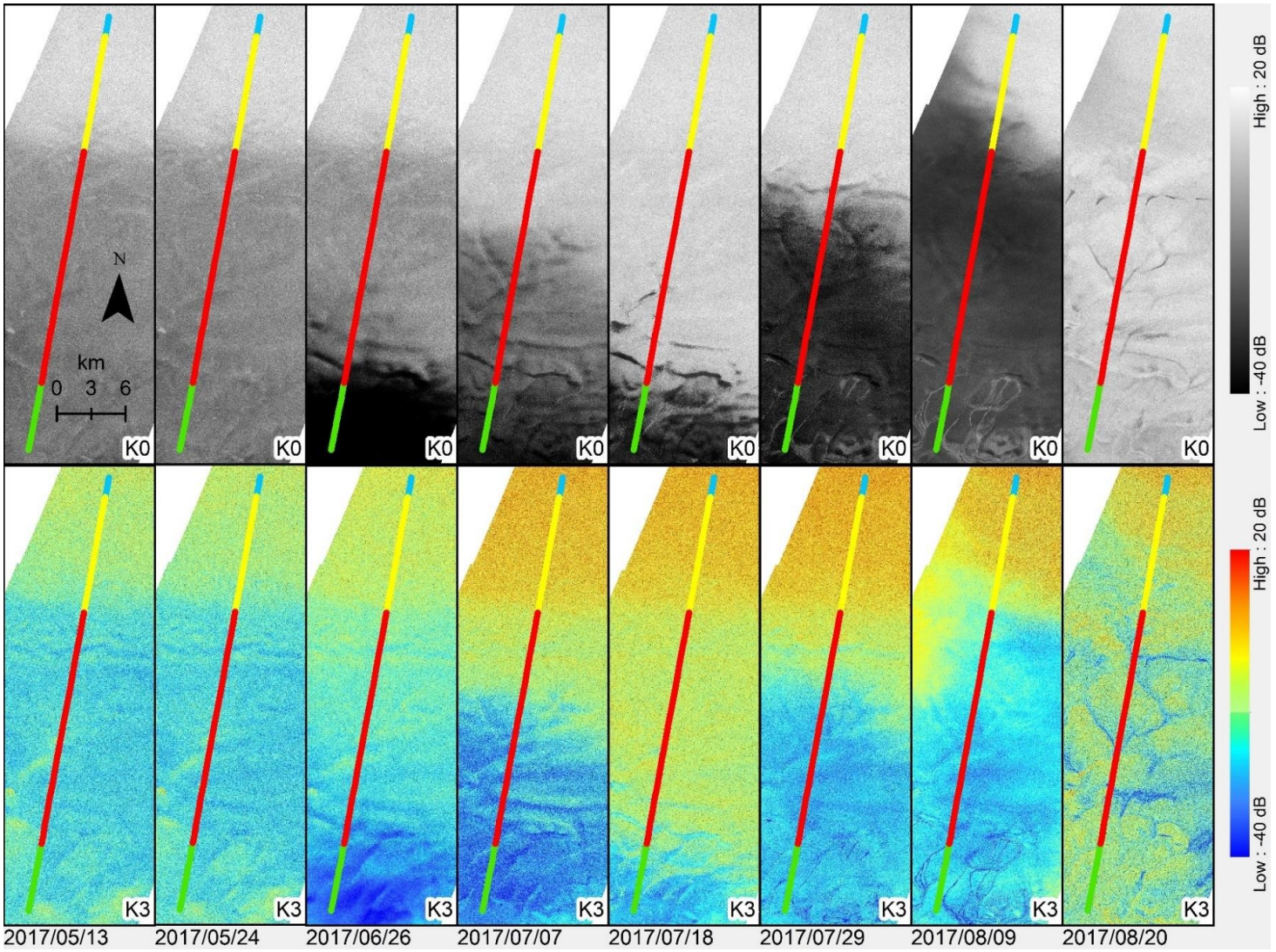

Figure 4.4 - GPR transect color-coded. The colors are displayed in respect to the characterization inferred from GPR data acquired in 2017. Green represents the Glacier Ice zone, red represents the Superimposed Ice Zone, yellow represents the wet-snow zone and cyan represents the percolation zone.

4.4.2 Grid lines and joint analysis with KE

In the wet-snow zone, where the grid lines are located, the stratigraphy is expected to present discontinuous and thin ice layers. Thus, the profiles collected in this region should have some scale variability in the IRH. The amount of surface melt produced in the grid area is roughly the same everywhere due to the small size of the study area, and the glacier slope has an important role in determining locations where meltwater should pond (Figure 4.5).

Ice layers are present along all grid lines and vary in thickness from thin (< 30cm) to thick (> 4m). Continuous ice layers prevail in this region although there are also some discontinuous layers. Discontinuous ice layers are usually found below concavities in thicker ice layers likely as a result of stretching and compression of the ice layers caused by flow over the subglacial bedrock topography (Budd, 1970). Ice layers in the grid area show a high level of stratification where the firn contains some very thin ice layers and the ice layers have some firn inclusions. Buried firn is found below all thick ice layers in the grid area. The surface topography modeled using elevation data from the GPS coupled to the GPR equipment shows 4 surface depressions (Figure 4.5 Box B 1-4). In these regions, a higher ice content is expected as these areas function as small-scale basins in which surface meltwater can pond. Similarly, a lower ice content is expected in profiles that cross regions in which the surface topography is in the form of small ridges.

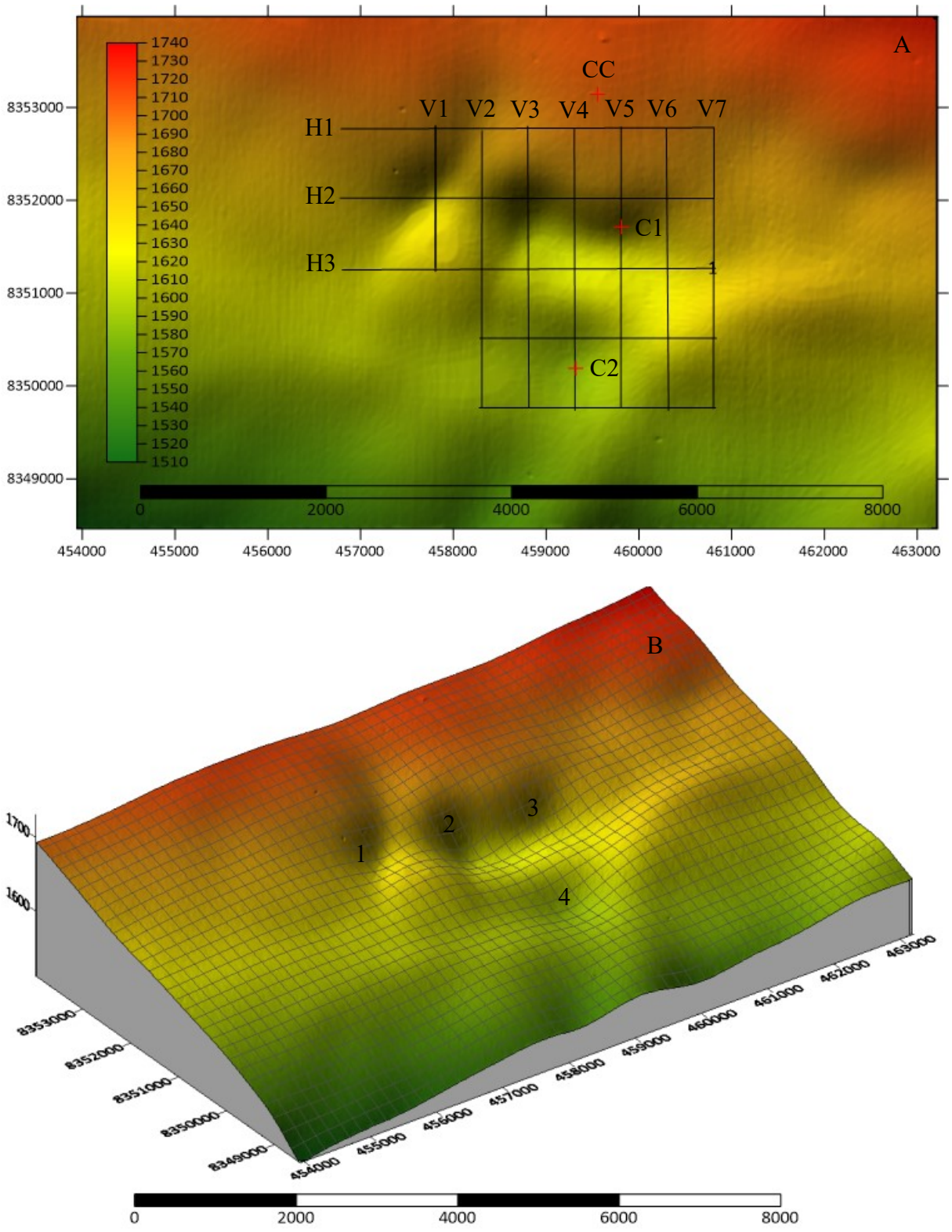

Figure 4.5 - Figure A displays the color relief contour of the grid area and the red crosses indicate the location of all 3 firn cores. Figure B shows the 3-D surface contour and the location of 4 surface depressions.

The ice layer detected along the vertical grid lines V3-V5 exhibits two concavities that are filled with firn (Figure 4.6). These concavities are conformable with the surface depressions visible on the modeled surface (areas 2, 3 and 4 (Figure 4.5 box B)). More and thicker ice layers are found along vertical transects V3-V5. Transect V1 contains discontinuous ice layers (<1.5 m thick) that extend across a concavity that is filled with firn. Transects V2-V7 also include some discontinuous ice layers in the concavities although the uppermost ice layer is essentially continuous over a distance of 3 km (V6 and V7).

The horizontal profiles display a gradual increase in ice layer thickness from the H1 transect (where the ice layers are ~1-2 m thick) to the H5 transect which is located further down-glacier (where they are up to 4 m thick) (Figure 4.7). The H1 transect includes some unique vertical intrusions of ice. On the H2 transect, which is immediately adjacent, there are some similar ice intrusions although they are less abundant than on H1. Such features are not present on transects H3-H5 where the ice layers are thicker and more continuous and occasionally incorporate pockets of embedded firn.

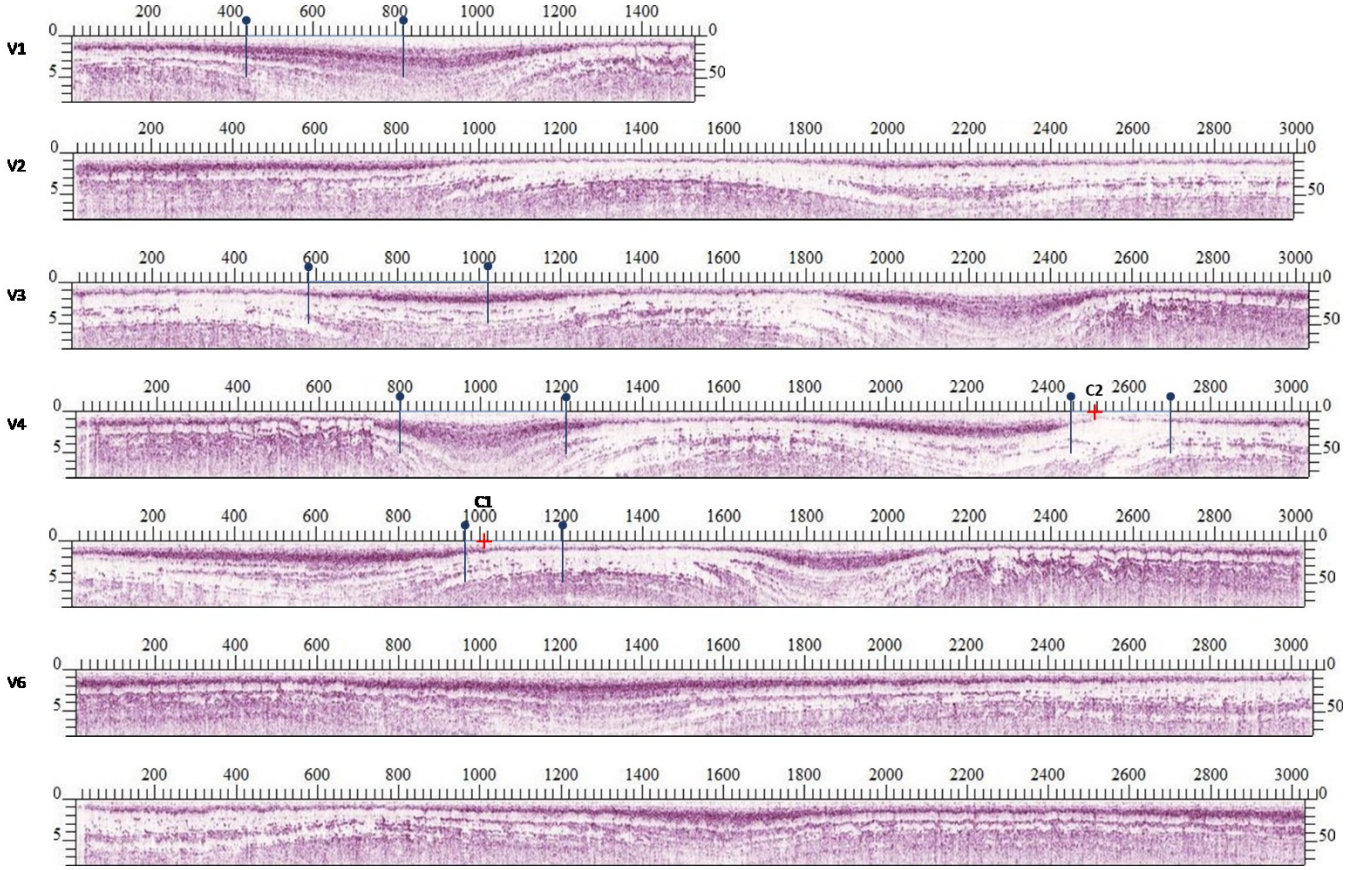

Figure 4.6: GPR profiles of the vertical lines that comprise the grid lines. The red crosses indicate the location at which firn cores 1 and 2 were drilled. The dots and lines indicate the section of the line that was superimposed on the KE image of the ice build-up anomaly at its maximum extent.

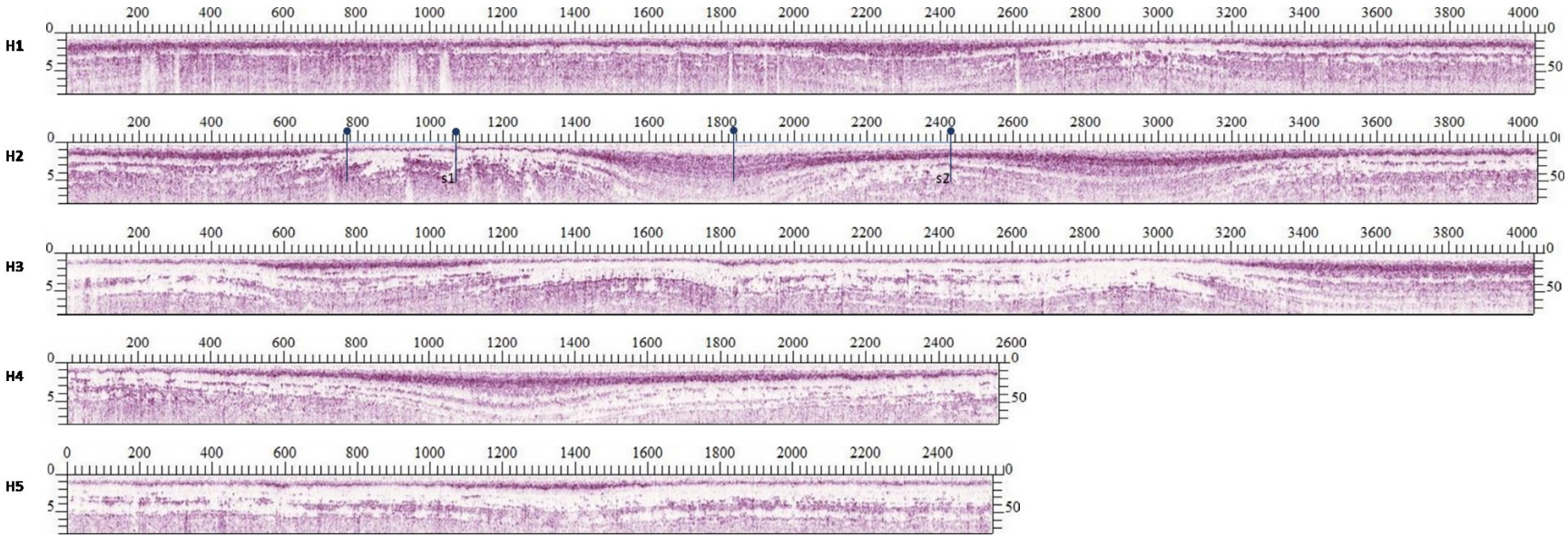

Figure 4.7: GPR profiles of the horizontal lines that compose the grid lines. The dots and lines indicate the section of the line that was superimposed on the KE image of the anomaly at its maximum extent.

Previous analysis of this area using imagery from Landsat-8 (Chapter 3 – Item 3.6.2) identified two small lakes in imagery from 2015 and 2016 (although they were smaller in 2016 than in 2015). Decomposition of TSX data identified 2 ice build-up anomalies in the same years. However, in 2017 they are only visible in the K_0 element (Chapter 2 – Item 2.5.1). Although the grid area was chosen for the purpose of identifying areas of ice build-up, not all transects intersected with the locations of lakes or ice thickness anomalies. The profiles that intersect the anomaly location (V1, V3, V4, V5 and H2) are shown in the respective profiles (Figure 4.1 Box B, Figure 4.5 Box A and Figure 4.6).

The Landsat-8 images of areas where lakes were found in 2015 and 2016, and TSX images of areas in which anomalies were found in either or both of the K_0/K_3 elements, were juxtaposed with color-code segmented grid lines using a classification obtained from the image in which the anomaly/lake reached its maximum extent (Figure 4.8). The location in which the anomalies developed coincides with the location of the surface depressions (Figure 4.5 – Box B 1-4). However, the interpretation of the GPR data from this area is not straightforward. Although the anomaly in the TSX K_0 element is visible in the image from August 9, 2017, it is totally absent in the K_3 element, which indicates that, at the time of the image acquisition, the ice cap surface was merely moist, and not wet enough to cause changes in the polarization of the K_3 element. The image in which the anomaly was most prominent (from August-14 2015) was acquired almost 2 years from the date on which the GPR profile was acquired (May 2017). Two sections of the H2 transect (H2s1 and H2s2) correspond with surface depressions 1 and 2 (Figure 4.5 box B). Both sections show ice within the firn, although, at H2s2 the ice layer is only found below 3m depth while, at H2s1, it is closer to the surface (only 1 m deep within the firn). The

response of the KE for both settings is very similar and may be explained by the locations at which the anomalies occur. The firn at H2s1 has a higher ice content close to the surface than does the firn at H2s2). H2s1 is located at the bottom of a hill although it is slightly inclined in the direction at which the TSX satellite acquires its images of the region. H2s2 is located on the hill in such way that the angle between the surface slope direction and the satellite orbit was smaller than at H2s1. This would influence the strength of the returned radar signal and the resulting KE, as would the proximity of the ice layer to the surface at the time of anomaly detection in 2015 (the 2017 GPR profile shows some accumulation in the area even though the accumulation on top of the ice layer would have been less at the time of the data acquisition).

The same effect caused by the geometry of the satellite acquisition and the surface slope explains the anomalies in V1, V3, V4s1 and V5. GPR transects V3, V4s1 and V5 are located on a steeper hill than V1, although the firn stratigraphy at V1 is similar to that found at V4s1. The section where the anomaly in V1 occurs is characterized by a thick layer of firn (> 2m from the surface) that contains scattered embedded thin ice layers. However, the two-year gap between the acquisition of the TSX data and the acquisition of the GPR data explains the absence of the anomaly in the TSX images. Likewise, the firn stratigraphy suggests an accumulation of >1 m of firn from 2015 to 2017, suggesting that the ice layer was closer to the surface at the time of the 2015 anomaly detection. The same interpretation can be used for the V3 and V6 sections that have a very similar firn stratigraphy to that found at V1, where a thick ice layer is <1.5m from the surface (V5 <1 m from the surface). Profile V4, located on the steepest hill, contains a buried ice layer located deeper in the stratigraphic profile (center of the section V4s1 > 5m deep) although thin ice layers are

also embedded within the firn close to the surface. The cause for such a strong anomaly (low values in K_3) is the presence of water near the surface at the time of the acquisition of TSX.

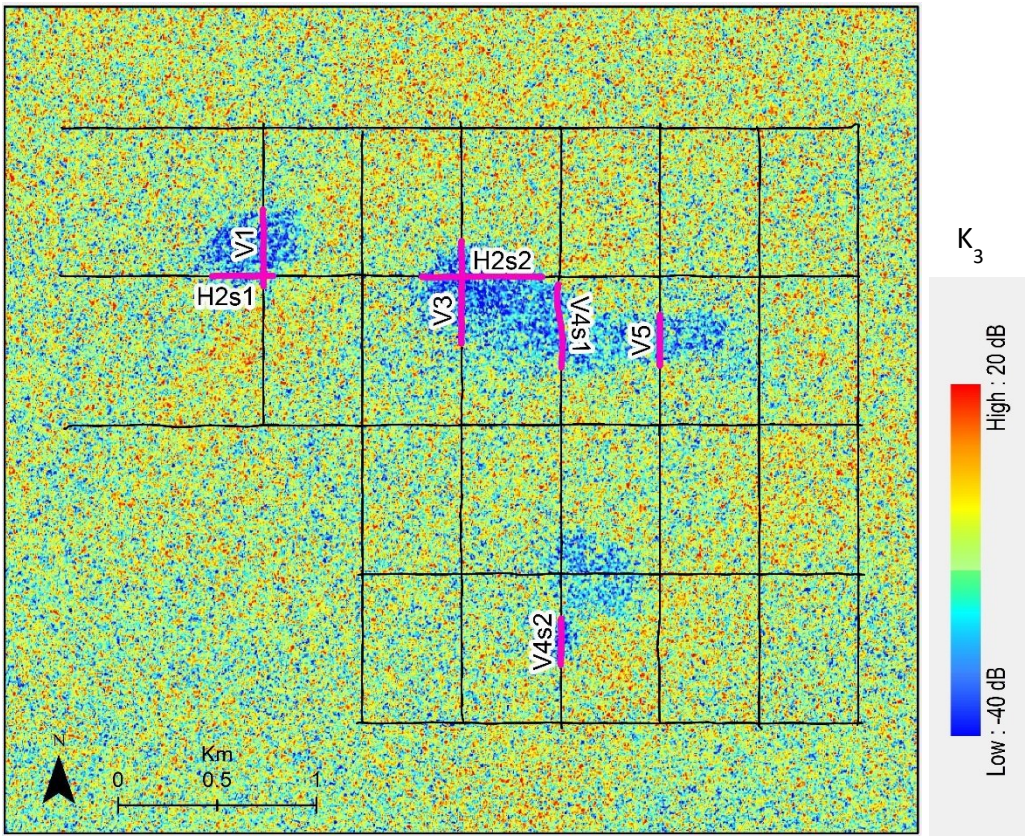

Figure 4.8: Pink highlight of the section of grid lines according to the maximum extent of the anomaly detected by TSX in August-14 2015 (only K_3 element is displayed).

The section V4s2 is located at the very bottom of depression 4 (Figure 4.8) and contains the highest concentration of ice in both the stratigraphic profile for the section and the firn core. Additionally, a seasonal lake is evident in exactly the same location in optical Landsat-8 images from 2015 and 2016. The anomaly in the TSX data was, however, only detected at this location in 2015. The high ice content of the 3.5 m firn core from this location suggests that a lake has formed in this location for several years. The time-

sensitive nature of the anomaly coupled with the TSX revisit time of 11 days is likely the cause for its apparent absence in subsequent years

However, the most remarkable result is the failure of the X-band data to detect the thick ice layers that are present in most grid transects below a depth of 1 m and, at times, the apparent inability of these data to detect ice layers that are even closer to the surface (for instance along the section of the V2 line between km 1.0 and km 1.8).

4.5 Conclusions

In this study, GPR data were collected and used to demonstrate spatial and temporal changes in the distribution of glacier facies zones on the southern flank of the Devon Ice Cap, by comparing GPR data acquired in 2012 and 2017. The observations showed an upward migration of the wet-snow zone onto the ice cap dome in the summer during this period. This resulted in the development of a continuous and thick ice layer at higher elevations. The presence of continuous ice layers at elevations up to 1784 m a.s.l. indicates an extreme decrease in the area of the percolation zone of the ice cap and a corresponding expansion of the wet-snow zone.

GPR data collected in grid format were used to check the presence of 2 lakes in the wet-snow zone of the ice cap that were detected in optical Landsat-8 images in 2015 and 2016 and in (TerraSAR-X) images from 2015-2017. By comparing the Kennaugh Elements derived from the TSX images with the GPR data we investigated the depth to which x-band SAR data can be used to infer the shallow-subsurface stratigraphy of the firn-covered regions of the ice cap. Although the KE detected an abnormal backscattering response over the same area in 3 successive years, the GPR data reveal that the penetration depth of x-

band products over the region does not exceed 1 m. This is likely related to the grain size of the firn and overlying fresh snow. However, the KE show promise as a tool for detecting shallow ice layers within the firn (buried up to 1 m below the surface), especially during the period after freeze-up when backscattering is characterized by a temporal switch from even (double – within the surface) to odd (higher surface contribution) bounce.

We showed that migration of glacier facies to higher elevations is happening more rapidly than expected due to the enlargement of ice layers within the firn. Results from our grid analysis suggest that annual monitoring using x-band data, especially using the KE derived from dual co-polarized TSX images, can provide useful evidence of the locations in which ice is forming close to ice cap surface as a result of freezing-induced accretion of surface meltwater on top of pre-existing ice layers within the firn.

Chapter 5 – Concluding Remarks and future work

One of the most challenging topics in glaciology is related to the study of firn processes such as meltwater retention, the heterogeneity of meltwater percolation, firn densification, the development of ice layers in firn, the detection and modeling of ice layer formation in firn, and the impact of ice layer development on the form of the supraglacial drainage network. Results presented in this thesis combined the use and analysis of optical (Landsat-7 and Landsat-8) and radar (TerraSAR-X) remote sensing data with analysis of ground-based measurements from Ground Penetrating radar and firn cores, and air temperature (2 m) data from an Automatic Weather Station to investigate the development of supraglacial drainage systems on the Devon Ice Cap and its connection to the formation of near-surface ice layers within the shallow part of the firn layer in the accumulation zone. Thus, the objectives of this research were to map and document the distribution and growth of ice bodies near the surface of the firn layer on the DIC and their evolution over time in order to assess and identify their impact on surface runoff patterns. To achieve this objective, three different methods were used.

In Chapter 2 “Detecting Supraglacial Meltwater Drainage On The Devon Ice Cap Using Kennaugh Decomposition Of The TerraSAR-X Imagery” we used the Kennaugh Decomposition elements of spatial and temporal changes in radar backscattering over firn-covered areas to detect the seasonal onset and freeze-up of melt, the spatial evolution of surface melt, and the seasonal development of supraglacial meltwater drainage systems on the DIC. The radiometric stability provided by the KE, which means no variation in the intensity of backscattering or polarimetry over time, delivered excellent results in the

detection of changes in the snow and firn and, especially, of changes associated with changes in the state of water.

Comparisons with the timing of melt onset at the different AWS during the study period showed a high degree of conformity between the AWS records and the KE results especially in the Wet-Snow, Superimposed Ice, and Bare Ice zones. Whenever meltwater was present at the surface, the K_0 element indicated low backscattering as a result of high absorption, which limited the penetration depth of the radar to a few centimeters. During periods of melt, the K_3 element repeatedly showed a shift from double bounce to a surface reflection. After freeze-up, however, this reverted to a double bounce reflection. For instance, melt (2m air temperature >0^{o}C) recorded at AWS Site-1 on July 1, 2015, was apparent in the KE records for that date although downward percolation occurred almost as soon as meltwater formed on the surface.

At the time the work for Chapter 2 began, we used the decomposition technique to map the development and expansion of the supraglacial drainage network. However, we found 5 patches within the Percolation Zone with KE signatures that we attributed to the presence of bare ice exposed by the removal of snow. This finding aroused our curiosity as to what was the nature of such an oddity. Thus, we added to the analysis the study of optical data from Landsat-7 and Landsat-8 to support our interpretation.

In Chapter 3 “Supraglacial Drainage Network Expansion On The Devon Ice Cap In Response To Changes In The Shallow Subsurface Hydrology Of Firn Covered Areas” changes in the distribution of surface meltwater channels and in the geometry of the mapped supraglacial drainage networks (2000-2017) within the firn region of the DIC were used as a proxy in the detection of shallow firn layers based on the concept that supraglacial

channels would only develop in areas where either the full pore volume of the firn column was filled with ice (Pfeffer and Meier, 1991; Fountain and Walder, 1998; Jansson, Hock and Schneider, 2003; Bøggild, Forsberg and Reeh, 2005; de Woul *et al.*, 2006; Harper *et al.*, 2012) or a thick and impermeable ice layer was present in the shallow sub-surface (Machguth *et al.*, 2016a; MacFerrin *et al.*, 2019). We analyzed the mapped supraglacial channels and lakes in combination with (a) the AWS 2 m air temperature records, (b) a classification of the glacier facies present in the study area and a map of their distribution, as derived from Landsat images, and (c) the expected distribution of surface lakes and meltwater channels that was derived from simulating the expected meltwater flow pathways over the DEM of the surface topography of the study area.

We found 16 different locations in which lakes occurred during the study period. Of these, Lakes 1 and 2 appeared in 15 and 16 years respectively of the 18 possible years for which data were available (2000-2017). These lakes were located at 918 and 943 m a.s.l. respectively. Both of these lakes formed very close to the mean elevation of the Snow-line (924 m a.s.l.) where ice forms as meltwater refreezes, forming either glacier ice or superimposed ice. The most intriguing lake development occurred in 2015 and 2016 when Lakes 13 and 14 formed. Both lakes were located in the percolation zone (at 1614 and 1590 m a.s.l., respectively), coincident with 2 (of the 5) patches that exhibit KE signatures that we associate with ice formation.

Supraglacial channels mapped during the period 2000-2017 provide clear evidence that the drainage network on the DIC is expanding to higher elevations (the maximum elevation of a single supraglacial channel reached ~1540 m a.s.l. in 2016). Our data show that the aggregate length of supraglacial channels increased with the annual sum of positive

degree days (PDD). Likewise, the expansion of the superimposed ice and bare ice zones is in accordance with the warming recorded in in situ air temperature records from the ice cap. The marked expansion of the wet-snow zone at the expense of the percolation zone is not directly reflected in the air temperature records even though we suspect that high temperatures during the period from 2010-2012 resulted in the refreezing of considerable amounts of meltwater as infiltration ice within the firn, which ultimately resulted in the development of impermeable layers in the shallow sub-surface layer of the percolation zone in the following years. The similarities in the distributions of the mapped and modeled supraglacial meltwater channels indicate that the surface topography is the primary control on the location in which new channels develop, especially at higher elevations.

Work reported in Chapter 4 “Detecting Ice Layers In The Percolation Zone Of The Oice Cap Using TerraSAR-X Images was motivated by the results presented in Chapter 2 and Chapter 3 and the need to determine whether the proposed methods are effective. The changes in the firn stratigraphy along the CryoSat line between the GPR datasets collected in 2012 and 2017 show the expansion of the wet-snow zone to higher elevations, consuming areas that used to be in the percolation zone. The total length of the wet-snow zone along the CryoSat line was 6.4 km in 2012 and 10.1 km in 2017. The boundary between the wet-snow zone and the Superimposed ice zone has also shifted to higher elevations. Thus, the most significant change in the glacier facies zones is attributed to the enlargement of the Superimposed Ice Zone from 14 km wide in 2012 to 20.2 km wide in 2017. Such results are in agreement with the results obtained from the Landsat-7 and Landsat-8 classifications and the distribution of the glacier facies zones. Although the general trend in the results is the same, in which the glacier facies zones are expanding to

higher elevations, the accuracy of the estimates provided by GPR measurements is likely greater because these data take into account the shallow subsurface firn structure, especially in the boundary region between the percolation zone and the wet-snow zone. The glacier facies zones identified in the GPR data (Chapter 4) and those identified in the TSX glacier zonation from 2015 (Chapter 2) show a better agreement particularly in the percolation and wet-snow zones due to the capability of TSX to penetrate the snow pack, which makes it possible to capture radar backscattering from the shallow subsurface of the firn, yielding results similar to those found in the GPR data.

The GPR grid data were acquired to investigate the ice build-up anomaly detected by TSX data that was later found to be associated with a lake that was visible on optical LandSat-8 images. According to the interpretation of data from the CryoSat line acquired in 2017, the area of the grid is located in the Wet-snow zone of the DIC. The wet-snow zone has very undulating ice layers usually within the upper 2-3 m of the firn. Layers in the grid area are more undulating than those observed on the CryoSat-line and include ice layers > 4m thick that are at times found within 1 meter of the surface. Ice layers that are close enough to the surface (within the first 1 m) and located on a slope are captured by the KE derived from TSX data.

Our observations of the development of supraglacial drainage systems in the accumulation area of the Devon Ice Cap, coupled with the ground truth obtained from the GPR measurements, indicate that the mapping and continuous surveillance of the development of new channels and lakes especially at higher elevations is an exceptional approach for characterizing the firn densification process. Supraglacial drainage systems will only develop in areas where the shallow sub-surface snow and firn contain ice layers

thick enough to limit meltwater percolation into the firn pore volume (Pfeffer and Meier, 1991; Harper *et al.*, 2012; Bezeau *et al.*, 2013; Gascon *et al.*, 2013; Machguth *et al.*, 2016b; Mikkelsen *et al.*, 2016). The combination of local surface slope, availability of surface meltwater, and presence of ice layers in the shallow sub-surface will determine the locations at which channels and lakes will form on the glacier or ice cap surface. Although there are some limitations to the approach, the observations made using the Kennaugh Elements decomposed from TerraSAR-X images can be used for the early detection of ice layer formation close to the ice cap surface in the percolation and wet-snow zones, in particular at the end of the melting season.

The most fascinating result from this work is that the existing model of glacier facies zonation (Benson, 1962) merits a review. Under the recent scenario of warmer temperatures happening in the Arctic summers, the subsequent increase in the generation of meltwater has imposed changes in the time frame at which glacier zones fluctuate its boundaries. Previous literature suggested that significant changes in glacier zones only occur after a prolonged period of consistent changes in one of the variables driving changes in the glacier zonation. This research has shown that not only the time frame for changes is shorter than suggested (migration of hundreds of meters in the WSL from one year to another – e.i. 2011 (average of 1221 m a.s.l.) and 2012 (average of 1553 m a.s.l.). We demonstrated that the glacier facies are under continuous modification from year to year, but most importantly, we found that supraglacial channels can develop not only at the lower limits of the wet-snow zone as previously suggested (Ferguson, 1973; Fountain, 1996; Chu, 2014; Chen, Howat and De La Peña, 2017) but anywhere where the substrate contains

enough ice to impede vertical percolation of meltwater, and that this includes the upper limits of the wet-snow zone.

Our observations have demonstrated the potential of X-band, specifically the Kennaugh decomposed elements, in detecting ice layers within the firn although with some limitation due to the x-band wavelength penetration into firn capacity. Further research should explore the applicability of Kennaugh Decomposition in other areas where increased melt has been detected such as in other ice caps in the Arctic and Greenland Ice Sheet as well as in areas of the Antarctica Peninsula. To examine and likely expand the potential of the Kennaugh Decomposition method, the experimentation with different bands is suggested. We believe that the addition of L-band and Ku band can be successful in the study of ice layers early detection in firn. The use of optical data for mapping the evolving supraglacial channels and lakes can be improved with the addition of other optical images such as WorldView imagery. Optical images with a better spatial resolution and/or revisit times will positively impact the availability of information regarding supraglacial development in all glacier areas. Supraglacial channels and lakes appearance on the accumulation zone are a visible indication of changes occurring in the subsurface substrate. Thus, this information can be used to support interpretations of supraglacial runoff impact on the densification of firn in the accumulation area of glaciers.

.

Bibliography

AMAP-SWIPA (2017) *Snow, Water, Ice and Permafrost in the Arctic (SWIPA) 2017*. Oslo.

Van Angelen, J. H. *et al.* (2013) 'Rapid loss of firn pore space accelerates 21st century Greenland mass loss', *Geophysical Research Letters*, 40(10), pp. 2109–2113. doi: 10.1002/grl.50490.

'ArcticDEM Documentation and User Guidance' (2017), pp. 1–10. Available at: http://www.vedur.is/media/frettir/ArcticDEM_Documentation_and_User-Guidance_Rel4.pdf.

van As, D., Box, J. E. and Fausto, R. S. (2016) 'Challenges of quantifying meltwater retention in snow and firn: an expert elicitation', *Frontiers in Earth Science*, 4(December), p. Article 101. doi: 10.3389/feart.2016.00101.

Benson, C. S. (1962) 'Stratigraphic studies in the snow and firn of the Greenland Ice Sheet', *Folia Geographica Danica*. Hanover: Cold Reg. Res. and Eng. Lab, 70(August), pp. 13–37.

Bezeau, P. *et al.* (2013) 'Firn profile changes in response to extreme 21st-century melting at Devon Ice Cap, Nunavut, Canada', *Journal of Glaciology*, 59(217), pp. 981–991. doi: 10.3189/2013JoG12J208.

Blunden, J., Arndt, D. S. and Hartfield, G. (2018) *State of the climate in 2017*. doi: 10.1175/2018BAMSStateoftheClimate.1.

Bøggild, C. E., Forsberg, R. and Reeh, N. (2005) 'Meltwater retention in a transect across the Greenland ice sheet', *Annals of Glaciology*, 40, pp. 169–173. doi: 10.3189/172756405781813546.

Bolch, T. *et al.* (2008) 'Planimetric and volumetric glacier changes in the Khumbu Himal, Nepal, since 1962 using Corona, Landsat TM and ASTER data', *Journal of Glaciology*, 54(187), pp. 592–600. doi: 10.3189/002214308786570782.

Boon, S. *et al.* (2010) 'Forty-seven Years of Research on the Devon Island Ice Cap , Arctic Canada', 63(1), pp. 13–29.

Boon, S. and Sharp, M. (2003) 'The role of hydrologically-driven ice fracture in drainage system evolution on an Arctic glacier', *Geophysical Research Letters*, 30(18), pp. 3–6. doi: 10.1029/2003GL018034.

Braithwaite, R. J. (1995) 'Positive degree-day factors for ablation on the Greenland ice sheet studied by energy-balance modelling', *Journal of Glaciology*, 41(137), pp. 153–160.

Burgess, D. O. *et al.* (2005) 'Flow dynamics and iceberg calving rates of Devon Ice Cap,

Nunavut, Canada', *Journal of Glaciology*, 51(173), pp. 219–230. doi: 10.3189/172756505781829430.

Burgess, D. and Sharp, M. J. (2008) 'Recent changes in thickness of the Devon Island ice cap, Canada', *Journal of Geophysical Research*, 113(B7), p. B07204. doi: 10.1029/2007JB005238.

Casey, J. A. and Kelly, R. E. J. (2010) 'Estimating the equilibrium line of Devon Ice Cap, Nunavut, from RADARSAT-1 ScanSAR wide imagery', *Canadian Journal of Remote Sensing*, 36(June), pp. S41–S55. doi: 10.5589/m10-013.

Chen, C., Howat, I. M. and De La Peña, S. (2017) 'Formation and development of supraglacial lakes in the percolation zone of the Greenland ice sheet', *Journal of Glaciology*, 63(241), pp. 847–853. doi: 10.1017/jog.2017.50.

Chu, V. W. (2014) 'Greenland ice sheet hydrology', *Progress in Physical Geography*, 38(1), pp. 19–54. doi: 10.1177/0309133313507075.

Cogley, J. G. *et al.* (2011) *Glossary of glacier mass balance and related terms*. IHP-VII Te. Paris: UNESCO Working Series SC-2011/WS/4.

Cuffey, K. M. and Paterson, W. S. B. (2010) *The physics of glaciers*. 4th edn. Elsevier Inc.

Dowdeswell, J. a. (2004) 'Form and flow of the Devon Island Ice Cap, Canadian Arctic', *Journal of Geophysical Research*, 109(F2), pp. 1–14. doi: 10.1029/2003JF000095.

Echelmeyer, K. *et al.* (1992) 'Surficial glaciology of Jakobshavns Isbrae, West Greenland: Part 11. Ablation, accumulation and temperature', *Journal of Glaciology*, 38(128), pp. 169–181.

Ferguson, R. I. (1973) 'Sinuosity of supraglacial streams', *Bulletin of the Geological Society of America*, 84(1), pp. 251–256.

Fisher, D. *et al.* (2012) 'Recent melt rates of Canadian arctic ice caps are the highest in four millennia', *Global and Planetary Change*. Elsevier B.V., 84–85, pp. 3–7. doi: 10.1016/j.gloplacha.2011.06.005.

Flowers, G. E. and Clarke, G. K. C. (2002) 'A multicomponent coupled model of glacier hydrology 2. Application to Trapridge Glacier, Yukon, Canada', *Journal of Geophysical Research*, 107(B11), p. 2288. doi: 10.1029/2001JB001124.

Forster, R. R. *et al.* (2013) 'Extensive liquid meltwater storage in firn within the Greenland ice sheet', *Nature Geoscience*. Nature Publishing Group, 7(2), pp. 95–98. doi: 10.1038/ngeo2043.

Fountain, A. G. (1996) 'Effect of snow and firn hydrology on the physical and chemical characersitics of glacial runoff', *Hydrological Processes*, 10, pp. 509–521.

Fountain, A. G. and Walder, J. S. (1998) 'Water flow through temperate glaciers', *Reviews of Geophysics*, 36(97), p. 299. doi: 10.1029/97RG03579.

Gardner, A. S. *et al.* (2011) 'Sharply increased mass loss from glaciers and ice caps in the Canadian Arctic Archipelago.', *Nature*. Nature Publishing Group, 473(7347), pp. 357–60. doi: 10.1038/nature10089.

Gardner, A. S. *et al.* (2013) 'A Reconciled Estimate of Glacier Contributions to Sea Level Rise: 2003 to 2009', *Science*, 340(6134), pp. 852–857. doi: 10.1126/science.1234532.

Gascon, G. *et al.* (2013) 'Changes in accumulation-area firn stratigraphy and meltwater flow during a period of climate warming: Devon Ice Cap, Nunavut, Canada', *Journal of Geophysical Research: Earth Surface*, 118(4), pp. 2380–2391. doi: 10.1002/2013JF002838.

Gascon, G. *et al.* (2014) 'How well is firn densification represented by a physically based multilayer model? Model evaluation for Devon Ice Cap, Nunavut, Canada', *Journal of Glaciology*, 60(222), pp. 694–704. doi: 10.3189/2014JoG13J209.

Gascon, G., Sharp, M. and Bush, A. (2013) 'Changes in melt season characteristics on Devon Ice Cap, Canada, and their association with the Arctic atmospheric circulation', *Annals of Glaciology*, 54(63), pp. 101–110. doi: 10.3189/2013AoG63A601.

Gleason, C. J. *et al.* (2016) 'Characterizing supraglacial meltwater channel hydraulics on the Greenland Ice Sheet from in situ observations', *Earth Surface Processes and Landforms*, 41(14), pp. 2111–2122. doi: 10.1002/esp.3977.

Gray, L. *et al.* (2015) 'CryoSat-2 delivers monthly and inter-annual surface elevation change for Arctic ice caps', *Cryosphere*, 9(5), pp. 1895–1913. doi: 10.5194/tc-9-1895-2015.

Greuell, W. and Knap, W. (2000) 'Remote sensing of the albedo and detection of the slush line on the Greenland ice sheet', 105(1999), pp. 15567–15576.

Grinsted, A. (2013) 'An estimate of global glacier volume', *The Cryosphere*, 7(1), pp. 141–151. doi: 10.5194/tc-7-141-2013.

Guissard, A. (1994) 'Mueller and Kennaugh matrices in radar polarimetry', *IEEE Transactions on Geoscience and Remote Sensing*, 32(3), pp. 590–597. doi: 10.1109/36.297977.

Harig, C. and Simons, F. J. (2016) 'Ice mass loss in Greenland, the Gulf of Alaska, and the Canadian Archipelago: Seasonal cycles and decadal trends', *Geophysical Research Letters*, 43(7), pp. 3150–3159. doi: 10.1002/2016GL067759.

Harper, J. *et al.* (2012) 'Greenland ice-sheet contribution to sea-level rise buffered by

meltwater storage in firn.', *Nature*. Nature Publishing Group, 491(7423), pp. 240–3. doi: 10.1038/nature11566.

Hindmarsh, R. C. A. *et al.* (2006) 'Draping or overriding: The effect of horizontal stress gradients on internal layer architecture in ice sheets', *Journal of Geophysical Research: Earth Surface*, 111(2). doi: 10.1029/2005JF000309.

Hock, R. (2005) 'Glacier melt: a review of processes and their modelling', *Progress in Physical Geography*, 29(3), pp. 362–391. doi: 10.1191/0309133305pp453ra.

Humphrey, N. F., Harper, J. T. and Pfeffer, W. T. (2012) 'Thermal tracking of meltwater retention in Greenland's accumulation area', *Journal of Geophysical Research*, 117(F1), p. F01010. doi: 10.1029/2011JF002083.

Huss, M. and Farinotti, D. (2012) 'Distributed ice thickness and volume of all glaciers around the globe', *Journal of Geophysical Research*, 117(4), pp. 1–10. doi: 10.1029/2012JF002523.

Huybrechts, P. and Oerlemans, J. (1990) 'Response of the Antarctic ice sheet to future greenhouse warming', *Climate Dynamics*, 5(1990), pp. 93–102.

Iken, A. (1972) 'Measurements of water pressure in moulins as part of a movement study of the White glacier, Axel Heiberg Island, Northwest Territories, Canada', *Journal of Glaciology*, 11(61), pp. 53–58.

Iken, A. *et al.* (1983) 'The uplift of Unteraargletscher at the beginning of the melt season - a consequence of water storage at the bed?', *Journal of Glaciology*, 29(101), pp. 28–47. doi: 10.1017/S0022143000005128.

IPCC - Climate Change 2013: The Physical Science Basis. Contribution of Working Group I to the Fifth Assessment Report of the Intergovernmental (2013). Cambridge, United Kingdom and New York, NY USA.

Irvine-Fynn, T. D. L. *et al.* (2011) 'Polythermal Glacier Hydrology: A Review', *Rev. Geophys.*, 49(2010), pp. 1–37. doi: 10.1029/2010RG000350.1.INTRODUCTION.

Jansson, P., Hock, R. and Schneider, T. (2003) 'The concept of glacier storage: A review', *Journal of Hydrology*, 282(1–4), pp. 116–129. doi: 10.1016/S0022-1694(03)00258-0.

Jenson, S. K. and Domingue, J. O. (1988) 'Extracting topographic structure from digital elevation data for geographic information system analysis', *Photogrammetric Engineering and Remote Sensing*, 54(11), pp. 1593–1600. doi: 0099-1112/88/5411.

de Jong, T., Copland, L. and Burgess, D. (2018) 'Changes in glacier facies zonation on Devon Ice Cap, Nunavut, detected from SAR imagery and field observations', *The Cryosphere Discussions*, 1(November 2018).

Karlstrom, L., Gajjar, P. and Manga, M. (2013) 'Meander formation in supraglacial streams', *Journal of Geophysical Research: Earth Surface*, 118(3), pp. 1897–1907. doi: 10.1002/jgrf.20135.

Kaufman, D. S. *et al.* (2009) 'Recent Warming Reverses Long-Term Arctic Cooling', *Science (New York, N.Y.)*, 325(September), pp. 1236–1239.

King, L. *et al.* (2016) 'Flow routing for delineating supraglacial meltwater channel networks', *Remote Sensing*, 8(12), pp. 1–21. doi: 10.3390/rs8120988.

Knighton, A. D. (1985) 'Channel form adjustment in supraglacial streams, Austre Okstindbreen, Norway.', *Arctic & Alpine Research*, 17(4), pp. 451–466. doi: 10.2307/1550870.

Koenig, L. S. *et al.* (2015) 'Wintertime storage of water in buried supraglacial lakes across the Greenland Ice Sheet', *Cryosphere*, 9(4), pp. 1333–1342. doi: 10.5194/tc-9-1333-2015.

Lampkin, D. J. and Vanderberg, J. (2011) 'A preliminary investigation of the influence of basal and surface topography on supraglacial lake distribution near Jakobshavn Isbrae, western Greenland', *Hydrological Processes*, 25(21), pp. 3347–3355. doi: 10.1002/hyp.8170.

Lampkin, D. J. and Vanderberg, J. (2014) 'Supraglacial melt channel networks in the Jakobshavn Isbrae region during the 2007 melt season', *Hydrological Processes*, 28(25), pp. 6038–6053. doi: 10.1002/hyp.10085.

Leeson, A. A. *et al.* (2015) 'Supraglacial lakes on the Greenland ice sheet advance inland under warming climate', *Nature Climate Change*, 5(1), pp. 51–55. doi: 10.1038/nclimate2463.

Li, H. *et al.* (2015) 'Integrating a glacier retreat model into a hydrological model – Case studies of three glacierised catchments in Norway and Himalayan region', *Journal of Hydrology*, 527, pp. 656–667. doi: 10.1016/j.jhydrol.2015.05.017.

Li, J. and Wong, D. W. S. (2010) 'Effects of DEM sources on hydrologic applications', *Computers, Environment and Urban Systems*. Elsevier Ltd, 34(3), pp. 251–261. doi: 10.1016/j.compenvurbsys.2009.11.002.

Long, D. G. and Drinkwater, M. R. (1994) 'Greenland ice-sheet surface properties observed by the Seasat-A scatterometer at enhanced resolution', *Journal of Glaciology*, 40(135), pp. 213–230. doi: 10.1017/S0022143000007310.

MacFerrin, M. *et al.* (2019) 'Rapid expansion of Greenland's low-permeability ice slabs', *Nature*. Springer US, 573(7774), pp. 403–407. doi: 10.1038/s41586-019-1550-3.

Machguth, H. *et al.* (2016a) 'Greenland meltwater storage in firn limited by near-surface ice formation', *Nature Clim. Change*, 6, pp. 390–393. doi: 10.1038/nclimate2899.

Machguth, H. *et al.* (2016b) 'Greenland meltwater storage in firn limited by near-surface ice formation', *Nature Clim. Change*, advance on(January), pp. 1–6. doi: 10.1038/nclimate2899.

Mair, D., Burgess, D. and Sharp, M. (2005) 'Thirty-seven year mass balance of Devon Ice Cap, Nunavut, Canada, determined by shallow ice coring and melt modeling', *Journal of Geophysical Research: Earth Surface*, 110(1), pp. 1–13. doi: 10.1029/2003JF000099.

Malnes, E. *et al.* (2006) 'Multi-polarisation measurements of snow signatures with air- and satelliteborne SAR', *EARSeL eProceedings*, (January 2015), pp. 111–119.

Marston, R. A. (1983) 'Supraglacial Stream Dynamics on the Juneau Icefield', *Annals of the Association of American Geographers*, 73(4), pp. 597–608.

Marzeion, B., Jarosch, A. H. and Hofer, M. (2012) 'Past and future sea-level change from the surface mass balance of glaciers', *The Cryosphere*, 6, pp. 1295–1322. doi: 10.5194/tc-6-1295-2012.

Mikkelsen, A. B. *et al.* (2016) 'Extraordinary runoff from the Greenland ice sheet in 2012 amplified by hypsometry and depleted firn retention', *Cryosphere*, 10(3), pp. 1147–1159. doi: 10.5194/tc-10-1147-2016.

Mortimer, C. A., Sharp, M. and Wouters, B. (2016) 'Glacier surface temperatures in the Canadian High Arctic, 2000–15', *Journal of Glaciology*. doi: 10.1017/jog.2016.80.

Muller (1961) 'Zonation in the Accumulation Area of the Glaciers of Axel Heiberg Island, N.W.T., Canada', *Journal of Glaciology*, 4(33), pp. 302–311.

Naz, B. S. *et al.* (2014) 'Modeling the effect of glacier recession on streamflow response using a coupled glacio-hydrological model', *Hydrology and Earth System Sciences*, 18(2), pp. 787–802. doi: 10.5194/hess-18-787-2014.

Nghiem, S. V. *et al.* (2005) 'Mapping of ice layer extent and snow accumulation in the percolation zone of the Greenland ice sheet', *Journal of Geophysical Research: Earth Surface*, 110(2), pp. 1–13. doi: 10.1029/2004JF000234.

Nienow, P. and Hubbard, B. (2005) 'Surface and Englacial Drainage of Glaciers and Ice Sheets', *Encyclopedia of Hydrological Sciences*, pp. 1–12. doi: 10.1002/0470848944.hsa172.

Palmer, S. *et al.* (2011) 'Seasonal speedup of the Greenland Ice Sheet linked to routing of surface water', *Earth and Planetary Science Letters*. Elsevier B.V., 302(3–4), pp. 423–428. doi: 10.1016/j.epsl.2010.12.037.

Pfeffer, W. T. and Humphrey, N. (1998) 'Formation of ice layers by infiltration and refreezing of meltwater', *Annal of Glaciology*, (26), pp. 83–91.

Pfeffer, W. T. and Humphrey, N. F. (1996) 'Determination of timing and location of water movement and ice-layer formation by temperature measurement in sub-freezing snow', *Journal of Glaciology*, 42(141), pp. 292–304.

Pfeffer, W. T. and Meier, M. F. (1991) 'Retention of Greenland runoff by refreezing: Implications for projected future sea level change', *Journal of Geophysical Research*, 96(C12), p. 22117. doi: 10.1029/91JC02502.

Phillips, T. *et al.* (2013) 'Evaluation of cryo-hydrologic warming as an explanation for increased ice velocities in the wet snow zone, Sermeq Avannarleq, West Greenland', *Journal of Geophysical Research: Earth Surface*, 118(3), pp. 1241–1256. doi: 10.1002/jgrf.20079.

Radić, V. *et al.* (2014) 'Regional and global projections of twenty-first century glacier mass changes in response to climate scenarios from global climate models', *Climate Dynamics*, 42(1–2), pp. 37–58. doi: 10.1007/s00382-013-1719-7.

Radić, V. and Hock, R. (2011) 'Regionally differentiated contribution of mountain glaciers and ice caps to future sea-level rise', *Nature Geoscience*, 4(2), pp. 91–94. doi: 10.1038/ngeo1052.

'Randolph Glacier Inventory – A Dataset of Global Glacier Outlines: Version 6.0: Technical Report, Global Land Ice Measurements from Space, Colorado, USA. Digital Media.' (2017). doi: https://doi.org/10.7265/N5-RGI-60.

Rennermalm, a. K. *et al.* (2013) 'Evidence of meltwater retention within the Greenland ice sheet', *The Cryosphere*, 7(5), pp. 1433–1445. doi: 10.5194/tc-7-1433-2013.

Rippin, D. M., Pomfret, A. and King, N. (2015) 'High resolution mapping of supraglacial drainage pathways reveals link between micro-channel drainage density, surface roughness and surface reflectance', *Earth Surface Processes and Landforms*, 1290(March), p. n/a-n/a. doi: 10.1002/esp.3719.

Rutishauser, A. *et al.* (2016) 'Characterizing near - surface firn using the scattered signal component of the glacier surface return from airborne radio - echo sounding', *Geophysical Research Letters*, (Dic), pp. 1–9. doi: 10.1002/2016GL071230.

Scaramuzza, P., Micijevic, E. and Chander, G. (2004) *SLC Gap-filled products - Phase one methodology*.

Schmitt, A., Wendleder, A. and Hinz, S. (2015) 'The Kennaugh element framework for multi-scale, multi-polarized, multi-temporal and multi-frequency SAR image preparation', *ISPRS Journal of Photogrammetry and Remote Sensing*. International Society for Photogrammetry and Remote Sensing, Inc. (ISPRS), 102, pp. 122–139. doi: 10.1016/j.isprsjprs.2015.01.007.

Selmes, N., Murray, T. and James, T. D. (2011) 'Fast draining lakes on the Greenland Ice Sheet', *Geophysical Research Letters*, 38(15), pp. 1–5. doi:

10.1029/2011GL047872.

Sharp, M. *et al.* (2011) 'Extreme melt on Canada's Arctic ice caps in the 21st century', *Geophysical Research Letters*, 38(11), p. n/a-n/a. doi: 10.1029/2011GL047381.

Singh, V., Singh, P. and Haritashya, U. (eds) (2011) *Encyclopedia of Snow, Ice and Glaciers*. Dordrecht: Springer US.

Smart, C. C. *et al.* (2000) 'Exceptional ablation arising from rainfall-induced slushflows: Brewster Glacier, New Zealand', *Hydrological Processes*, 14(6), pp. 1045–1052. doi: 10.1002/(SICI)1099-1085(20000430)14:6<1045::AID-HYP995>3.0.CO;2-9.

Smith, L. C. *et al.* (2015) 'Efficient meltwater drainage through supraglacial streams and rivers on the southwest Greenland ice sheet', *Proceedings of the National Academy of Sciences*, 112(4), pp. 1001–1006. doi: 10.1073/pnas.1413024112.

Sugden, D. E. and John, B. S. (1976) *Glaciers and landscape: a geomorphological approach*. London: Edward Arnold.

Sylvestre, T. *et al.* (2013) 'Spatial patterns of snow accumulation across Belcher Glacier, Devon Ice Cap, Nunavut, Canada', *Journal of Glaciology*, 59(217), pp. 874–882. doi: 10.3189/2013JoG12J227.

Tedesco, M. *et al.* (2013) 'Ice dynamic response to two modes of surface lake drainage on the Greenland ice sheet', *Environmental Research Letters*, 8(3). doi: 10.1088/1748-9326/8/3/034007.

Wang, L. *et al.* (2005) 'Melt season duration on Canadian Arctic ice caps, 2000-2004', *Geophysical Research Letters*, 32(19), pp. 1–4. doi: 10.1029/2005GL023962.

Washburn, A. (1980) *Geocryology: A survey of periglacial processes and environments*. New York: John Wiley & Sons.

Wendleder, A., Roth, A. and Schmitt, A. (2014) 'Monitoring of ice growth on the East channel and on shallow lakes in the Mackenzie Delta', *EUSAR*, pp. 931–934.

Wolken, G. J., Sharp, M. and Wang, L. (2009) 'Snow and ice facies variability and ice layer formation on Canadian Arctic ice caps, 1999-2005', *Journal of Geophysical Research: Solid Earth*, 114(June), pp. 1999–2005. doi: 10.1029/2008JF001173.

de Woul, M. *et al.* (2006) 'Firn layer impact on glacial runoff: A case study at Hofsjökull, Iceland', *Hydrological Processes*, 20(10), pp. 2171–2185. doi: 10.1002/hyp.6201.

Wouters, B., Gardner, A. S. and Moholdt, G. (2019) 'Global glacier mass loss during the GRACE satellite mission (2002-2016)', *Frontiers in Earth Science*, 7(May), pp. 1–11. doi: 10.3389/feart.2019.00096.

Wyatt, F. R. (2013) *The spatial structure and temporal development of supraglacial*

drainage systems, and their influence on the flow dynamics of High Arctic ice caps. University of Alberta.

Wyatt, F. R. and Sharp, M. J. (2015) 'Linking surface hydrology to flow regimes and patterns of velocity variability on Devon Ice Cap, Nunavut', *Journal of Glaciology*, 61(226), pp. 387–399. doi: 10.3189/2015JoG14J109.

Van Wychen, W. *et al.* (2012) 'Spatial and temporal variation of ice motion and ice flux from Devon Ice Cap, Nunavut, Canada', *Journal of Glaciology*, 58(210), pp. 657–664. doi: 10.3189/2012JoG11J164.

Yang, K., Smith, L. C. L. C. L. C. L. C., *et al.* (2015) 'A caution on the use of surface digital elevation models to simulate supraglacial hydrology of the Greenland ice sheet', *IEEE Journal of Selected Topics n Applie Earth Observations and Remote Sensing*, 8(11), pp. 5212–5224. doi: 10.1109/JSTARS.2015.2483483.

Yang, K., Li, M., *et al.* (2015) 'River detection in remotely sensed imagery using Gabor filtering and path opening', *Remote Sensing*, 7(7), pp. 8779–8802. doi: 10.3390/rs70708779.

Yang, K. *et al.* (2016) 'Fluvial morphometry of supraglacial river networks on the Southwest Greenland ice sheet', *GIScience and Remote Sensing*. Taylor & Francis, 53(4), pp. 459–482. doi: 10.1080/15481603.2016.1162345.

Yang, K. and Smith, L. C. (2013) 'Supraglacial streams on the greenland ice sheet delineated from combined spectral-shape information in high-resolution satellite imagery', *IEEE Geoscience and Remote Sensing Letters*, 10(4), pp. 801–805. doi: 10.1109/LGRS.2012.2224316.

Yang, K. and Smith, L. C. (2016) 'Internally drained catchments dominate supraglacial hydrology of the southwest Greenland Ice Sheet', *Journal of Geophysical Research: Earth Surface*, pp. 1891–1910. doi: 10.1002/2016JF003927.

Zdanowicz, C. *et al.* (2012) 'Summer melt rates on Penny Ice Cap, Baffin Island: Past and recent trends and implications for regional climate', *Journal of Geophysical Research*, 117(F2), p. F02006. doi: 10.1029/2011JF002248.

Zwally, H. J. *et al.* (2002) 'Surface Melt – Induced Acceleration of Greenland Ice-Sheet Flow', *Science*, 218, pp. 218–223. doi: 10.1126/science.1072708.

Appendix A - Chapter 2

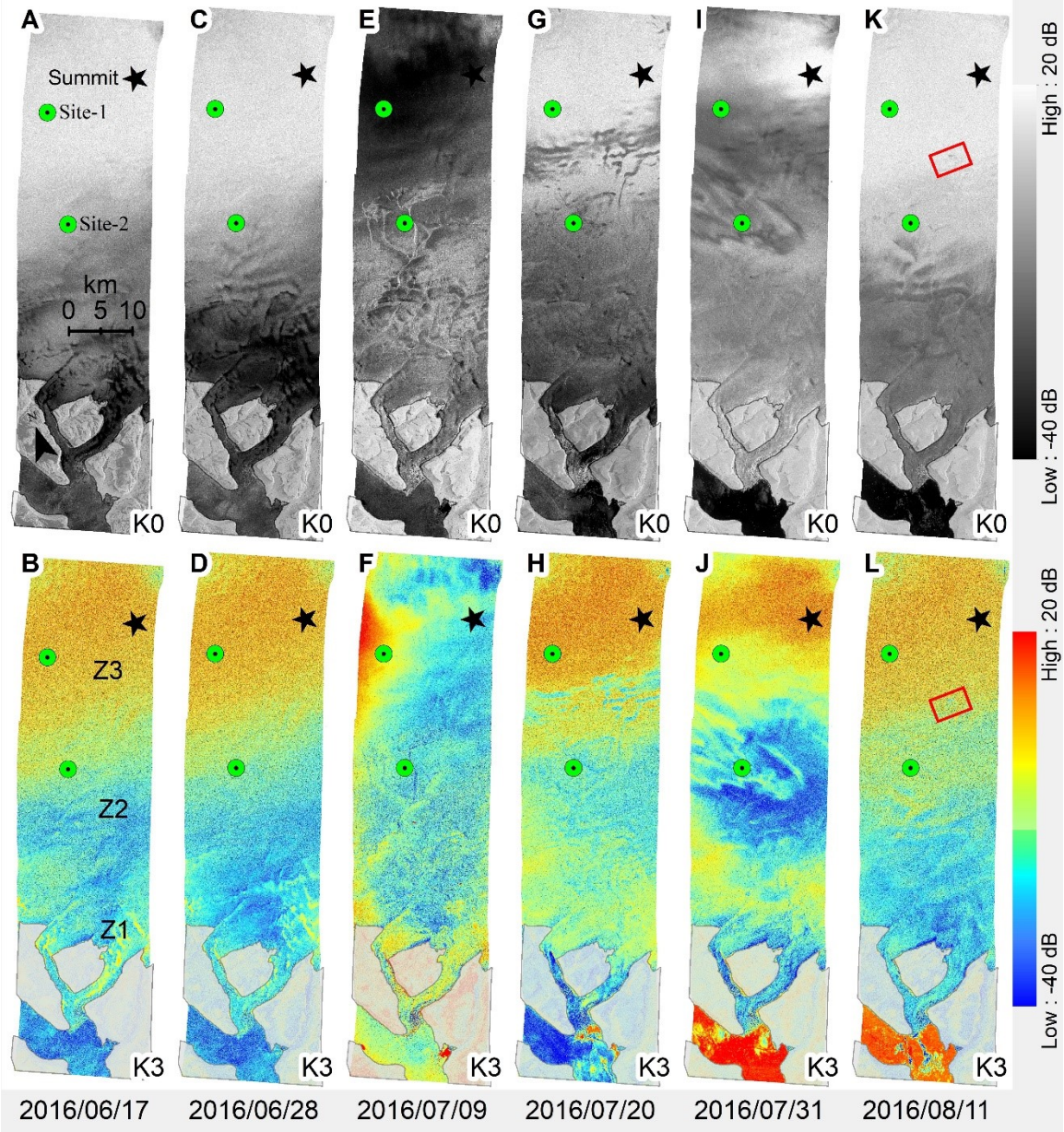

Figure 1 - TerraSAR-X images from June 17th of 2016 to 11st of August 2016 with a temporal resolution of 11 days. The red rectangle is the extent frame for the anomaly found on the image.

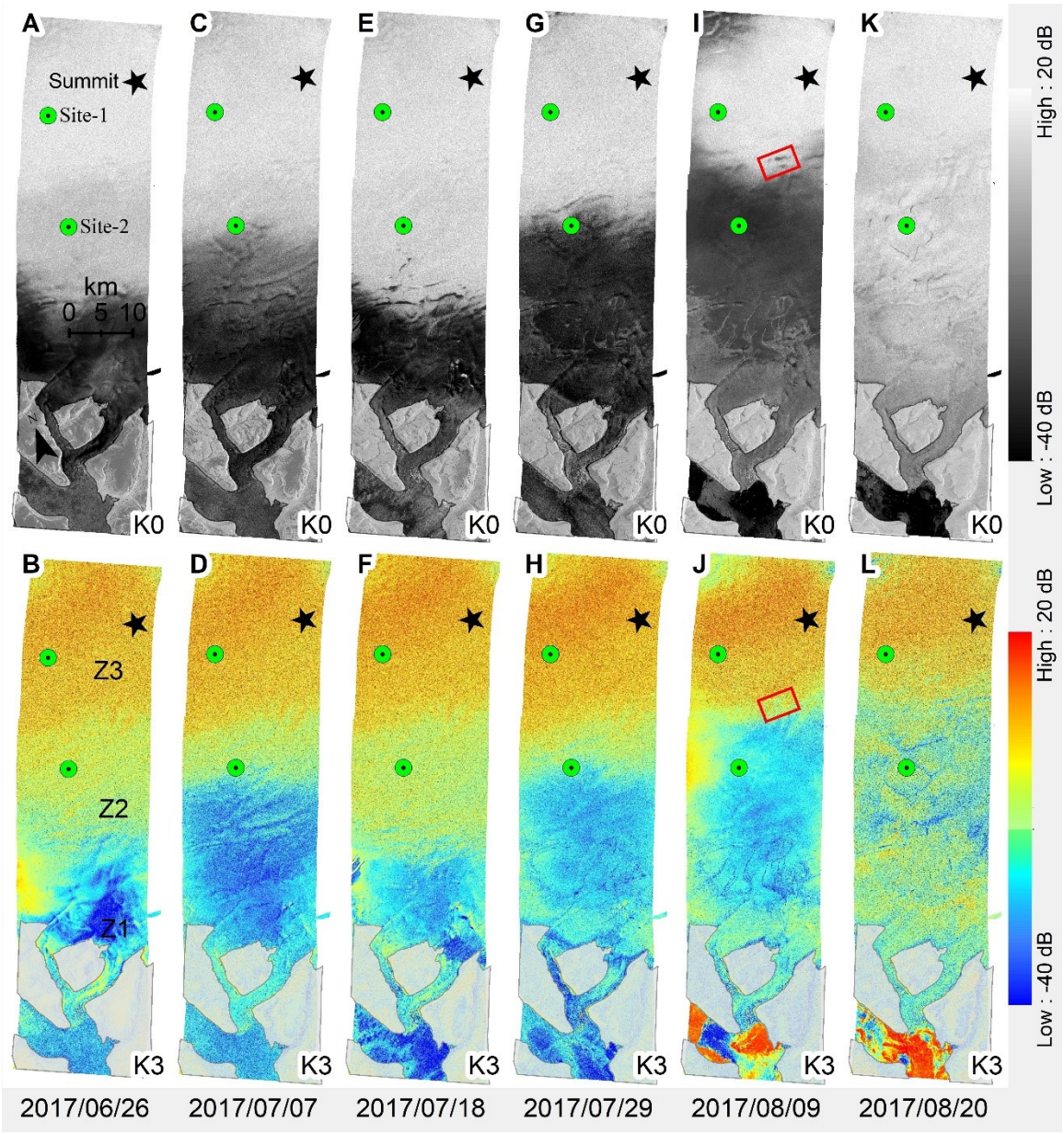

Figure 2 - TerraSAR-X images from June 26th of 2017 to 20th of August 2017 with a temporal resolution of 11 days. The red rectangle is the extent frame for the anomaly found on the image

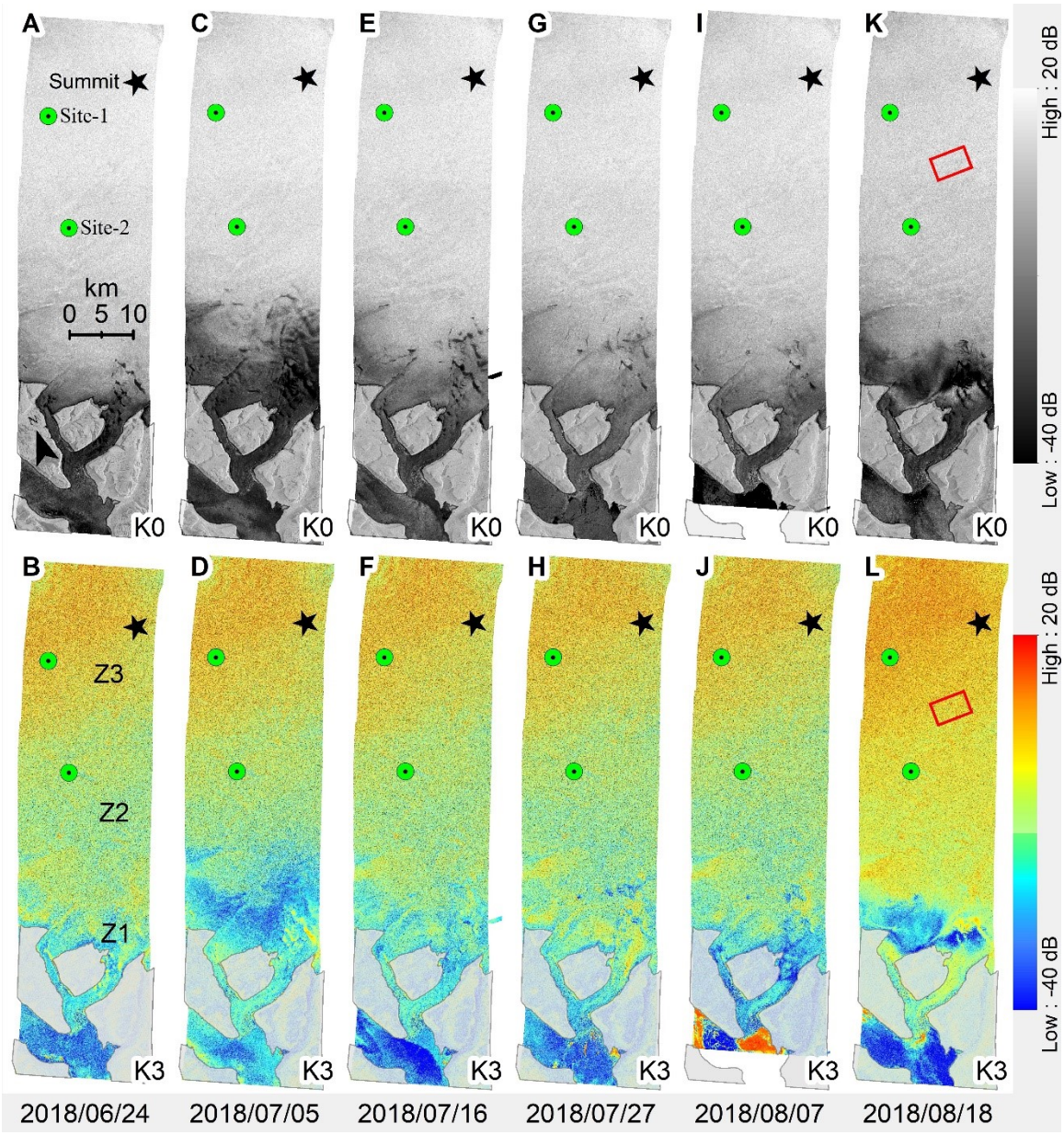

Figure 3 - TerraSAR-X images from June 24th of 2018 to 18th of August 2018 with a temporal resolution of 11 days. The red rectangle is the extent frame for the anomaly found on the image.

Appendix B - Chapter 3

Table 1 - List of images, dates, features mapped (Supraglacial channels: SC and Lakes: L), aggregate length of channels (km) and lakes (km^2) mapped. Bold indicate the image used for the mapping of glacier zones.

	Date	Image ID	Feature (SC/L)	Aggregate channel length	Aggregate lake area
2000	10-Jul	LE07_L1TP_035007_20000710	SC/L	65.8	0.8
	15-Jul	LE07_L1TP_038007_20000715	SC/L	53.2	0.0
	24-Jul	LE07_L1TP_037007_20000724	SC	7.6	
	29-Jul	LE07_L1TP_040006_20000729	SC/L	0.4	0.1
	2-Aug	**LE07_L1TP_036007_20000802**	SC	2.3	
	11-Aug	LE07_L1TP_035007_20000811	SC	41.8	
	25-Aug	LE07_L1TP_037007_20000825	SC	7.7	
		Sub-total		**178.8**	**0.9**
2001	2-Jul	LE07_L1TP_038007_20010702	SC/L	8.2	0.1
	20-Jul	**LE07_L1TP_036007_20010720**	SC/L	50.9	1.1
	29-Jul	LE07_L1TP_035007_20010729	SC	19.1	
	10-Aug	LE07_L1TP_039006_20010810	SC	122.0	
	12-Aug	LE07_L1TP_037007_20010812	SC	25.7	
	19-Aug	LE07_L1TP_038007_20010819	SC	1.1	
	26-Aug	LE07_L1TP_039006_20010826	SC	6.3	
		Sub-total		**233.4**	**1.2**
2002	19-Jul	LE07_L1TP_040006_20020719	SC	61.1	
	21-Jul	LE07_L1TP_038007_20020721	SC/L	127.9	0.0
	23-Jul	LE07_L1TP_036007_20020723	SC/L	10.2	0.6
		Sub-total		**199.1**	**0.6**
2005	4-Jul	LE07_L1TP_039006_20050704	SC/L	2.7	0.0
	29-Jul	**LE07_L1TP_038007_20050729**	SC/L	131.8	0.7

	31-Jul	LE07_L1TP_036007_20050731	SC	10.2	
	7-Aug	LE07_L1TP_037007_20050807	SC/L	1.5	0.3
	9-Aug	LE07_L1TP_035007_20050809	SC	1.0	
	14-Aug	LE07_L1TP_038007_20050814	SC	8.6	
		Sub-total		**155.7**	**1.0**
2006	24-Aug	LE07_L1TP_039006_20060824	SC	18.3	
	26-Aug	**LE07_L1TP_037007_20060826**	SC/L	147.9	0.5
		Sub-total		**166.2**	**0.5**
2007	3-Jul	LE07_L1TP_038007_20070703	SC/L	9.1	0.0
	5-Jul	LE07_L1TP_036007_20070705	SC	5.0	
	10-Jul	LE07_L1TP_039006_20070710	SC/L	22.0	0.4
	12-Jul	LE07_L1TP_037007_20070712	SC/L	94.0	0.7
	20-Aug	**LE07_L1TP_038007_20070820**	SC	65.3	
	29-Aug	LE07_L1TP_037007_20070829	SC	1.7	
		Sub-total		**197.1**	**1.2**
2008	5-Jul	LE07_L1TP_038007_20080705	SC/L	87.6	0.5
	7-Jul	LE07_L1TP_036007_20080707	SC/L	6.6	0.4
	12-Jul	**LE07_L1TP_039006_20080712**	SC	46.4	
	8-Aug	LE07_L1TP_036007_20080808	SC	22.2	
	15-Aug	LE07_L1TP_037007_20080815	SC	18.7	
	24-Aug	LE07_L1TP_036007_20080824	SC	11.5	
		Sub-total		**193.1**	**0.9**
2009	**24-Jul**	**LE07_L1TP_038007_20090724**	SC/L	108.4	0.4
	2-Aug	LE07_L1TP_037007_20090802	SC/L	23.6	0.2
	25-Aug	LE07_L1TP_038007_20090825	SC	70.2	
		Sub-total		**202.3**	**0.6**
2010	2-Jul	LE07_L1TP_039006_20100702	SC/L	22.1	0.0

	4-Jul	LE07_L1TP_037007_20100704	SC/L	58.5	0.9
	9-Jul	LE07_L1TP_040006_20100709	SC/L	3.6	0.2
	18-Jul	LE07_L1TP_039006_20100718	SC/L	125.5	0.1
	25-Jul	LE07_L1TP_040006_20100725	SC	18.8	
	27-Jul	LE07_L1TP_038007_20100727	SC	6.2	
	30-Aug	**LE07_L1TP_036007_20100830**	SC	2.6	
		Sub-total		**237.2**	**1.2**
2011	**5-Jul**	**LE07_L1TP_039006_20110705**	SC/L	57.3	0.5
	9-Jul	LE07_L1TP_035007_20110709	SC/L	156.9	0.4
	15-Aug	LE07_L1TP_038007_20110815	SC	81.3	
		Sub-total		**295.5**	**0.9**
2012	2-Jul	LE07_L1TP_036007_20120702	SC/L	64.6	1.1
	9-Jul	LE07_L1TP_037007_20120709	SC	135.5	
	14-Jul	LE07_L1TP_040006_20120714	SC	31.2	
	30-Jul	LE07_L1TP_040006_20120730	SC	8.0	
	3-Aug	LE07_L1TP_036007_20120803	SC	32.7	
		Sub-total		**271.9**	**1.1**
2013	18-Jul	LC08_L1TP_039006_20130718	SC/L	13.3	0.1
	20-Jul	LC08_L1TP_037007_20130720	SC	2.6	
	21-Jul	LE07_L1TP_036007_20130721	SC	1.6	
	22-Jul	LC08_L1TP_035007_20130722	SC	9.5	
	30-Jul	LE07_L1TP_035007_20130730	SC	4.7	
	4-Aug	LE07_L1TP_038007_20130804	SC/L	1.2	0.6
	5-Aug	LC08_L1TP_037007_20130805	SC	14.1	
	10-Aug	LC08_L1TP_040006_20130810	SC/L	87.7	0.1
	20-Aug	LE07_L1TP_038007_20130820	SC	27.9	
		Sub-total		**162.6**	**0.8**
2014	4-Jul	LE07_L1TP_040006_20140704	L		0.1
	5-Jul	LC08_L1TP_039006_20140705	SC	66.0	

	6-Jul	LE07_L1TP_038007_20140706	SC/L	30.9	0.1
	15-Aug	LC08_L1GT_095238_20140815	SC	143.0	
		Sub-total		**239.8**	**0.2**
2015	3-Jul	LC08_L1TP_036007_20150703	SC	19.4	
	10-Jul	LC08_L1TP_037007_20150710	SC/L	48.6	0.7
	12-Jul	LC08_L1TP_035007_20150712	SC	24.8	
	15-Jul	LC08_L1TP_040006_20150715	SC/L	23.3	0.0
	19-Jul	LC08_L1TP_036007_20150719	SC/L	48.2	0.4
	24-Jul	LC08_L1TP_039006_20150724	SC/L	39.6	0.3
	26-Jul	**LC08_L1TP_037007_20150726**	SC/L	27.7	0.0
	2-Aug	LC08_L1TP_038007_20150802	L		0.0
	9-Aug	LC08_L1TP_039006_20150809	SC	48.8	
		Sub-total		**280.4**	**1.4**
2016	3-Jul	LC08_L1TP_038007_20160703	SC/L	18.2	0.0
	5-Jul	LC08_L1TP_036007_20160705	SC/L	10.1	0.0
	10-Jul	LC08_L1TP_039007_20160710	SC/L	62.5	0.4
	12-Jul	LC08_L1TP_037007_20160712	SC/L	124.8	0.2
	28-Jul	LC08_L1TP_037007_20160728	SC	44.4	
	6-Aug	**LC08_L1TP_036007_20160806**	SC	30.7	
	27-Aug	LC08_L1TP_039006_20160827	SC	12.6	
		Sub-total		**303.3**	**0.7**
2017	6-Jul	LC08_L1TP_038007_20170706	SC	3.5	
	8-Jul	LC08_L1TP_036007_20170708	SC/L	4.5	0.1
	15-Jul	LC08_L1TP_037007_20170715	SC/L	2.9	0.1
	14-Aug	**LC08_L1TP_039006_20170814**	SC/L	133.6	0.6
	16-Aug	LC08_L1TP_037007_20170816	SC/L	109.3	0.3
	18-Aug	LC08_L1TP_035007_20170818	SC	18.2	
	21-Aug	LC08_L1TP_040006_20170821	SC	8.6	
		Sub-total		**280.5**	**1.1**

Total	**3597.1**	**14.2**

Table 2 - Co-registration information (displacement in x and y – in meters) of image pairs and instrument used to generate the DEM over the study area.

Object ID	Acquisition date Image 1	Sensor Image 1	Acquisition date Image 2	Sensor Image 2	dx (m)	dy (m)	Num GCPs
153953	5/9/2011	WV02	5/15/2011	WV02	-1.9	-0.93	29
45179	5/16/2011	WV01	5/16/2011	WV02	-5.54	1.48	1,055
27606	3/30/2012	WV01	4/3/2012	WV01	-1.94	1.1	106
27100	4/3/2012	WV01	4/3/2012	WV01	0.62	0.61	312
45603	4/4/2012	WV01	4/4/2012	WV02	-0.67	-1.21	461
154982	4/4/2012	WV02	4/4/2012	WV02	1.03	-1.74	81
36461	4/23/2012	WV01	4/23/2012	WV01	-0.42	1.33	791
36470	4/23/2012	WV01	4/23/2012	WV01	-7.36	0.97	11
145836	5/14/2012	WV02	5/14/2012	WV02	1.24	0.46	198
145837	5/14/2012	WV02	5/14/2012	WV02	-1.13	0.59	27
145838	5/14/2012	WV02	5/14/2012	WV02	-0.92	-2.88	7
38512	5/17/2012	WV01	5/17/2012	WV01	-0.87	0.55	248
145773	5/17/2012	WV02	5/17/2012	WV02	0.85	-2.77	24
145778	5/17/2012	WV02	5/17/2012	WV02	0.27	1.32	45
155688	6/1/2012	WV02	5/24/2012	WV02	-25.21	-12.72	63
145541	7/10/2012	WV02	7/10/2012	WV02	0.42	0.07	316
145519	7/13/2012	WV02	7/13/2012	WV02	-0.56	-1.66	158
38179	7/17/2012	WV01	7/17/2012	WV01	0.14	-0.06	28
37416	8/2/2012	WV01	8/2/2012	WV01	-8.63	4.54	83

37228	8/19/2012	WV01	8/19/2012	WV01	0.34	-5.63	684
38993	4/29/2013	WV01	4/29/2013	WV01	-1.62	-4.03	9
149739	5/9/2013	WV02	5/9/2013	WV02	1.07	-0.39	33
39305	6/23/2013	WV01	6/23/2013	WV01	-0.32	-0.03	134
148608	7/3/2013	WV02	7/3/2013	WV02	1.1	0.64	16
148662	7/8/2013	WV02	7/8/2013	WV02	-22.41	26.86	4
148710	7/20/2013	WV02	7/20/2013	WV02	2.58	1.65	148
148714	7/20/2013	WV02	7/20/2013	WV02	2.1	2.39	180
40724	7/21/2013	WV01	7/21/2013	WV01	-2.37	0.06	135
40002	8/4/2013	WV01	8/4/2013	WV01	-2.02	-1.39	573
39793	8/8/2013	WV01	8/8/2013	WV01	0.87	-2.36	766
42035	4/4/2014	WV01	4/4/2014	WV01	0.36	-0.41	895
41705	4/7/2014	WV01	4/7/2014	WV01	-5.24	-4.04	622
41712	4/7/2014	WV01	4/7/2014	WV01	-1.26	-1.68	7
150102	4/17/2014	WV02	4/17/2014	WV02	1.63	-0.35	45
41557	4/19/2014	WV01	4/19/2014	WV01	-0.77	0.07	728
44236	5/30/2014	WV01	5/30/2014	WV01	-0.47	1.96	402
152398	5/30/2014	WV02	5/30/2014	WV02	-12.21	-26.37	12
152402	5/30/2014	WV02	5/30/2014	WV02	-0.1	1.51	54
43125	8/22/2014	WV01	8/22/2014	WV01	-3.12	1.93	374
26232	2/27/2015	WV01	2/27/2015	WV01	-10.32	-3.6	9
32636	2/27/2015	WV01	2/27/2015	WV01	-8.79	-10.04	9
32638	2/27/2015	WV01	2/27/2015	WV01	-7.01	0.16	87
234654	2/27/2015	WV03	2/27/2015	WV03	2.87	1.11	636
234660	2/27/2015	WV03	2/27/2015	WV03	1.04	-0.11	721

33137	2/28/2015	WV01	2/28/2015	WV01	-0.26	0.13	814
137939	2/28/2015	WV02	2/28/2015	WV02	2.98	-1.8	897
137855	3/2/2015	WV02	3/2/2015	WV02	0.24	0.32	460
157270	3/2/2015	WV02	3/3/2015	WV01	5.45	-0.51	443
32861	3/3/2015	WV01	3/3/2015	WV01	-1.95	-0.13	168
137613	3/3/2015	WV02	3/3/2015	WV02	0	-1.4	968
33035	3/18/2015	WV01	3/18/2015	WV01	-12.39	3.11	7
44856	3/24/2015	WV01	3/25/2015	WV02	-1.03	-0.34	34
137979	3/25/2015	WV02	3/25/2015	WV02	-0.17	0.48	733
141943	3/23/2016	WV02	3/23/2016	WV02	-2	-1.73	28
141927	3/25/2016	WV02	3/25/2016	WV02	1.2	0.33	860
141930	3/25/2016	WV02	3/25/2016	WV02	0.61	-0.12	539
141935	3/25/2016	WV02	3/25/2016	WV02	-0.96	1.87	898
154412	3/25/2016	WV02	3/25/2016	WV02	2.68	-2.26	94
139932	4/1/2016	WV02	4/1/2016	WV02	0.15	0.14	769
36036	5/5/2016	WV01	5/5/2016	WV01	-4.52	0.69	408
143199	5/5/2016	WV02	5/5/2016	WV02	0.15	-1.58	306
238320	5/8/2016	WV03	5/8/2016	WV03	-3.41	-2.01	148
143525	5/9/2016	WV02	5/9/2016	WV02	0.51	-1.46	640
34503	6/8/2016	WV01	6/8/2016	WV01	1.05	2.95	28
31211	3/14/2017	WV01	3/14/2017	WV01	0.15	-0.47	96
31054	3/17/2017	WV01	3/17/2017	WV01	-3.48	2.43	896
233171	3/18/2017	WV03	3/18/2017	WV03	1.56	0.18	30
30915	3/19/2017	WV01	3/19/2017	WV01	-7.06	13.52	5
134891	3/26/2017	WV02	3/26/2017	WV02	0.75	2.64	691

135057	3/29/2017	WV02	3/29/2017	WV02	0.66	0.73	1,207
233348	3/29/2017	WV03	3/29/2017	WV03	-1.13	-4.73	16
233355	3/29/2017	WV03	3/29/2017	WV03	0.4	-1.06	319
30102	4/4/2017	WV01	4/4/2017	WV01	-4.25	-5.18	26
29660	4/19/2017	WV01	4/19/2017	WV01	-1.01	-0.23	1,092
31590	5/5/2017	WV01	5/5/2017	WV01	-2.25	2.09	30
				mean	-1.9	-0.4	

Table 3 - Spatially-averaged minimum, mean, and maximum elevations (m a.s.l.) and standard deviation (m) of the Snow line (SL) and Wet-snow line (WSL), the area (km^2) of the glacier zones for the period 2000–16, when sufficient imagery was available.

	2000	**2001**	**2005**	**2006**	**2007**	**2008**	**2009**	**2010**	**2011**	**2012**	**2015**	**2016**
SL mean elev.	906	911	878	870	908	922	921	941	919	961	969	978
SL minimum elev.	771	782	717	728	809	788	769	844	772	863	865	863
SL maximum elev.	1021	1289	997	978	1012	1061	1039	1060	1022	1053	1058	1131
SL Standard Deviation	52	48	45	48	41	57	50	48	44	44	46	56
WSL mean elev.	1400	1317	1235	1418	1304	1265	1323	1358	1221	1553	1492	1495
WSL minimum elev.	1290	1083	942	1001	1033	1022	1028	1099	957	1468	1416	1447
WSL maximum elev.	1583	1437	1497	1797	1613	1390	1554	1518	1380	1614	1577	1627
WSL Standard Deviation	87	70	145	228	161	86	114	121	110	34	35	30
BI & SI	148	156	103	92	151	174	173	208	169	245	260	277
Wet-Snow Zone	1036	846	728	1132	822	716	843	884	635	1217	1109	1097
Percolation Zone	573	755	926	533	784	866	742	666	954	295	388	383

Table 4 - Summary statistics of supraglacial lakes observed over the study period (2000–17).

	2000	**2001**	**2002**	**2005**	**2006**	**2007**	**2008**	**2009**	**2010**	**2011**	**2012**	**2013**	**2014**	**2015**	**2016**	**2017**
Number of lakes observed	8	7	6	5	5	8	6	5	8	6	5	6	4	11	10	7
Area of smallest lake (km^2)	0.02	0.02	0.01	0.03	0.02	0.03	0.02	0.04	0.04	0.06	0.04	0.03	0.03	0.01	0.02	0.09
Area of largest lake (km^2)	0.26	0.35	0.19	0.28	0.20	0.33	0.26	0.19	0.36	0.39	0.38	0.28	0.09	0.29	0.24	0.34
Average lake area (km^2)	0.11	0.17	0.10	0.20	0.10	0.15	0.15	0.12	0.15	0.15	0.22	0.13	0.05	0.12	0.07	0.16
Total area of all lakes (km^2)	0.90	1.19	0.62	1.01	0.50	1.17	0.92	0.60	1.20	0.87	1.08	0.77	0.20	1.36	0.70	1.12
Highest elevation (m a.s.l.) at which a lake was observed	1198	1198	1198	1197	1198	1198	1197	1254	1198	1197	1198	1141	1141	1610	1610	1198

Table 5 - Area of all lakes mapped during the study period (2000–17) (see Figure 3.5). Elevation of each lake is shown in brackets.

	2000	**2001**	**2002**	**2005**	**2006**	**2007**	**2008**	**2009**	**2010**	**2011**	**2012**	**2013**	**2014**	**2015**	**2016**	**2017**
Lake 1 (918 m a.s.l.)	0.10	0.24	0.07	0.23	0.05	0.29	0.19	0.16	0.24	0.06	0.07	0.27		0.21	0.07	0.10
Lake 2 (943 m a.s.l.)	0.20	0.25	0.19	0.24	0.10	0.33	0.22	0.19	0.36	0.39	0.38	0.28	0.04	0.29	0.12	0.15
Lake 3 (1197 m a.s.l.)	0.22	0.35	0.12	0.28	0.20	0.21	0.17	0.16	0.12	0.11	0.23			0.25	0.24	0.34
Lake 4 (1142 m a.s.l.)	0.26	0.21	0.19	0.23	0.12	0.20	0.26		0.16	0.18	0.36	0.12	0.09	0.27		0.16
Lake 5 (842 m a.s.l.)	0.02	0.02		0.03		0.04	0.05		0.11			0.03	0.03	0.06	0.08	
Lake 6 (1122 m a.s.l.)	0.05					0.03	0.02		0.10	0.06				0.10		0.19
Lake 7 (1032 m a.s.l.)	0.04					0.04			0.08			0.04		0.07	0.03	0.09
Lake 8 (844 m a.s.l.)	0.02	0.05	0.01			0.03						0.03	0.04	0.03	0.05	0.09
Lake 9 (1092 m a.s.l.)		0.07	0.04		0.02			0.04	0.04		0.04					
Lake 10 (1257 m a.s.l.)								0.05								
Lake 11 (1194 m a.s.l.)										0.08						
Lake 12 (984 m a.s.l.)														0.02		
Lake 13 (1614 m a.s.l.)														0.05	0.02	
Lake 14 (1590 m a.s.l.)														0.01	0.02	
Lake 15 (1280 m a.s.l.)															0.02	
Lake 16 (1161 m a.s.l.)															0.05	

Appendix C - Chapter 4

	Start Length (cm)	End Length (cm)	Total Length (cm)	Material
Firn Core C1	0	115	115	Firn
	115	145	30	Ice
	145	154	9	Firn
	154	164	10	Ice
	164	178	14	Firn
	178	179	1	Ice
	179	205	26	Firn
	205	270	65	Ice
	270	286	16	Firn
	286	300	14	Ice
	300	305	5	Firn
	305	307	2	Ice
	307	328	21	Firn
	328	575	247	Ice
	575	580	5	Firn
Firn Core C2	0	350	350	Ice
	350	356	6	Firn
	356	386	30	Ice
	386	440	54	Firn
	440	446	6	Ice
	446	480	34	Firn
	480	485	5	Ice
	485	486	1	Firn
	486	487	1	Ice
	487	510	23	Firn
	510	607	97	Ice

	Start Length (cm)	End Length (cm)	Total Length (cm)	Material
Firn Core CC	0	56	56	Firn
	56	69	13	Ice
	69	80	11	Firn
	80	166	86	Ice
	166	187	21	Firn
	187	200	13	Ice
	200	238	38	Firn
	238	342	104	Ice
	342	360	18	Firn
	360	363	3	Ice
	363	434	71	Firn
	434	435	1	Ice
	435	442	7	Firn
	442	451	9	Ice
	451	455	4	Firn
	455	462	7	Ice
	462	474	12	Firn
	474	482	8	Ice
	482	490	8	Firn
	490	507	17	Ice
	507	574	67	Firn

Figure 1 - Detailed information and description of firn cores drilled along the grid lines

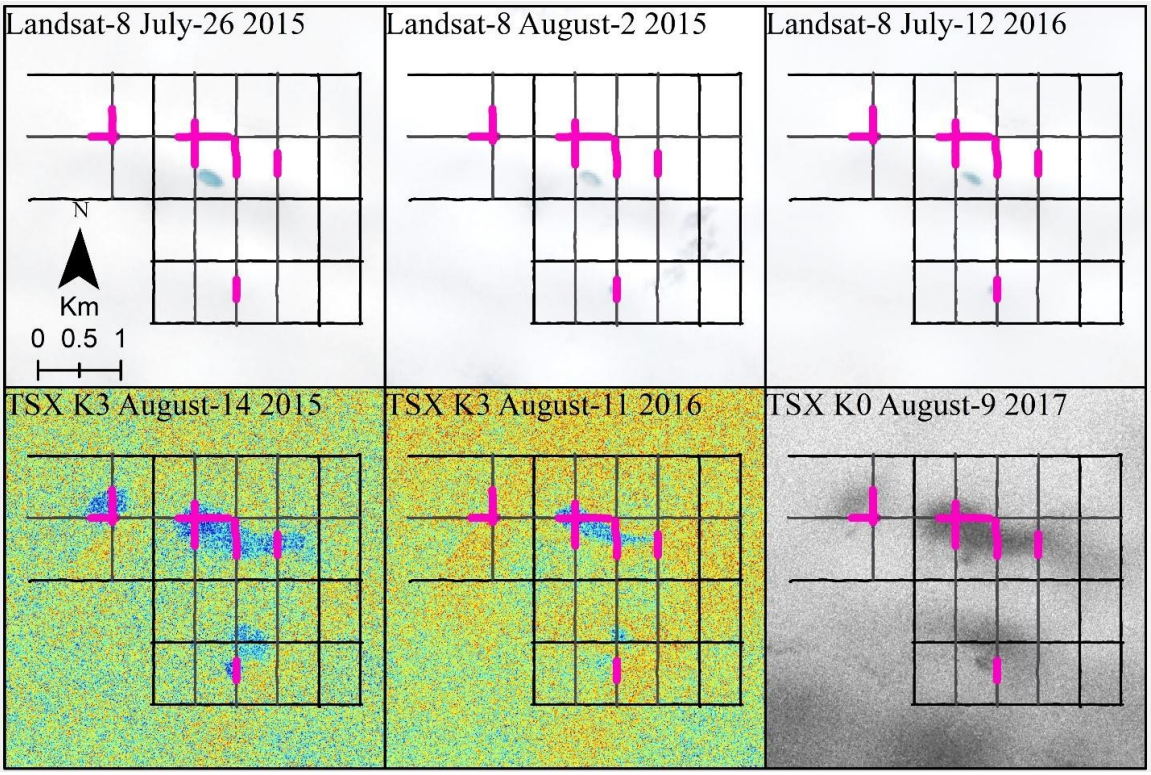

Figure 2 - Images from Landsat-8 and the Kennaugh Elements of the area in which the lakes anomaly was found. The pink lines represent the sections of each profile on which the ice build-up anomaly was at its maximum extent on 14-August 2015